MODELING AND EXPERIMENTS TO DEVELOP THERMO-ELECTROCHEMICAL CELLS

A Dissertation

Presented to

The Academic Faculty

By

Pablo Felix Salazar Zarzosa

In Partial Fulfillment

of the Requirements for the Degree

Doctor of Philosophy in the

George W. Woodruff School of Mechanical Engineering

Georgia Institute of Technology

December 2014

MODELING AND EXPERIMENTS TO DEVELOP THERMO-ELECTROCHEMICAL CELLS

Approved by:

Dr. Baratunde A. Cola, Advisor
School of Mechanical Engineering
Georgia Institute of Technology

Dr. Todd A. Sulchek
School of Mechanical Engineering
Georgia Institute of Technology

Dr. Satish Kumar, Co-advisor
School of Mechanical Engineering
Georgia Institute of Technology

Dr. Thomas F. Fuller
School of Chemical Engineering
Georgia Institute of Technology

Dr. Peter J. Hesketh
School of Mechanical Engineering
Georgia Institute of Technology

Dr. Sankar Nair
School of Chemical Engineering
Georgia Institute of Technology

Date Approved: August 19, 2014

To my family

ACKNOWLEDGEMENTS

I am grateful to God for His guidance through these years. I am also grateful to my mother for her amazing support.

Then, I would like to express my appreciation to my advisors, Dr. Baratunde Cola and Dr. Satish Kumar, for their assistance throughout my entire Ph.D research process. I would also like to thank Dr. Sulchek, Dr. Fuller, Dr. Hesketh, and Dr. Nair for serving on my committee. Their comments added a lot to my research.

I would like to acknowledge the members of NEST lab, colleagues and friends for their support and help, and useful conversations throughout my stay at Georgia Tech.

Contents

List of Tables

List of Figures

List of symbols

Symbol	Property [Units]
A	Electrode surface area [m^2]
β_{T1}	Temperature density change coefficient 1[kg m^{-3}]
β_{T2}	Temperature density change coefficient 2 [kg m^{-3} K^{-1}]
β_{T3}	Temperature density change coefficient 3 [kg m^{-3} K^{-2}]
C_p	Electrolyte heat capacity [J kg^{-1} K^{-1}]
C_i	Ion concentration [mol m^{-3}]
C_i^*	Initial ion concentration [mol m^{-3}]
C_O	Oxidized concentration [mol m^{-3}]
C_R	Reduced concentration [mol m^{-3}]
C_{Cl}	Counter ion concentration [mol m^{-3}]
D_i	Ion diffusion coefficient [m^2 s^{-1}]
D_O	Oxidized diffusion coefficient [m^2 s^{-1}]
D_R	Reduced diffusion coefficient [m^2 s^{-1}]
D_{Cl}	Counter ion diffusion coefficient [m^2 s^{-1}]
ρ	Electrolyte density [kg m^{-3}]
ρ_o	Electrolyte density reference at 300 K [kg m^{-3}]
ε	dielectric constant [A^2 s^4 kg^{-1} m^{-3}]
E	Electrode potential [V]
E^o	Standard electrode potential [V]
E_a	Anode potential [V]

E_a^{eq}	Anode equilibrium potential [V]
E_c	Cathode potential [V]
E_c^{eq}	Cathode equilibrium potential [V]
Ex_a	Rate constant activation energy [J $mol^{-1}K^{-1}$]
F	Faraday constant [C mol^{-1}]
h_e	Effective heat transfer coefficient [W m^{-2} K^{-1}]
I_o	Optimum cell current [A]
j	Electronic current density [A m^{-2}]
j_a	Electronic current density at the anode [A m^{-2}]
j_c	Electronic current density at the cathode [A m^{-2}]
J_{sc}	Short-circuit current density [A m^{-2}]
j_{wc}	Electronic current density without convection [W m^{-2}]
k	Electrochemical rate constant [m s^{-1}]
k^o	Standard rate constant [m s^{-1}]
κ_s	Electrolyte thermal conductivity [W m^{-1} K^{-1}]
κ_e	Electrode thermal conductivity [W m^{-1} K^{-1}]
$\vec{N}_i$	Ion flux density [mol m^{-2} s^{-1}]
$\vec{N}_O$	Oxidized flux density [mol m^{-2} s^{-1}]
$\vec{N}_R$	Reduced flux density [mol m^{-2} s^{-1}]
$\vec{N}_{Cl}$	Counter ion flux density [mol m^{-2} s^{-1}]
n	Number of electrons transferred [-]
η	Conversion efficiency [%]

η_i	Conversion efficiency of intermediate cell [%]
η_r	Relative efficiency [%]
ξ_a	Anode overpotential [V]
ξ_c	Cathode overpotential [V]
P_e	Electric power density [W m^{-2}]
P_i	Electric power of intermediate cell [W]
P_m	Maximum electric power density [W m^{-2}]
q	Heat flux density [W m^{-2}]
q_{wc}	Heat flux density without convection [W m^{-2}]
Q_{CI}	Counter ion heat of transport [J mol^{-1}]
Q_i	Ion heat of transport [J mol^{-1}]
Q_O	Oxidized heat of transport [J mol^{-1}]
Q_R	Reduced heat of transport [J mol^{-1}]
R	Gas constant [J $mol^{-1}K^{-1}$]
$\mathcal{R}_T$	Thermocell volume [m^3]
S	Heat generation sources [W m^{-3}]
T	Temperature [K]
T_a	Anode temperature [K]
T_c	Cathode temperature [K]
T_H	Temperature at the hot electrode [K]
T_o	Standard temperature [K]
U_C	Cold flow temperature [K]

U_H	Hot flow temperature [K]
u_i	Ion mobility [$m^2\ s^{-1}\ V^{-1}$]
$\vec{u}$	Bulk vector velocity [$m\ s^{-1}$]
υ	kinematic viscosity [$m^2\ s^{-1}$]
V_o	Optimum cell voltage [V]
V_{oc}	Open circuit cell voltage [V]
V_T	Cell voltage [V]
Z_{Cl}	Counter ion charge number [-]
Z_i	Ion charge number [-]
Z_O	Oxidized charge number [-]
Z_R	Reduced charge number [-]
ϕ	Electrostatic potential [V]
θ	Charge transfer coefficient [-]
$\Delta\phi^s$	Solution ohmic drop [V]
ΔS^o_{rx}	Standard redox reaction entropy [$J\ mol^{-1}K^{-1}$]
ΔH^o_{rx}	Standard redox reaction enthalpy [$J\ mol^{-1}$]
ΔG^o_{rx}	Standard redox reaction free energy [$J\ mol^{-1}$]
$\int_a$	Integral at the anode surface
$\int_c$	Integral at the cathode surface
$\int_T$	Integral in the thermocell

SUMMARY

Low-temperature waste heat recovery is an important component of generating a more efficient, cost-effective and environmentally-friendly energy source. To meet this goal, thermo-electrochemical cells (TECs) are electrochemical devices that produce a steady electric current under an applied temperature difference between their electrodes. TECs have zero gas emissions, can be flexible and can be relatively inexpensive. However, current TECs have low conversion efficiencies. On this project, I developed a comprehensive multiscale model that couples the governing equations in TECs (mass and heat transfer, electro-kinetics and fluid dynamics). The model was used to understand the fundamental principles and limitations in TECs, and to find the optimum cell thickness, aspect ratio and number of cells in a series stack. Doped multiwall carbon nanotubes (MWCNTs) were then explored as alternative electrodes for TECs. The results show that nitrogen and boron doping of MWCNT buckypaper, through plasma-enhanced chemical vapor deposition, increases the electrochemically active surface area of the electrodes. However, electrostatic interactions with potassium ions (in potassium ferri/ferrocyanide electrolytes) reduce the charge transfer kinetics of doped electrodes, resulting in lower power of TECs.

One of the main objectives of this dissertation is to study multiwall carbon nanotube/ionic liquid (MWCNT/IL) mixtures as alternative electrolytes for TECs. Previous authors showed that the addition of carbon nanotubes (CNTs) to a solvent-free IL electrolyte improves the efficiency of dye solar cells by 300%. My research plan involved a spectroscopy analysis of imidazolium-based ionic liquids (IILs) mixed with MWCNTs using impedance spectroscopy and nuclear magnetic resonance. The results

show a percolation threshold below 1 wt% of MWCNTs due to their high dispersibility in IILs. The addition of MWCNTs increases the diffusion coefficient of the anions up to 35%, which is likely due to weak van der Waals interactions between the MWCNT walls and the cations. The MWCNTs also appear to polarize their interface with IILs, yielding a 3- to 5-fold increase in electrical conductivity of the mixture at MWCNT concentrations that are under the threshold for percolation. The results show that the combination of these effects (interfacial polarization and ion pair dissociation) reduces mass transfer resistances and enhances the power of TECs at low wt% of MWCNTs. This happens in spite of reduced open circuit voltage due to percolated networks.

CHAPTER 1. INTRODUCTION

1.1 Motivation: waste heat recovery

In 2008, the US Department of Energy (DOE) reported that 50 to 66% of the energy used by industry is wasted as heat (**Fig. 1.1A**). This represents a loss of almost 2 quadrillion BTU/year [1]. DOE estimated that this energy loss is equivalent to $6 million per year. Harvesting high- and low-temperature waste heat could reduce gas emissions and improve the energy efficiency of industrial plants, vehicles and residential buildings. The technologies to recover high-temperature waste heat (above 600°C), such as combustion air and boiler feed water preheating, can be cost effective. While the limits imposed by the second law of thermodynamics (Carnot efficiency: $(T_{Hot} - T_{Cold})/T_{Hot}$) make it difficult to achieve the cost effectiveness of high-temperature waste heat recovery processes, the large amounts of low-temperature waste heat (< 230°C) (**Fig. 1.1B** [1]) justify efforts to recover it. The most efficient technology for recovering low-temperature waste heat as electricity is the organic Rankine cycle (ORC), which operates between 25°C and 150-400°C with an overall efficiency of 10-20% [2].

The ORC can be used to harvest waste heat from gas turbines, furnaces and boiler exhausts; but the process requires heat transfer from the waste source to the boiler of the ORC. An efficient ORC fluid should have a low boiling point, good chemical stability at the source temperature, environmental suitability and high latent heat of vaporization. Thus, the efficiency of an ORC is maximized to a particular working fluid, depending on the source temperature and the thermodynamic properties of the fluid. Despite these technical barriers, the ORC can be cost-effective with prices from 3.5 to 1.5 dollars per

watt, especially when compared to thermoelectric generation devices that are priced above $20/W [3]. Other technologies for waste heat recovery are solid-state thermoelectrics and thermo-electrochemical cells (TECs). Solid-state thermoelectrics are based on n-type and p-type semiconductors, e.g. Bi_2Te_3 and PbTe, which create a voltage under a thermal gradient, as a result of the Seebeck effect. Although nanostructuring and alloying can increase the efficiency of thermoelectrics by as much as 20% [3], these techniques can often increase cost. Despite their high costs, thermoelectrics are attractive because they can be compact and lightweight and thus suitable for small scale or mobile applications, e.g., vehicle or space heat recovery. Thermoelectric devices have the additional advantages of zero gas emissions, high reliability and no moving parts, which reduces the need for maintenance.

TECs are based on redox electrolytes, which are typically aqueous solutions. The electrolyte produces a voltage that depends on the reaction entropy of the redox couple and the temperature difference between the electrodes. TECs can have an extra advantage over conventional solid-state semiconductor thermoelectrics. For example, if the electrodes are made of flexible material, such as buckypaper or electrically conductive polymer, the cell can be molded to any waste heat source geometry. This versatility eliminates the need for extra equipment to transfer the waste heat, when compared to ORC or conventional semiconductor thermoelectrics. TECs can also be inexpensive, depending mainly on the cost of the buckypaper or the conductive polymer electrode used. These cells, however, are limited by their low conversion efficiency, at least one order of magnitude lower than conventional semiconductor thermoelectrics. In TECs, charges are transported by ions, instead of electrons, which are used in solid-state

thermoelectrics. The slower mobility of ions compared to electrons limits the electrical conductivity of TECs, thus their efficiency. This thesis fundamentally investigates the potential increase in efficiency of TECs that can be achieved by enhancing the ionic diffusion and conductivity of the electrolyte, and by optimizing the cell dimensions.

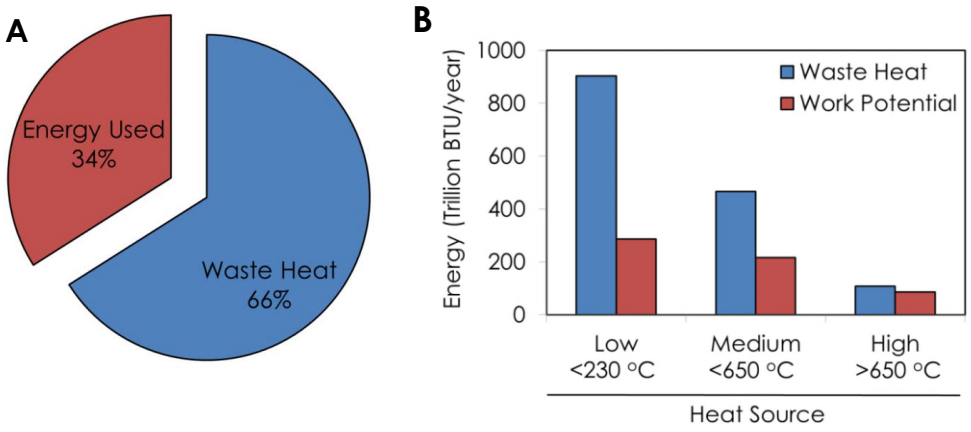

Fig. 1.1 A) Energy produced and wasted as heat. B) Breakdown of the waste heat energy by temperature of the source. Work potential is the heat energy that could be recovered based on the Carnot efficiency [1].

1.2 Review of thermo-electrochemical cells

TECs are electrochemical devices that produce a steady electric current under an applied temperature difference between the electrodes. The electrode at higher temperature (hot) is designated as the anode, and the cold electrode as the cathode. The cell, filled with a redox electrolyte in an aqueous, or non-aqueous solution or a solid state membrane, creates a voltage proportional to the redox reaction entropy of the electrolyte. When the cell is connected to a load, current flows through the load in an attempt to reach electrochemical equilibrium. The continuity of electronic current is maintained by a flux of the electrolyte within the cell. At the anode the reduced species are consumed, while

they are generated at the cathode. The concentration gradient built up drives a diffusion flux that returns the reduced species to the anode and the oxidized species to the cathode. The transport of ions is also driven by a combination of convection, migration and thermal diffusion. A steady-state current is maintained as long as the temperature difference persists. **Fig 1.2** highlights the main aspects of TECs.

Ideally, the electrolyte used in TECs should have high ionic conductivity and fast kinetics at the electrodes to maximize the current density. It should have a high redox reaction entropy and low thermal conductivity to increase the conversion efficiency. The electrolyte should be chemically and thermally stable, and it should not corrode the electrodes and packaging materials, in order to ensure a long lifetime of operation.

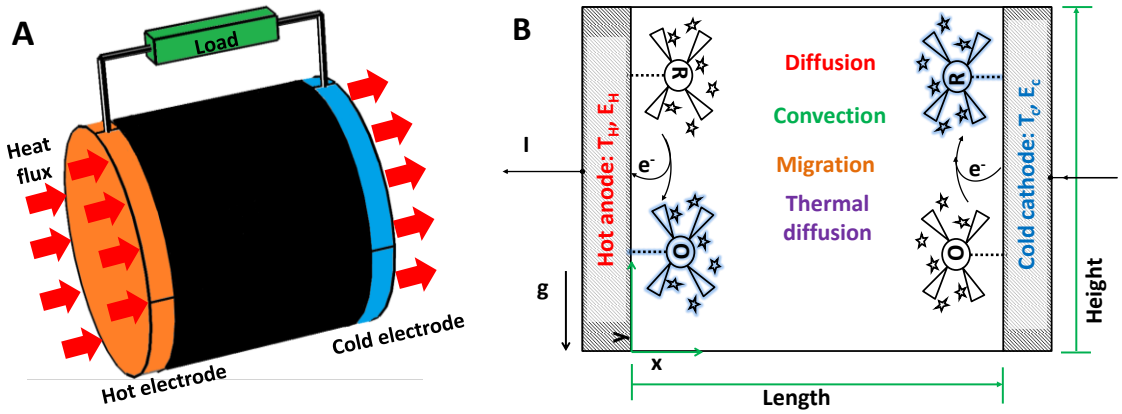

Fig. 1.2 3-D (A) and 2-D (B) schematic representation of thermocells (enclosed cell) with electrodes placed vertically. Cell voltage, V_{cell}, is a function of the redox reaction entropy, temperature difference at the electrodes and current. Electric current, I, depends on kinetic and mass transfer parameters as well as cell dimensions.

The conversion efficiency of thermocells is evaluated by

$$\eta\,[\%] = \frac{\text{Maximum electric power}}{\text{Input heat}}(100) = \frac{V_o I_o}{h_e \Delta T}(100) \qquad \text{eq. 1}$$

and the relative efficiency with respect to the Carnot efficiency, $\eta_r = \frac{\eta}{\Delta T / T_H}$. The input heat can be represented by the temperature difference (ΔT) and an effective heat transfer coefficient, h_e, which depends on the electrolyte thermal conductivity, cell thickness and, in some cases, natural or forced convection. Since the electric current depends on the cell voltage (based on the Butler-Volmer model), the maximum power is found by optimizing the current and voltage of the cell. The electric current also depends on the effective surface area of the electrode, the effective diffusivity of the ions, the electro-kinetic rate constant, cell thickness and the effect of natural or forced convection (if there is any).

Hupp *et al.* reported values of standard redox reaction entropy for aqueous and non-aqueous electrolytes [4]. In this survey, aqueous potassium ferri/ferrocyanide solutions were demonstrated to have one of the highest redox reaction entropies, e.g. -180 J/mol-K, leading to a 1.4 mV/K thermal-to-voltage conversion. Thus, conventional TECs are based on this redox couple. The electrode materials are usually materials with high catalytic activity such as platinum, in order to ensure fast reactions at the electrodes [5,6]. The electrodes are also conventionally symmetric, i.e., the same material is used for the anode and cathode, because the reaction entropy depends on the redox couple and not on the nature of the electrode material.

Regarding theoretical studies, Sokirko developed an analytical solution for the 1-D diffusion-migration transport and 2-D diffusion-convection transport in a numerical study of TECs [7]. Ikeshoji *et al*. presented a 2-D numerical simulation of power, current and heat flux density considering diffusion, migration and natural convection in a potassium ferri/ferrocyanide electrolyte [8,9]. These reports showed that natural convection has a strong effect in the conversion efficiency of TECs, because, in low

viscosity solutions, mass boundary layers are thinner than thermal boundary layers [10,8,9,7]. The effects of natural convection were also demonstrated through the effect of cell orientation on power density. For example, when horizontal electrodes (parallel to gravity) or cold above hot vertical electrodes were used, the power density was higher than in TECs with hot-above-cold vertical electrodes.

In early experimental studies, TECs with aqueous ferri/ferrocyanide solutions and platinum electrodes showed conversion efficiencies of less than 0.1% and electric powers up to 2 W/m^2 [11,12,10,13]. However, the low efficiencies and required use of platinum electrodes to achieve kinetic reversibility diminished further research efforts on TECs. But in 2001, Nugent *et al.* showed fast kinetics using potassium ferri/ferrocyanide on MWCNT electrodes [6]. Motivated by these results, Hu *et al.* [14] showed that MWCNT electrodes could be used in TECs to increase energy conversion efficiency and potentially to reduce their cost, as the cost of MWCNTs continues to decrease. The high catalytic activity of CNTs toward oxidation and reduction reactions has found application in other electrochemical devices (e.g., batteries, sensing and fuel cells) [15,14,16-19]. Another attractive characteristic of CNTs is their relative ease of functionalizing or doping to potentially alter their properties [20]. For example, nitrogen doped CNTs have been shown to have a greater electrocatalytic activity than pristine CNTs toward oxygen reduction reactions [21].

It is also possible to improve the conversion efficiency of TECs by enhancing the internal accessible surface area of the CNT electrodes and/or by using electrolytes with small molecular volume (e.g., lithium salts), while keeping the same cross-sectional area to the heat source. TECs based on lithium-intercalated electrodes and lithium salts have

been demonstrated to have values of thermal-to-voltage and energy efficiency conversion that are similar to those of potassium ferri/ferrocyanide with Pt electrodes [22].

As alternative electrolytes, ILs are promising because of their good chemical and thermal stability, low thermal conductivity, and ability to act as a solvent and source of redox couple (solvent-free electrolyte) [23]. Recent reports have demonstrated the use of ILs as solvents for TEC electrolytes, allowing waste heat recovery from higher temperature sources (150 – 200 °C) than can be obtained with aqueous electrolytes [24-27]. For example, Pringle *et al*. used a novel cobalt-based redox couple diluted in an IIL as an alternative electrolyte for TECs [26,27]. This redox couple shows a fast kinetics on platinum electrodes, as well as in less expensive electrodes (MWCNTs and poly(3,4-ethylenedioxythiophene)) [26,28]. In addition, the unsymmetrical and complex structure of ILs could potentially yield high reaction entropies [4]. Previous authors have reported unexpectedly high temperature-to-voltage conversion up to 7 mV/K in non-aqueous electrolytes [29]. However, ILs usually have a viscosity 25 times or greater than that of water [30], which decreases the ionic diffusion in these solvents, increases the ohmic resistance and makes natural convection effects weak in these systems. The loss of power due to thick diffusive boundary layers and high ohmic drops is partially compensated by the low thermal conductivity of ILs, which is approximately 5 times lower than that of aqueous electrolytes [31]. Thus, further research on ILs for TECs is aimed to reduce the mass transfer limitations.

Some authors have proposed the addition of CNTs to IL electrolytes (CNT-ILs) in order to improve the efficiency of dye solar cells (DSCs) [32-35]. For example, Lee *et al*. [35] mixed single-wall CNTs (SWCNTs) in 1-ethyl-3-methylimidazolium iodide to reach

an efficiency of 1.9%, compared to 0.4% without SWCNTs. These composites have been also proposed as electrodes for biosensors [36], electronic materials for flexible actuators [37], and other applications [38-40]. While CNT-ILs show promise to enhance the efficiency of DSCs, the molecular mechanisms that enable the improved performance are not completely clear [41]. CNTs typically agglomerate in solution and bundle by van der Waals forces [42]. However, some ILs have a high affinity to disperse bundles of CNTs [40,43-46]. Further, ILs are less volatile and toxic [47,23,48] than conventional solvents used to disperse CNTs without surfactants, such as N-Methyl-2-pyrrolidone (NMP) or dimethylformamide (DMF) [49,50]. Despite significant interest in CNT-ILs, the type of molecular interactions between ILs and CNTs are still controversial [40]. While some authors have suggested cation-π interactions between imidazolium-cation ILs and CNTs [51,44], others have indicated weak van der Waals interactions instead [52].

1.3 Summary and objectives

This thesis project is focused on improving the conversion efficiency of TECs by optimizing the cell design and dimensions, and by engineering novel electrodes and electrolytes.

In Chapter 2, I present a theoretical background with the fundamental equations that govern TECs. These include heat and mass transfer, fluid dynamics, electrode-kinetics and temperature-dependence of key properties of redox electrolytes, such as density, viscosity and electrode potential. These equations are simplified for low-viscosity and low-concentration electrolytes. However, they provide an accurate first-approximation for the performance of TECs. In Chapter 3, these equations are implemented and solved using a COMSOL model based on the properties of potassium

ferri/ferrocyanide electrolyte. The goals of this study are the identification of fundamental limitations in the conversion efficiency of TECs, the optimization of cell dimensions, and the power estimation of new designs (series stacking and flow-cell design). The results are published in ref. [53].

In Chapter 4, I experimentally explore the use of p and n-type CNT electrodes for TECs. The doping is carried out through a plasma treatment and optimized to reach 5% of boron and nitrogen, respectively. The changes in internal surface area, electrical and kinetic properties are characterized using impedance spectroscopy and cyclic voltammetry. The doping effects in the thermal-to-voltage conversion and electrical power are also tested in a U-glass TEC. The results are published in ref. [28].

In Chapter 5, I perform a spectroscopy study of IL-CNT composites by nuclear magnetic resonance (NMR) and impedance spectroscopy (EIS). The addition of CNTs to ILs electrolytes has been shown to improve the efficiency of DSCs in previous studies. The objective here is to understand the dielectric and percolation changes, as well as the molecular interactions in these mixtures. In this study, I compare the electrical contributions due to interfacial polarization and percolated networks of CNTs in common solvents and IILs. I also evaluate the possibility of ion pair dissociation induced by the CNTs and their effect on diffusion coefficients. The results are published in ref. [54].

In Chapter 6, I measure the electrical power of TECs using IILs mixed with MWCNTs. In particular, I test 1-ethyl-3-methylimidazolium bis(trisfluoromethanesulfonyl) amide ([EMIM][NTf_2]) mixed with cobalt redox couples, and a solvent-free redox ionic liquid, 1-methyl-3-propylimidazolium iodide ([PMIM][I]). The objective is to evaluate if the changes in interfacial polarization and ion pair

dissociation can overcome the open circuit reduction, and ultimately enhance the power of TECs.

CHAPTER 2. BACKGROUND

2.1 Introduction

TECs, or thermocells, are electrochemical devices that produce a steady electric current under an applied temperature difference between the electrodes (Fig 1.2A). The open circuit voltage depends on the reaction entropy of the redox electrolyte and temperature difference between the electrodes. The electrical current through an external load is maintained by mass transfer in the electrolyte driven by diffusion, convection, migration and thermal diffusion (Fig 1.2B). This chapter presents the governing equations in TECs for redox couples in low-viscosity solvents. These equations are simplified for diluted electrolytes, one-electron transfer kinetics, non-porous electrodes, and steady-state. This chapter also describes the experimental characterization techniques used throughout this work.

2.2 Governing equations

2.2.1 Heat transfer

At steady state, the temperature profile in the electrolyte is governed by [8]

$$\rho C_p \vec{u} \cdot \nabla T = \nabla \cdot (\kappa_s \nabla T + \sum D_i Q_i \nabla C_i) + S \qquad \text{eq. 2}$$

Heat is transferred to the TEC from a heat source, e.g., from the surface of a pipe in a power plant with hot water flowing through it. An electrolyte with a low thermal conductivity is required to obtain a maximum temperature difference across the electrodes. The maximum operative temperature of TECs is limited by the boiling point of water in aqueous solutions, or the volatility of the electrolyte in non-aqueous solutions. The minimum operative temperature is set by the solubility of the electrolyte at the cold

electrode. The temperature range for optimum performance of aqueous TECs is between 25 and 75^{o}C. The second term on the right side of **eq. 2** represents the Dufour effect. The attraction or repulsion of ions to the hot or cold electrode due to the Soret effect leads to an additional heat flux proportional to the diffusivity, concentration gradients, and Soret coefficients of the ions [55,56]. The last term on the right of equation 1, S, represents the sum of reversible heat due to electrochemical reactions and irreversible heat due to activation overpotentials and Joule heating. As noted by Quickenden [13], their contribution in TECs is relatively small, compared to the conductive-convective heat transfer, resulting in a negligible effect on temperature distribution or heat flux.

2.2.2 Thermodynamics

A reduction-oxidation (redox) reaction is described as

$$[\text{Reduced}]^{Z_R} \rightleftharpoons [\text{Oxidized}]^{Z_O} + (Z_R - Z_o)[e^-] \qquad \text{eq. 3}$$

Redox reactions at the electrode are thermodynamically balanced by

$$\Delta G^o_{rx} = \Delta H^o_{rx} - T^o \Delta S^o_{rx} \qquad \text{eq. 4}$$

In addition, the standard electrode potential with respect to the standard hydrogen electrode, and the standard reaction free energy are related by

$$E^o = \frac{-\Delta G^o_{rx}}{nF} \qquad \text{eq. 5}$$

Formally, concentrations at the electrode surface alter the electrode potential according to the Nernst equation. Thus, the electrode potential at any temperature is [57]

$$E = E^o + (T - T^o)\frac{\Delta S^o_{rx}}{nF} - \frac{RT}{nF}\ln\frac{C_R}{C_O} \qquad \text{eq. 6}$$

Enthalpy and entropy of reaction can be assumed constant in the temperature range of aqueous solutions.

When the cell is in open circuit or not connected to a load, the initial bulk concentrations are the same as those at the electrode surface. Conventionally, the ratio of oxidized and reduced species is 1. Also, electrolyte reacting at the anode and cathode is the same in TECs. If the standard electrode potential is independent of the electrode material, which is usually the case for redox couples used in TECs, we obtain the thermal-to-voltage conversion

$$V_{oc} = E_c - E_a = -\frac{\Delta S^o_{rx}(T_a - T_c)}{nF} \quad \text{eq. 7}$$

Hupp *et al.* reported values of standard redox reaction entropy for electrolytes as well as their respective standard electrode potentials [4]. It was found that the reaction entropy is negative, if the absolute charge of the reduced ion is larger than that of oxidized ion. The same publication reports the redox reaction entropy dependence on physicochemical parameters such as oxidation state, metal-atom radius and solvent molecules. The redox reaction entropy has not been reported to depend on the choice of electrode material.

2.2.3 Electrode kinetics

A simple expression for the electrode transfer rate constant is [58]

$$k = Z_e e^{-\frac{Ex_a}{RT}} \quad \text{eq. 8}$$

where Z_e is a constant frequency factor and Ex_a the total activation energy fit from the experimental values. The Butler-Volmer model describes the net electric current densities at the electrodes as [58]

$$j_a = nFk^o \exp\left[\frac{Ex_a}{R}\left(\frac{1}{T^o} - \frac{1}{T_a}\right)\right]\left[C_o^a \exp\left(\frac{-nF(1-\theta)\xi_a}{RT_a}\right) - C_R^a \exp\left(\frac{nF\theta\xi_a}{RT_a}\right)\right] \quad \text{eq. 9}$$

at the anode; and

$$j_c = nFk^o \exp\left[\frac{Ex_a}{R}\left(\frac{1}{T^o} - \frac{1}{T_c}\right)\right]\left[C_o^c \exp\left(\frac{-nF(1-\theta)\xi_c}{RT_c}\right) - C_R^c \exp\left(\frac{nF\theta\xi_c}{RT_c}\right)\right] \quad \text{eq. 10}$$

at the cathode. The overpotential, ξ, is the electrode potential with respect to its equilibrium value, which was given in **eq. 6**. Therefore, the anode and cathode overpotentials are

$$\xi_a = E_a - E_a^{eq} \quad \text{eq. 11}$$

$$\xi_c = E_c - E_c^{eq} \quad \text{eq. 12}$$

Eq. 9 and **10** show the dependence of these overpotentials on the concentration at the electrode surface and the rate constant k^o. The two contributions are defined as activation and concentration overpotentials. The activation overpotential is the overpotential when no mass transfer resistances appear, that is, the concentration at the surface is the same as in the bulk. The concentration overpotential is the actual concentration discrepancy at the surface. Electronic current continuity is satisfied by

$$\int_a j_a dA = -\int_c j_c dA \quad \text{eq. 13}$$

The double layer effect in the electrochemical kinetics requires further clarification. The effective overpotential that applies to the electrode kinetics of **eq. 9** and **10** is lower than that specified by these equations, because part of the overpotential difference is dissipated in a diffusive layer next to the reaction zone. However, as pointed out by Bockris [59], at high concentrations (above 0.1 M) the diffusive layer is so compact that most of the interphase potential affects the reaction zone only. Thus, the validity of equations **9-12** is retained for TECs.

2.2.4 Mass transfer

Electric current at the electrodes must be maintained by a flux of ions in the thermocell. The ionic density fluxes for the oxidized and reduced species, and the counter ions are [7]

$$\vec{N}_O = \underbrace{-D_O \nabla C_O}_{\text{diffusion}} \underbrace{-Z_O u_O F C_O \nabla \phi}_{\text{migration}} \underbrace{-\frac{Q_O}{RT^2} D_O C_O \nabla T}_{\text{thermal diffusion}} \underbrace{+C_O \vec{u}}_{\text{convection}} \quad \text{eq. 14}$$

$$\vec{N}_R = -D_R \nabla C_R - Z_R u_R F C_R \nabla \phi - \frac{Q_R}{RT^2} D_R C_R \nabla T + C_R \vec{u} \quad \text{eq. 15}$$

$$\vec{N}_{Cl} = 0 = -D_{Cl} \nabla C_{Cl} - Z_{Cl} u_{Cl} F C_{Cl} \nabla \phi - \frac{Q_{Cl}}{RT^2} D_{Cl} C_{Cl} \nabla T + C_{Cl} \vec{u} \quad \text{eq. 16}$$

The thermal diffusion, also known as the Soret effect, represents the ionic flux driven by a thermal gradient, generally from the hot to the cold side [55,56]. The Nernst-Einstein relationship is used to describe the mobility of ions

$$u_i = \frac{D_i F Z_i}{RT} \quad \text{eq. 17}$$

Eq. 14-16 are strictly valid for only infinitely dilute solutions. Under this approximation, the ion-ion interactions in the bulk are neglected and the activity values become equivalent to concentrations. Following the electrochemical literature, **eq. 14-16** are applied TECs because of its simplicity. Experimental diffusion data at high concentrations is used in an attempt to account for the discrepancy. The electrical neutrality condition

$$\frac{\nabla^2 \emptyset}{-F/\varepsilon} = \sum Z_i C_i = 0 \quad \text{eq. 18}$$

is applied in light of the large value of the ratio of F to ε in aqueous solutions [60]. Following the electrochemical reaction stoichiometry at the electrode

$$\vec{N}_O . \vec{n} = -\vec{N}_R . \vec{n} \quad \text{eq. 19}$$

where $\vec{n}$ is a normal unit vector perpendicular to the electrode. Whereas at the electrically insulated walls, $\vec{N}_i.\vec{n} = 0$, is applied. For every oxidation reaction at the hot electrode, a reduction happens at the cold electrode. Therefore, the total amount of reactants in the cell remains constant. This balance condition is expressed as

$$\int_T C_i d\mathcal{R}_T = \mathcal{R}_T C_i^* \quad \text{eq. 20}$$

Continuity at the electrodes is satisfied by the balance of ionic and electronic current density

$$j = \sum F\left(Z_R \vec{N}_R + Z_O \vec{N}_O\right).\vec{n} \quad \text{eq. 21}$$

There are no homogeneous reactions in the electrolytes conventionally used in TECs. Thus, at steady state, $\nabla.\vec{N}_i = 0$.

The resultant cell voltage is [58]

$$V_T = V_{oc} - \xi_a - \xi_c - \Delta\phi^s \quad \text{eq. 22}$$

2.2.5 Navier-Stokes equations for fluid flow

The mass conservation equation at steady state is

$$\nabla.(\rho\vec{u}) = 0 \quad \text{eq. 23}$$

In TECs, density variations with temperature (β_{T1}, β_{T2}) of the form

$$\rho = \beta_{T1} + \beta_{T2}T - \beta_{T3}T^2 \quad \text{eq. 24}$$

are used in this thesis [9,61]. I have omitted density changes due to electrolyte concentration because they represent a small contribution compared to temperature variations [7].

Steady-state momentum conservation in a laminar flow, when only gravitational forces are present, is described as

$$(\vec{u}.\nabla)\vec{u} = \upsilon\nabla^2\vec{u} + \vec{g}\left(\frac{\rho_o - \rho}{\rho_o}\right) \quad \text{eq. 25}$$

Following Boussinesq approximation, density changes are only considered in terms that contain gravity in the momentum conservation equations. The no-slip condition ($\vec{u} = 0$) is applied at every wall.

2.3 Experimental techniques

This section aims to cover the technical aspects of some of the characterization techniques used throughout this thesis. Rather than general, the explanation is focused on practical correlations between the measurements and material properties relevant to TECs.

2.3.1 Cyclic voltammetry

Several properties of a TEC electrolyte can be obtained by using cyclic voltammetry. Some of them are reaction kinetics, redox reaction entropy and diffusion coefficients. During cyclic voltammetry, an applied voltage is spanned from negative to positive values (or in the opposite direction) at a scan rate, typically, in the range of 10 to 100 mV/s. The experiment is performed in a 3-electrode system within a potential window that avoids reactions of the solvent. In the case of an equimolar potassium ferri/ferrocyanide solution (a one-electron redox reaction), two current peaks (anodic and cathodic) will appear, as shown in **Fig 2.1**. As the potential deviates away from the equilibrium potential, the current rises due to reactions at the electrode and diffusion from the bulk to the electrode. The current peak is the result of electrolyte depletion at the electrode surface. The potential separation of the redox peaks indicates the reversibility or kinetics of the reaction. A small potential peak separation means that the electrolyte depletion at the electrode happens quickly due to fast reactions. In contrast, sluggish kinetics require high electrode potentials before the surface concentration drops to zero.

A proper calibration system to check the reliability of the experimental set-up consists of a low concentrated solution (less than 10mM) of aqueous potassium ferri/ferrocyanide, 10 mV/s scan rate and platinum working electrodes. The potential peak separation on this experiment should be the ideal for a reversible one-electron transfer reaction, i.e. 59 mV.

The peak potential separation also depends on the solution resistance of the electrolyte due to migration between the reference and working electrode. A high ohmic resistance will require high electrode potentials away from equilibrium in order to reach the peak current, leading to large peak potential separations. When comparing peak potential separations, it is important to always compensate the current from the ohmic resistance. This can be done automatically with modern potentiostats.

If dealing with aqueous electrolytes, the reference electrode to choose is Ag/AgCl (a silver wire embedded in a saturated aqueous KCl solution). If the electrolyte is non-aqueous, the choice is Ag/Ag^+ (a silver wire embedded in a non-aqueous solvent). When dealing with ionic liquids, it is also possible to use a platinum pseudo-reference electrode instead of Ag/Ag^+, in order to avoid contamination of the ionic liquid. It is possible to experience a possible drift of the equilibrium potential when using non-aqueous or pseudo-reference electrodes, so special treatment and calibration is needed.

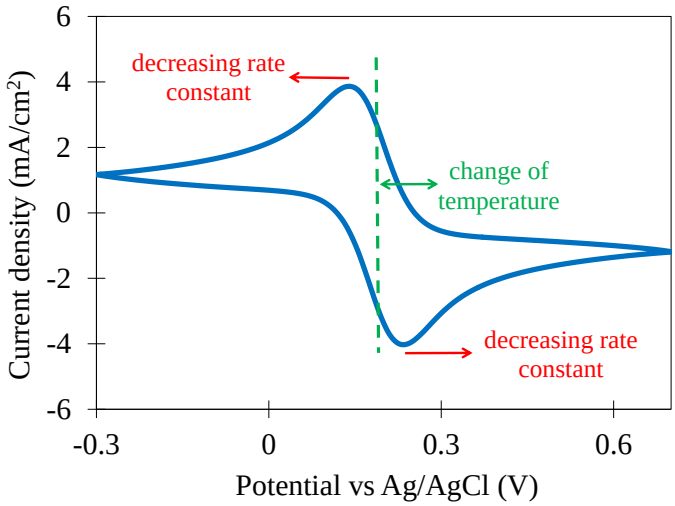

Fig. 2.1 Cyclic voltammetry of a 0.01M equimolar solution of $K_3Fe(CN)_6/K_4Fe(CN)_6$ at 100 mV/s and 20 °C. Voltage scan starts at -0.3 V (with respect to a Ag/AgCl reference electrode). IR compensation was applied before every run. The plot shows the trend of the peak-potential separation as the reaction rate constant decreases. The plot also indicates that the equilibrium potential (average of the peak potentials) shifts depending on the changes in temperature.

Ohmic (IR) compensation is performed internally in the potentiostat. As shown in

$$V_T = V_{oc} - \xi_a - \xi_c - \Delta\phi^s \qquad \text{eq. 22}$$

the total cell voltage V_T is equal to the open circuit voltage, V_{oc}, minus the activation overpotentials, ξ, and ohmic drop, $\Delta\phi^s$. The ohmic drop is equal to the ohmic resistance of the electrolyte times the current that passes through. By applying an ohmic compensation in the experiment, the total cell voltage depends only on the overpotentials at the electrodes and the open circuit voltage. In a 3-electrode configuration, the ohmic resistance of the electrolyte depends on the separation of the working and reference electrode, as well as, in the concentration and mobility of the ions. In 0.4M potassium

ferri/ferrocyanide solutions, the ohmic resistance can represent 3 to 5% of the total cell resistance in thermocells that are 2 mm long. However, in thermocells with electrodes separated 10 cm apart, the ohmic resistance can represent 50 to 60 % of the total cell resistance.

The estimation of reaction entropies is based on the shifting of the equilibrium potential at different temperatures. In an equimolar solution, the semi-sum of the potential peaks is the equilibrium potential of the reaction, E°. The experiment is performed in a solution at a uniform temperature. As the temperature increases, the equilibrium potential will shift towards higher or lower potentials, depending on whether the redox reaction entropy is negative or positive, respectively. After correcting for the shift of the reference electrode potential, the redox reaction entropy, ΔS_{rx}, can then be found according to

$$\Delta S_{rx} = nF\frac{dE^o}{dT} = \frac{\left(E_{T_1}^{anode}+E_{T_1}^{cathode}\right)-\left(E_{T_2}^{anode}+E_{T_2}^{cathode}\right)}{2(T_1-T_2)} \quad \text{eq. 26}$$

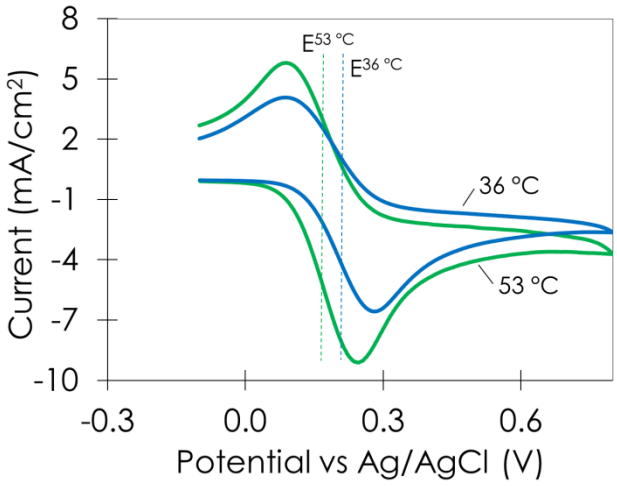

Fig. 2.2 Cyclic voltammetry of a 0.01M equimolar solution of $K_3Fe(CN)_6/K_4Fe(CN)_6$ at 36 °C and 53 °C. Voltage scan starts at -0.1 V (with respect to a Ag/AgCl reference electrode). IR compensation was applied before every run. The plot shows the equilibration potential shift with temperature.

To estimate diffusion coefficients, cyclic voltammetry is carried out with a platinum working electrode of 10 um diameter (thus, also called microvoltammetry). But the diameter and material could vary. Due to the small surface area of the electrode, the ions reach a steady-state diffusion radial to the electrode. The result is then a steady current under an applied voltage in relatively short measuring times (**Fig. 2.3**). Because of the small surface area of the electrode, the ohmic and charge transfer resistances are significantly high, leading to small currents that do not affect the total current. The measured current then only depends on the ionic diffusion near the electrode. The diffusive layer thickness during the measurement is approximately the same as the diameter of the microelectrode [62].

A typical experiment is a cyclic voltammetry spanning from anodic to cathodic potentials at a scan rate of 10 mV/s, for 3 cycles. At high anodic and cathodic potentials, the current will reach a steady state proportional to the diffusion of the ions, according to the formula:

$$I_{ss} = 4nFrDC \qquad \text{eq. 27}$$

where n is the number of electrons transferred, ‘r’ is the radius of the microelectrode, ‘D’ is the ionic diffusion coefficient, ‘F’ is the Faraday constant, and ‘C’ is the bulk concentration of the electrolyte. The reader is referred to [63,62,64-70] for further basic information on these characterization techniques.

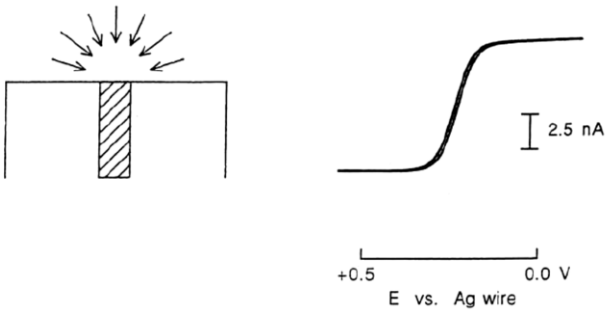

Fig. 2.3 Radial diffusion and ultramicroelectrode cyclic voltammetry in 1mM ferrocene solution at 50 mV/s [62].

2.3.2 Electrochemical impedance spectroscopy

Impedance spectroscopy can be used to estimate the ohmic resistance of the electrolyte. In impedance spectroscopy, an alternating voltage signal is applied to the electrolyte. The signal is varied from high to low frequencies, and the impedances are recorded. The impedance of the system depends on the frequency of the signal because of different electronic and mass transfer mechanisms. For example, the bulk capacitance of

the electrolyte, which depends on the molecular reorientation and induced dipoles in the electrolyte, can only be estimated experimentally at frequencies higher than 10^4 Hz; while ionic diffusion coefficients are estimated at frequencies lower than 1Hz [71].

The optimum amplitude of the AC signal is a tradeoff between a high signal-to-noise ratio and linearity between the current and voltage [72]. A typical AC signal is between 10 to 15 mV. Along with the AC signal, a constant voltage bias is also applied, but typically is set to 0 V. If, however, the bias voltage is different from 0, it is important to set a preconditioning run at the same bias voltage before the AC signal is applied.

An established model for aqueous redox electrolytes in nonporous electrodes is represented in **Fig. 2.4**. In this circuit model, C_b represents the bulk resistance, R_b is the bulk resistance of the electrolyte, R_{ct} is the charge transfer resistance, W is the Warburg element and Q_{dl} is a constant-phase element at the double layer of the electrolyte/electrode interface. Q_{dl} is a non-ideal capacitor with a phase lower than 90° that aims to account for the surface roughness of the electrode and other inhomogeneous properties at the double layer. W is an element that represents mass transfer resistances due to diffusion near the electrode, while R_{ct} represents the activation polarizations of the reactions.

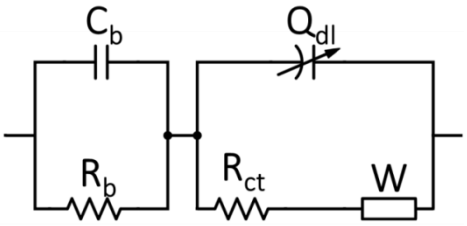

Fig. 2.4 Electrochemical model for a redox electrolyte with nonporous electrodes.

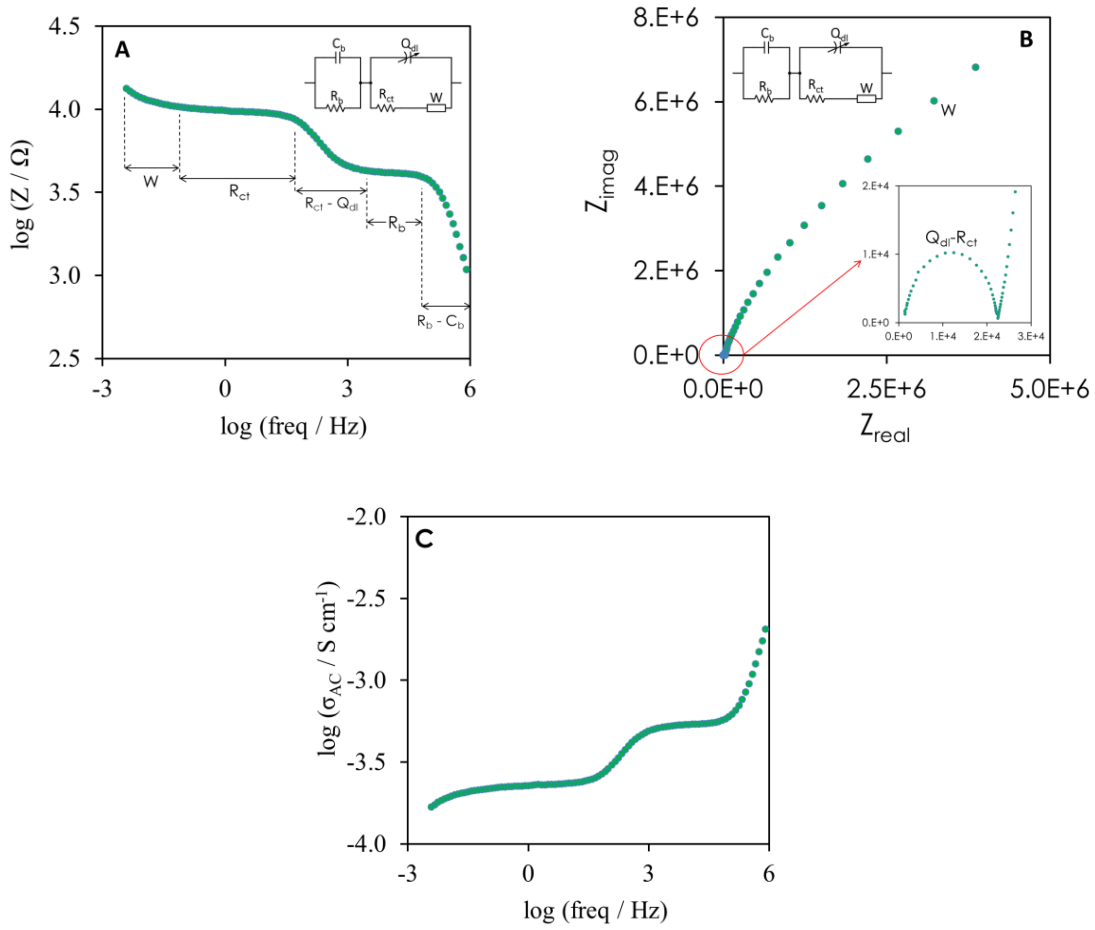

Fig. 2.5 a) Bode and b) Nyquist plots for a redox IL showing the frequency range for each model component. c) Conversion of the impedance spectra of figure a to conductivity, σ_{AC}, using equations **28** and **29**.

Impedance spectroscopy analysis can be a complicated study depending on the properties the researcher would like to determine. Some other properties that can be obtained are porosity of the electrodes, diffusion coefficient in solid electrolytes and additional reactions, but those require more complex and extensive models.

In TECs, the ohmic resistance of the electrolyte is an important property, because it can limit the electric power. It is also the most reliable property to be estimated by impedance spectroscopy. As shown in the model of **Fig. 2.5**, the high-frequency spectrum is determined by the bulk capacitance (C_b) and the electrolyte resistance (R_b) bracket. This is because the bulk capacitance is 2 to 3 orders of magnitude higher than the capacitance at the double layer, depending on the dimensions of the cell. At frequencies between 10^5 and 10^3 Hz, the bulk capacitance is always charged, thus the impedance is constant and depends only on the electrolyte ohmic resistance.

The electrode design plays an important role in estimating the electrical resistivity of the electrolyte. Because of edge effects, the electric flux will not be entirely uniform between the electrodes. The geometry factor of the cell can be obtained by using a standard electrolyte solution of known resistance. An aqueous KCl solution at 0.1 or 0.01M can be used for calibration. The ohmic resistivities at different temperatures are reported in the CRC Handbook of Chemistry and Physics [73]. The geometry factor is

$$\mathrm{GF} = \frac{\rho_{\mathrm{KCl}}}{\mathrm{R_{KCl}}} \qquad \text{eq. 28}$$

where ρ_{KCl} is the resistivity reported for KCl and R_{KCl} is the resistance measured. Then, the resistivity of the new electrolyte is

$$\rho_{\mathrm{electrolyte}} = (\mathrm{GF})\mathrm{R_{electrolyte}} \qquad \text{eq. 29}$$

Fig. 2.5c shows the conversion of the impedance, Z, spectra measured to conductivity values, σ_{AC}, using the calibrated geometry factor, GF. The reader is referred to [73,71,74,72] for further basic information on these characterization techniques.

2.3.3 TEC power measurement

Three of the designs to test the performance of TECs are the U-glass cell design, the coin cell design and the stirring cell.

U-glass cell design

TEC power measurements are performed in a U-shaped glass filled with the electrolyte only, as shown in **Fig. 2.6**. The temperature of one compartment is raised with a wire heater, while the other is controlled at room temperature with a chiller. On each compartment there is a Teflon-coated thermocouple that is immersed in the solution. The electrodes are also immersed without interfering with the thermocouples. It is important to check that the connectors for the electrodes do not touch the electrolyte, because such contact might induce additional reactions. As a check point, the open circuit voltage without a thermal gradient should be zero, or within the experimental uncertainty error. A potentiostat can be used to monitor the transients of voltage and current. The 3-electrode configuration can be adapted to a 2-electrode, by plugging the reference electrode together with the counter electrode, preferably in the hot electrode. As the temperature difference increases, the open circuit voltage should consistently increase or decrease, depending on the sign of the reaction entropy of the electrolyte. As another checkpoint, the open circuit voltage should go back to zero once the thermal gradient is removed. In a U-glass design, the thermal-to-voltage measurement is the most reliable property that can

be obtained. If however, the researcher wants to compare the power densities, it is important to obtain a good control in the electrode separation, surface area and homogeneity of the electrodes.

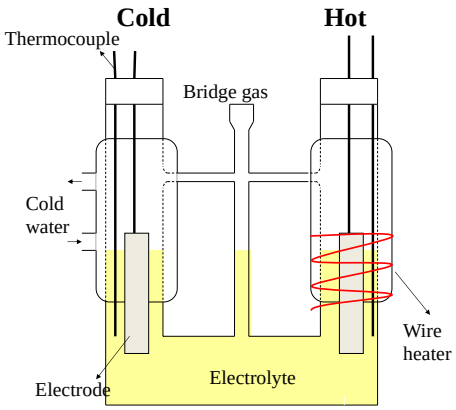

Fig. 2.6 U-shape glass cell for measurement of thermal-to-voltage conversion.

Coin cell design

TEC power measurements are performed between two metal blocks and using a coin-size TEC, as shown in **Fig. 2.7**. The electrodes are deposited in the stainless steel coin-size substrates. In this thesis, the electrodes consisted of e-beam evaporated platinum (100 nm), or MWCNTs grown in a Ni/Ti/Al/Fe catalyst [75], or buckypaper electrodes (purchased from Nanocomp, Inc.) connected to the substrate with carbon paste. **Fig. 2.7c** shows the coin-shape substrates before and after crimping. The smaller substrate (~20 mm diameter) is enclosed with a polypropylene gasket (thermal conductivity ≈ 0.1 W/m-K). The bigger substrate (~22 mm diameter) is fully filled with electrolyte, while the smaller substrate is wetted with some electrolyte, avoiding air gaps with a pipette. In this thesis, I did not include any separator or membrane in the

electrolyte. The smaller substrate is plugged in the bigger substrate, and then crimped at a pressure of 250 psi for 30 seconds. The coin cells and crimper are then cleaned with acetone. Optionally, some electrolyte leakage can be prevented by adding super glue at the joints. The thermocouples are adhered to the metal blocks with kapton tape, and the coin cell is sandwiched between the metal blocks. One of the blocks is connected to a thermal pad, while the other is connected to the chiller. Again as a checkpoint, the open circuit voltage without a thermal gradient should be close to zero. If this is not the case, the problem could be a leakage of electrolyte or super glue reacting with the metal blocks, or corrosion of the electrolyte with the substrate electrodes. Instabilities in the voltage could also be due to remaining air gaps in the crimped coin cell. As the temperature difference increases, the open circuit voltage should consistently increase or decrease, depending on the sign of the reaction entropy of the electrolyte. Unlike the U-glass cell design, the thermocouples are connected to the metal blocks rather than immersed in the electrolyte. Thus, the temperature measurements in the coin cell do not include the thermal losses at the interface. As consequence, the thermal-to-voltage conversion measured for the same electrode/electrolyte combination will be lower in a coin cell design than in the U-glass cell design. Once the thermal gradient and voltage have reached a steady state, the power density measurements can be acquired. As another checkpoint, the open circuit voltage should go back to zero once the thermal gradient is removed.

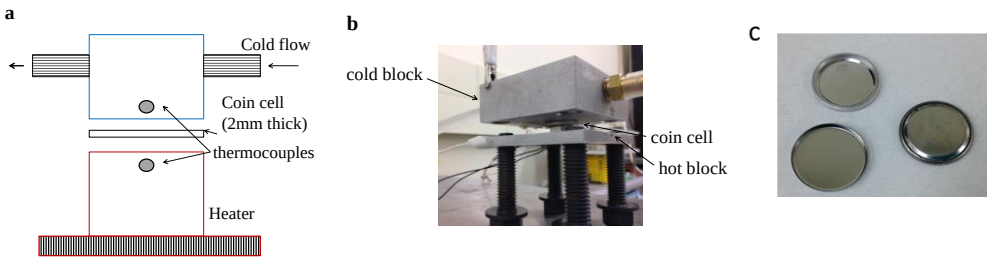

Fig. 2.7 Schematic (a) and photograph picture (b) of the experimental set-up for the performance testing of coin TECs. c) Photograph of coin cells before and after crimped.

Stirring cell design

TEC power measurements are performed in a water jacket cell and two vertical electrodes, as shown in **Fig. 2.8**. A chiller is connected to the water jacket, controlling the overall temperature of the cell. A magnetic bar is included in the electrolyte, and stirred with a controlled rate by the plate at the bottom. In order to create the thermoelectric effect, one of the electrodes is heated with thin film heaters (1.6 W/cm^2 each) connected to a copper jacket at the top of the electrode. Forced convection in the electrolyte is designed to make the diffusive boundary layers thinner, and force the system to become ohmic limited. Even though forced convection reduces thermal gradients between the electrodes, a thermal gradient at the boundary layer of the hot electrode and electrolyte still exists. The thermoelectric effect is maintained because redox reactions happen at the boundary layers of the electrodes. In this thesis, the electrodes used are graphite electrodes of 6.1 mm in diameter. Graphite is used because of its high thermal and electrical conductivity. Due to the size of the copper jacket and electrodes, it takes approximately 3 hours to reach steady state on the initial open circuit voltage. Upon

stirring of the cell, sampling of the steady state open circuit voltage and short circuit current takes 30 min. As the stirring rate increases, forced convection cools down the electrode surface temperature, and the open circuit voltage decreases. This trend can be used as a checkpoint of the experimental set-up.

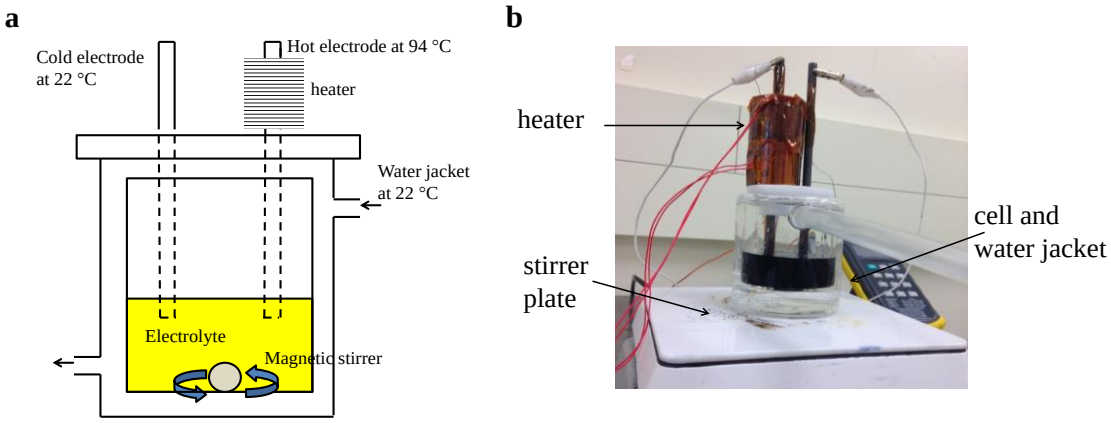

Fig. 2.8 Schematic (a) and photograph picture (b) of the experimental set-up for the performance testing of stirring TECs.

2.3.4 Nuclear magnetic resonance (NMR) spectroscopy

NMR spectroscopy allows us to determe not only the chemical composition of a liquid, but also its molecular structure. It is also possible to estimate intermolecular interactions in nanofluids, as shown later in **CHAPTER 5**. The samples are prepared in NMR tubes of 5mm in diameter. The tubes have to be properly cleaned and dried, because small impurities can be easily detected in the NMR spectra. The mixture has to be homogeneous and without air gaps.

The NMR experiments in this thesis were performed at the NMR center at Georgia Tech (http://ww2.chemistry.gatech.edu/~gelbaum/nmr/nmr.html) using the Bruker AV3-400 NMR spectrometer. The spectrometer is equipped with a DIFF50 probe

that allows magnetic field gradients greater than 2000 G/cm. Before running 1D and diffusion experiments, the spectrometer is calibrated using an external standard solution of 0.1% 3-Trimethylsilylpropane sulfonic acid in D_2O containing 20% H_2O.

In a 1D NMR experiment, a molecule absorbs electromagnetic radiation in a frequency range, which is correlated to a chemical shift (**Fig. 2.9)**. For the same type of isotope, the type of interaction with the other atom determines the chemical shift at which the isotope emits electromagnetic radiation. For example, a hydrogen isotope covalently bonded to oxygen will have a higher chemical shift than a hydrogen isotope in a methyl group (**Fig. 2.9**). When adding nanoparticles to a fluid, the shielding (chemical shifts to lower values) or deshielding (shift to high chemical shifts) is an indication of electronic interactions between the nanoparticles and the fluid.

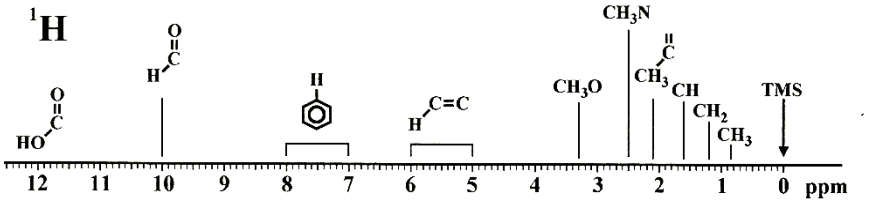

Fig. 2.9 Chemical shifts of ^1H affected by the proximity of different electronegative atoms or groups [76].

Diffusion experiments on NMR-sensitive nuclei (^1H, ^{13}C, ^{15}N and ^{19}F) can be performed using the pulsed gradient spin-echo (PGSE) technique. In general, a magnetic gradient pulse of δ duration and G magnetic strength is imposed on a 90° radio frequency signal. The pulse disperses the magnetization of the spins in a well-defined space. The signal is then refocused by applying an inverted (180°) radio frequency signal after a time delay (Δ). It then spins, and the atoms and molecules diffuse away from the

magnetization zone, in this way the refocused signal is attenuated. The attenuated signal is measured at different magnetic field gradients (**Fig. 2.10**), and the diffusion coefficients of the isotopes (*D*) are estimated according to

$$\ln\left(\frac{I}{I_o}\right) = -(\gamma\delta)^2 G^2 \left(\Delta - \frac{\delta}{3}\right) D \qquad \text{eq. 30}$$

where I/I_o is the ratio of the intensities with and without the gradient pulses, and γ is the gyromagnetic ratio. The optimum magnetic field strength G and delay time Δ depend on the diffusion coefficient of the isotope. Low diffusion coefficients require high magnetic field strengths or longer delay times. The reader is referred to [76-79] for further basic information on these characterization techniques.

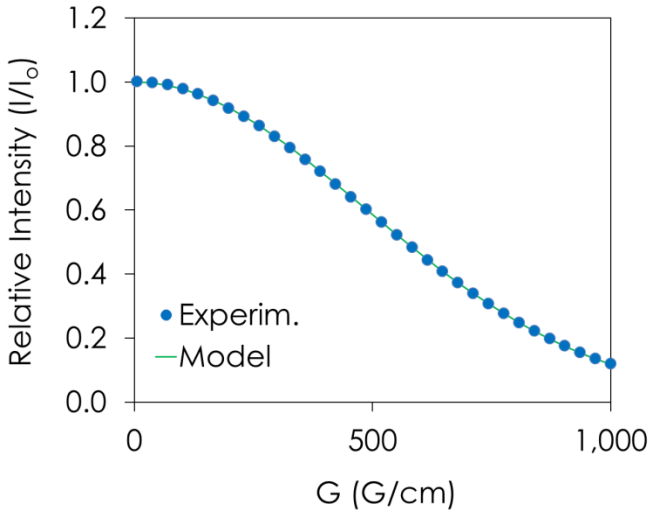

Fig. 2.10 Experimental and model (**eq. 30**) relative intensity of a 1H NMR resonance peak at several magnetic field strengths (G), to determine diffusion coefficients.

CHAPTER 3. MODELING AND OPTIMIZATION OF THERMO-ELECTROCHEMICAL CELLS

3.1 Introduction

In this chapter, the fundamental governing equations for mass and heat transfer, fluid dynamics, and electrokinetics in TECs, presented in **Section 2.2,** are solved numerically using COMSOL Multiphysics®. A snapshot of the model used is included in the Appendix. This report seeks to extend the optimization of thermocells to the dimensions and designs of practical cell configurations. In addition, this report highlights the critical limitations on power generation and conversion efficiency, as well as, the effect of natural convection in mass and heat transfer in thermocells. The performance of stacking cells in series is later evaluated. Finally, I evaluate the performance of a thermocell design with forced convection of the electrolyte, i.e., a flow cell.

3.2 Performance in conventional TECs

This section describes quantitative insights of the output electrical power and heat needed in convectional TECs, as well as the upper limits in efficiencies of an optimized cell. Conventional TECs do not employ forced convection; thus the bulk flow of the electrolyte is only buoyancy driven. In addition, conventional TECs use an equimolar aqueous solution of potassium ferri/ferrocyanide due to its high reaction entropy. The maximum concentration of potassium ferri/ferocyanide used here is 0.4 M because this is the solubility limit in the electrolyte. No supporting electrolyte is added since it would reduce the solubility of the redox couple. Platinum or MWCNT are used as electrodes because of their high kinetic reactivity and because they have been used in prior

experimental work [28,14]. A 2-D model, with the x-axis in the direction of diffusion and the y-axis in the direction of the electrode surfaces, is considered to approximate a coin cell design [14]. These designs usually have a thickness of approximately 1 mm. All parameters used in the simulation are presented in **Table 3.1**.

Fig. 3.1A shows the current and power density as a function of the cell voltage. The maximum mean power density is reached at a current strength of roughly half of the open-circuit potential. Unless specified otherwise, the power density and heat flux density reported in the following simulations are the average along the electrodes. Thus, the term 'mean' is omitted. An analysis of the kinetic and mass transfer resistances (**Fig. 3.1B**) depicts the cathodic concentration overpotential as the major limitation in conventional thermocells. In other words, the current density is mainly limited by the low ionic diffusion at the cold electrode. As a consequence, there is a greater consumption/generation of oxidized/reduced species at this electrode (**Fig. 3.1C**). At high current densities, the electrolyte at the cold electrode is depleted and the current density approaches its limiting value. The reversibility of the electrodes translates into small activation overpotentials compared to the total potential drop (**Fig. 3.1B**). Temperature, velocities and concentration profiles under natural convection due to temperature and concentration gradients are shown in **Fig. 3.1D-F**.

Table 3.1 Parameters used in the stagnant TEC simulation with potassium ferri/ferrocyanide as electrolyte.

Parameter [Units]	Value
Cell height and length [mm]	1
Electrolyte heat capacity [J $kg^{-1}K^{-1}$] [9]	$C_p = 4187$
Initial $K_3Fe(CN)_6$/ $K_4Fe(CN)_6$ concentration [mol m^{-3}]	400/400
Density [kg m^{-3}] [61][a]	$1063 + 0.546T - 0.00147T^2$
Diffusion coefficient [m^2 s^{-1}][61][b]	$(62.66-0.5336T+1.1482 \times 10^{-3}T^2) \times 10^{-10}$
Rate constant activation energy [kJ mol^{-1}][5]	$Ex_a = 14.644$
Standard rate constant [m s^{-1}] [80][c]	$k^o = 0.6e\text{-}5$
Electrolyte thermal conductivity [W $m^{-1}K^{-1}$] [9]	$\kappa_s = 0.6$
Anode temperature [K]	$T_a=360$
Cathode temperature [K]	$T_c=300$
kinematic viscosity [cm^2 s] [61]	$\nu = \exp(-4.818-1808T^{-1} + 5.616e5T^{-2})$
Thermal-to-voltage conversion [mV K^{-1}] [28]	1.5

[a] In lack of reported values at 0.4M, the electrolyte density at 0.2M was used.

[b] The diffusion coefficients and their temperature dependence of the oxidized and reduced species were assumed equal. In lack of reported values at 0.4M, the diffusion coefficient at 0.2M was used.

[c] The rate constant reported at 0.4M was used.

Table 3.2 Power and heat flux density with and without natural convection included in the simulations with a 1 mm square cell

	With natural convection	Without natural convection
Maximum power density [W m^{-2}]	4.61	0.56
Input heat flux density [W m^{-2}]	56050	36000
Relative efficiency [%]	0.049	0.009

Natural convection compresses the boundary diffusive layer (**Fig. 3.1F**), thus increasing the ionic flux density at the electrodes and ultimately the power density, as shown in **Table 3.2**. Similarly, this electrolyte recirculation increases the input heat flux needed at the hot electrode to maintain the temperature difference set between the two electrodes. The strength of natural convection on the heat flux density and current density is estimated by the Nusselt and Sherwood number, respectively. For finite anode-cathode separations, the dimensionless Nusselt and Sherwood correlations are [81]

$$\mathrm{Nu} = \frac{q}{q_{wc}} = 0.19(\mathrm{GrPr})^{1/3}\ ,\ \mathrm{Sh} = \frac{j}{j_{wc}} = 0.19(\mathrm{GrSc})^{1/3} \qquad \text{eq. 31}$$

The fluid is characterized by the Grashof (Gr), Schmidt (Sc) and Prandtl (Pr) number [81]

$$\mathrm{Gr} = \frac{gL^3(\rho_o-\rho)}{\nu^2\rho_o}\ ,\ \mathrm{Sc} = \frac{\nu}{D}\ ,\ \mathrm{Pr} = \frac{\nu\rho C_p}{\kappa_s} \qquad \text{eq. 32}$$

where the characteristic length, L, is the anode-cathode separation. Combining **eq. 1, 31 and 32**, the conversion efficiency can then be expressed as

$$\eta\ [\%] = \frac{V_T \cdot j}{q}(100) = \frac{V_T \cdot j_{wc} \cdot \mathrm{Sh}}{q_{wc} \cdot \mathrm{Nu}}(100) = \eta_{wc} \cdot \left(\frac{\alpha}{D}\right)^{1/3} \qquad \text{eq. 33}$$

where $\alpha/_D$ ratio is also known as the Lewis (Le) number. The Rayleigh number was at most in the order of 10^7, that is, at least 2 orders of magnitude lower than the critical transition value from laminar to turbulent flow.

For the conditions and cell dimensions given in **Table 3.1** (1 mm square cell), the power density increases 8 times because of natural convection. On the other hand, the input heat flux density at the anode is only 1.5 times higher due to natural convection. The higher power density increase is due to the low diffusion coefficients of redox species in comparison to their thermal diffusivities. The average diffusion coefficient (D) of potassium ferri/ferrocyanide is 4 x 10^{-10} m^2 s^{-1}, while their thermal diffusivity $\left(\alpha = \frac{\kappa_s}{\rho C_p}\right)$ is 1.4 x 10^{-7} m^2 s^{-1}. The difference translates into the lack of a temperature boundary layer (**Fig. 3.1D**) and a smaller input heat flux increase due to natural convection. Also, the buoyancy effects are due to the temperature gradients rather than to the net concentration (oxidized plus reduced species) gradients. The Soret and Dufour effects in aqueous potassium ferri/ferrocyanide solutions were omitted because their relevance on mass and heat transport is relatively small. The heat of transport coefficients of potassium ferri and ferrocyanide in aqueous solutions are about 8.0 kJ mol^{-1} [82].

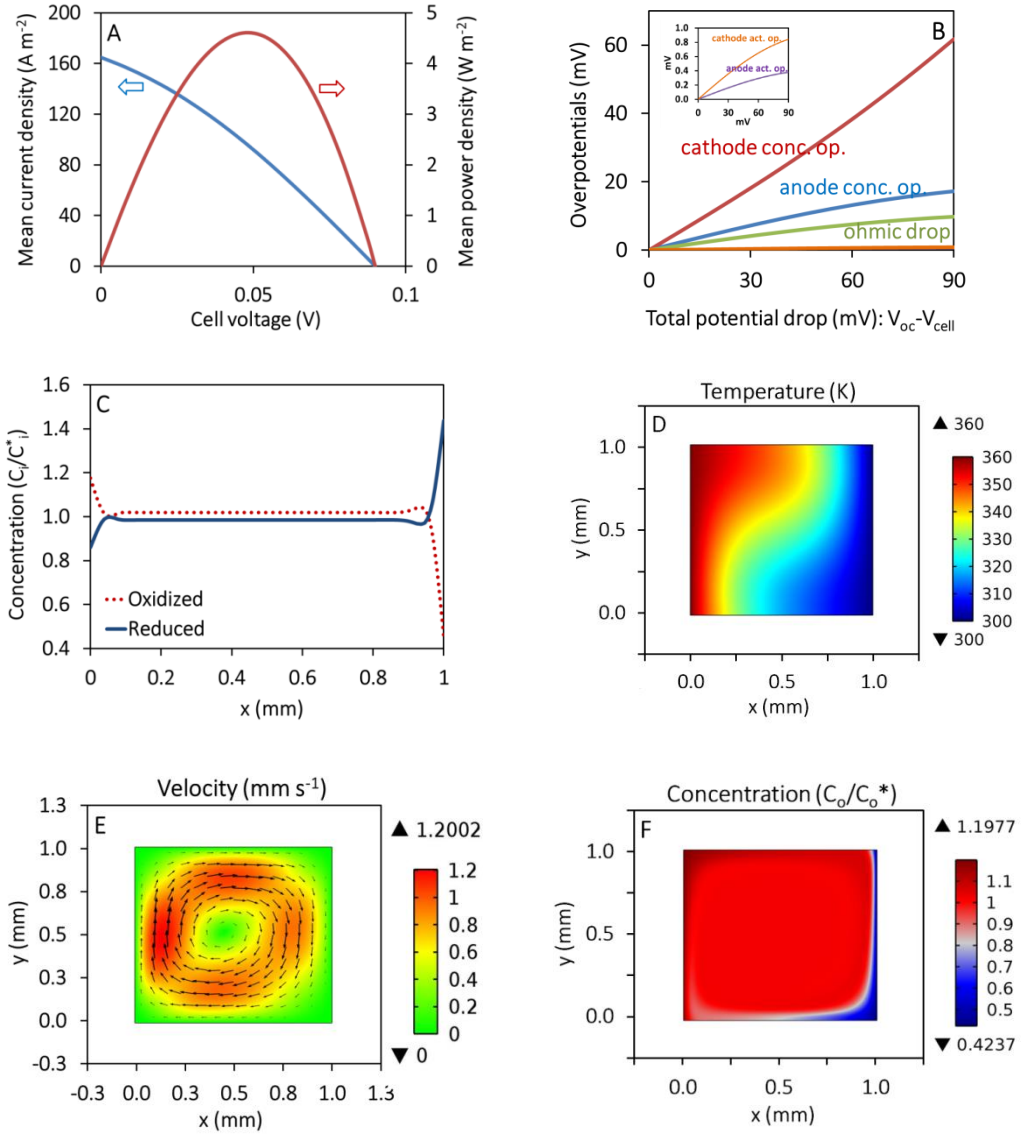

Fig. 3.1 A: Current and power density vs cell voltage. B: Overpotential breakdown (cathode and anode concentration overpotential, and ohmic potential drop; inset shows the cathode and anode activation overpotential). C to F show contour plots at maximum output power for C: normalized ionic concentration distribution along the center of the cell (y=height/2), D: temperature (K), E: velocity (mm s^{-1}) and direction, F: normalized (with respect to initial concentration) oxidized concentration. These measurements were

obtained using a square thermocell of 1 mm length with electrodes placed vertically, anode at the left side (refer to **Fig. 1.2B**)

3.3 Validation

The multiphysics model and parameters used were tested with experimental values reported by Ikeshoji and Mua *et al*. [10,83]. **Table 3.3** shows the dependence of short circuit current on electrode separation for an equimolar potassium ferri/ferrocyanide solution and supporting electrolyte. At electrode separations greater than 1 cm, the electric current is mainly limited by the ohmic resistance of the solution, and the calculated short circuit current fairly matches the experimental values. I found a high overestimation of electric current at an electrode separation of 1 mm; i.e., when the transport is driven mainly by conductive and convective forces. The lower experimental short circuit currents are probably due to the additional boundary layers at the side walls of the cylindrical thermocell, which are not considered in the 2-D model. Natural convection can be suppressed by placing the hot electrode above the cold electrode. The experimental and calculated changes of electric power density with the orientation of the cell are shown in **Table 3.3**. In addition, the Sherwood and Nusselt numbers for a square TEC of 1 mm length (**Fig. 3.2A**) are in agreement with the computational results of Ikeshoji et al. (**Fig. 7** of Ref. [8]).

In all simulations, each boundary was meshed with a minimum element size of 2 x 10^{-7} m (to assure grid independence), linearly distributed from a fine grid near the boundary to a course grid near the center of the cell. The maximum element ratio (the ratio of the biggest and smallest element) was 20. If the minimum element size is

decreased to 1 x 10^{-7} m, the results change less than 2%. The simulations converged in less than 100 iterations with a relative tolerance of 0.001 and using a Multifrontal Massively Parallel sparse direct solver (MUMPS).

Table 3.3 Experimental and calculated short circuit current (J_{sc}) and maximum electric power density (P_m)

Author: Ikeshoji et al. [10] T_a-T_c = 72 °C , T_c = 5.4 °C , $[K_3Fe(CN)_6] = [K_4Fe(CN)_6]$ = 0.01 M , platinum electrodes of 9 mm diameter, electrode separation of 1 mm [a]		
	Exp. P_m (W m^{-2})	Calc. P_m with our model (W m^{-2})
Conductive (hot-above-cold)	0.028	0.03
Conductive-Convective (cold-above-hot)	0.074	0.09

Author: Mua et al. [83] T_a-T_c = 40 °C , T_c = 20 °C , $[K_3Fe(CN)_6] = [K_4Fe(CN)_6]$ = 0.26 M , [KCl] = 0.8 M , platinum electrodes of 1cm^2 surface area, cold-above-hot electrode configuration [a]		
Electrode distance (cm)	Exp. J_{sc} (A m^{-2})	Calc. J_{sc} with our model (A m^{-2})
0.1	32	38.2
3	14	16.9
5	10	11.8
10	6	7.0
20	3	3.6

[a] The diffusion, rate constant, viscosity and density parameters at 0.01M; and the addition of supporting electrolyte were considered in the simulations.

3.4 Optimization of cell dimensions

The strength of natural convection with cell aspect ratio (height/length) at a fixed length (1 mm) is depicted in **Fig. 3.2A**. At small aspect ratios, convection of heat and mass is small (Nu→1 and Sh→1). As the aspect ratio increases, convective heat and mass transfer becomes relevant (Sh and Nu increase). An optimum efficiency is found in this transition. Similarly, as the cell length increases, heat conduction decreases and the optimum aspect ratio becomes smaller (**Fig. 3.2B**). Sherwood numbers were calculated as the ratio of current density considering natural convection over current density without natural convection from the simulations. Similarly, Nusselt numbers were calculated as the ratio of heat flux considering natural convection over heat flux without natural convection from the simulations.

Fig. 3.3A shows a non-monotonic change of the relative efficiency as the cell length is increased while the aspect ratio is held constant at 1. At small cell lengths, the decrease of power and input heat flux density is linear because conduction and diffusive mass transfer are dominant. The inflection point at 0.1 mm and 0.5 mm in the power and heat flux density curve, respectively, indicates the compression of boundary layers because of natural convection. The efficiency increases at 0.1 mm because of a secondary effect of temperature gradients in ionic transfer (the primary effect being natural convection). As shown in **eq. 33**, the effect of natural convection on the efficiency is determined by the ratio of thermal and ionic diffusivities, $\alpha/_D$ (Lewis number). The diffusion coefficients near the cold electrode boundary layer should be considered in the Lewis number, because cathodic concentration overpotentials limit the current density (**Fig. 3.1B**). As the cell length increases, temperature gradients decrease and the average

diffusion coefficient at the cathode boundary layer decreases. Thus, convective forces become stronger at the cold electrode. A maximum efficiency is found at 1 mm thermocell length because as the length increases the ohmic potential drop begins to reduce the available cell voltage (**Fig. 3.3B**). Convection is the transport of bulk solution which, by electrical neutrality (**eq. 18**), has zero net charge. Thus, any forced or free convection would not create a separation of charges between the electrodes and would not reduce the ohmic resistance.

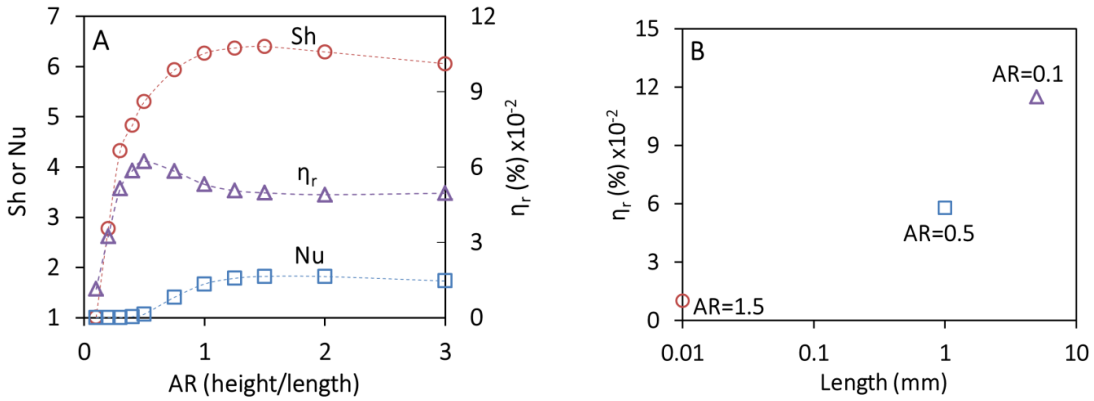

Fig. 3.2 Effect of aspect ratio (height/length) on natural convection. A: Sherwood (Sh), Nusselt (Nu) and relative efficiency η_r; cell length fixed at 1mm. B: Conversion efficiency and optimum aspect ratio at several cell lengths.

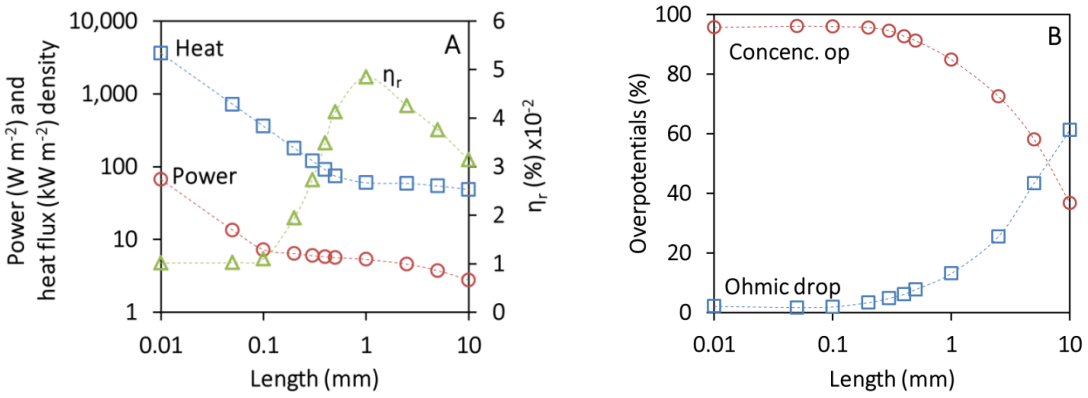

Fig. 3.3 Cell length parametric study. A: Maximum power, input heat flux density and conversion efficiency η_r. B: Overpotential distribution at maximum power operational points. Aspect ratio held at 1.

3.5 Series stacking

Implementation of TECs to waste heat sources would require thicker cells in order to assure a maximum temperature difference. I consider the case of a single cell (5 mm length and 5 mm height) that is split in equal sized cells and stacked in series. In a series configuration stacking as shown in **Fig. 3.4**, the input heat flux coming out from the hotter inner cell is transferred to the next inner cell (since the side walls are considered insulated). The total conversion efficiency in a series configuration is then

$$\eta\,[\%] = \frac{\sum_{i=1}^{N} P_i}{\text{Heat input}}(100) = \sum_{i=1}^{N} \eta_i \qquad \text{eq. 34}$$

Input heat flux and power density decrease after the cell splitting (**Fig. 3.5A**), because the reduced length of the intermediate cells decreases the natural convection in them (Grashof number decreases). **Fig. 3.5B** compares the efficiency of each intermediate cell in a 2-series stack as well as in the single configuration. The current density of the hotter intermediate cell is discontinued because the limit of the cooler cell

is reached. The maximum efficiency in the coupled cell is found by the efficiency sum of the intermediate cells at the same current density. Hotter intermediate cells have higher efficiency because ionic diffusive flux increases as its mean temperature increases, and because the loss of convective forces is less critical in the hotter intermediate cells (high diffusion coefficient and low Sherwood number). However, consecutive cell splitting reduces the limiting current of the colder intermediate cells (low mean temperature) and eventually lowers the efficiency of the stack.

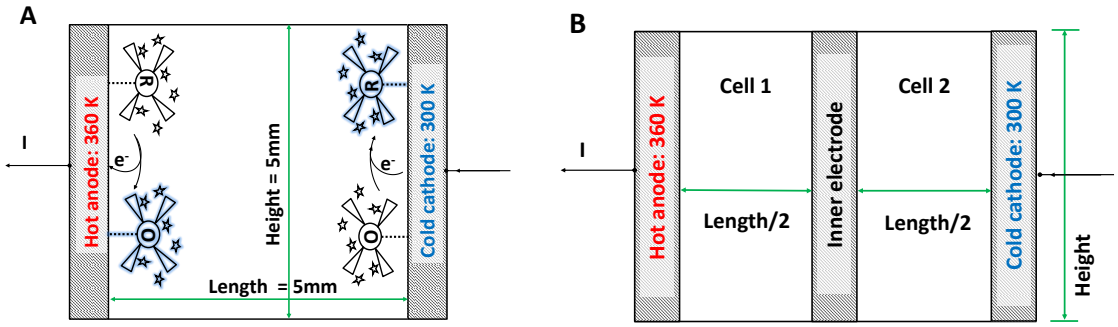

Fig. 3.4 A: schematic representation of stagnant TEC in a single cell configuration. B: example of a series stacking TEC with 2 internal cells. The height, total length, temperature of leftmost hot anode and rightmost cold cathode are kept same. In a N-series configuration, the single cell is split into N inner cells of equal size. Other parameters remain same as in **Table 3.1**.

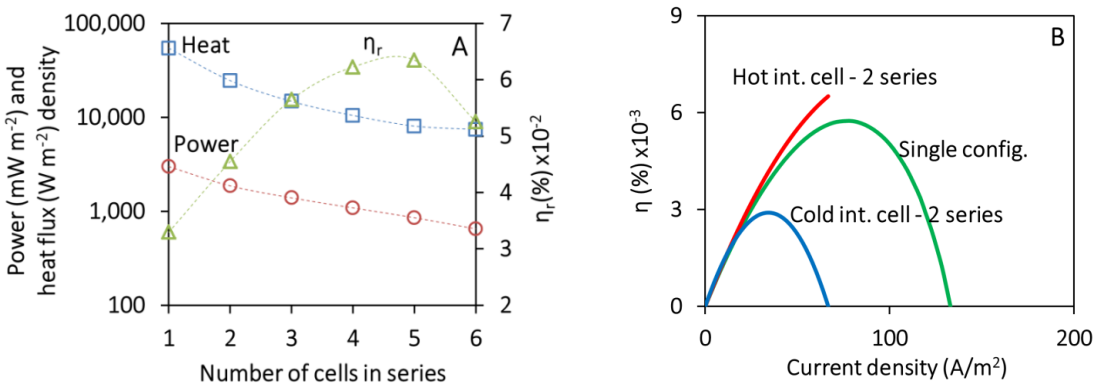

Fig. 3.5 Series stacking analysis. A: relative efficiency, power and input heat flux density in a N-series configuration. Number of cells equal to 1 refers to the single configuration (**Fig. 3.4A**). B: Efficiency breakdown of a 2-series and single configuration.

3.6 Flow thermo-electrochemical cell

Implementation of TECs in established flows and thermal gradients, like heat exchangers, can result in extra power production that would otherwise be lost. A forced convection or flow-TEC design is shown in **Fig. 3.6**, where a cold and hot equimolar redox electrolyte flows enter the TEC at a flow rates U_C and U_H, respectively. A no-slip velocity boundary condition is applied at the electrodes and the separator walls. The outside walls of the electrodes are insulated. The loss of thermal energy from the chemical reactions and from friction through the walls is assumed to be negligible. A uniform cold and hot temperature in the cathode and anode compartments is maintained, respectively. The temperature difference between the electrodes generates a cell voltage proportional to the redox reaction entropy. In a closed circuit, ionic flux, and oxidation and reduction at the electrodes maintains the electric current through the load. Natural convection due to concentration and temperature gradients is neglected because each

compartment (cold and hot) remains almost isothermal. Aqueous potassium ferri/ferrocyanide is used as electrolyte; thus, the Soret and Dufour effects are negligible. Also, the ionic molar resistivity of the membrane has been omitted.

As shown in **Fig. 3.7**, the majority of the potential drop in the flow TEC modeled here is due to the electrolyte resistivity. Consequently, current density changes linearly with cell voltage, which means the current has a strictly ohmic nature. Transient currents due to ionic diffusion in the boundary layer vanish rapidly, as reported previously [14]. These results considered along with the dependence of the power on cell length as shown in **Fig. 3.3** suggest that a fundamental limit exists on the ability to scale TECs, as any form of convection would not improve the performance past a point.

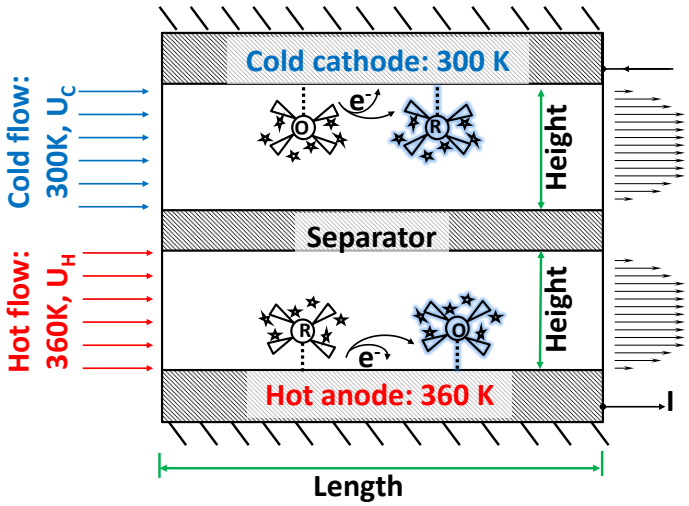

Fig. 3.6 Schematic representation of a flow TEC. Hot and cold compartments are assumed to have a uniform temperature of 360 and 300 K, respectively. Compartment height is 5 mm, and length is 10 mm. Hot and cold inlet equimolar concentration equals 400 mol m^{-3}. Hot and cold flow rate is 0.1 m s^{-1}. Refer to **Table 3.1** for the remaining parameters.

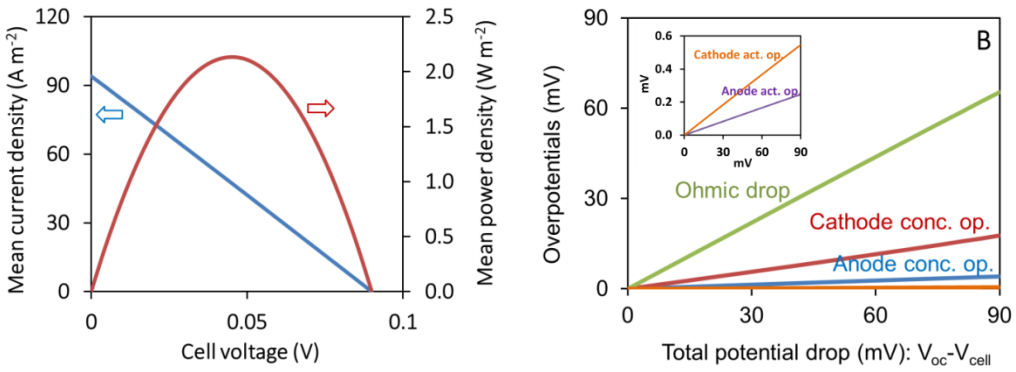

Fig. 3.7 Performance of a flow TEC at 0.1 m s^{-1} inlet electrolyte flow rate. Cell dimensions as described in **Fig. 3.6**. A: average current and power density vs cell voltage. B: breakdown of the overpotential components (ohmic drop, concentration and activation overpotentials).

In summary, this study shows that natural convection can significantly increase the conversion efficiency of thermocells with conventional aqueous electrolyte (0.4M potassium ferri/ferrocyanide), by compressing the diffusive boundary layers. The simulations also show that series stacking of TEC can potentially increase the conversion efficiency by 100% compared to a single cell configuration. The results also show that in a flow thermocell design, the power is limited by the ohmic resistances of the electrolyte.

CHAPTER 4. DOPING OF CARBON NANOTUBE ELECTRODES AND THEIR EFFECT ON THERMO-ELECTROCHEMICAL CELL EFFICIENCY

4.1 Introduction

As mentioned in Section 2.2, the electrokinetics is also affected by the electrolyte concentration, solvent and counter ion. In potassium ferri/ferrocyanide, in particular, the kinetics is slower at higher concentrations, thus limiting the power in TECs. In this chapter, nitrogen-doped MWCNT (NCNT) and boron-doped MWCNT (BCNT) electrodes are investigated in order to improve the catalytic activity of MWCNT electrodes with potassium ferri/ferrocyanide, and to potentially improve the energy conversion efficiency of MWCNT-based TECs. The kinetic and surface area changes due to plasma doping of MWCNT buckypaper (purchased from Nanocomp Inc.)electrodes are characterized using cyclic voltammetry and impedance spectroscopy. These electrodes are then tested with potassium ferri/ferrocyanide electrolyte in a U-shape glass TEC.

4.2 Methods

4.2.1 Electrode preparation and doping

MWCNT buckypaper was purchased from Nanocomp, Inc. The buckypaper is approximately 35 μm thick, with MWCNT lengths ~ 100 μm and diameters approximately 10 nm (**Fig 4.1A**). The typical synthesis of the buckypaper consists first on a dispersion of MWCNTs in an aqueous solution and surfactants. The MWCNTs are then filtered and compressed until forming an uniform film. The doping element content

in the MWCNTs was controlled to approximately 5% with respect to carbon using a plasma-enhanced chemical vapor deposition (PECVD) process. Nitrogen doping of buckypaper samples was obtained after 5 minutes exposure to 350W RF plasma (13.56 MHz) and 250 sccm of nitrogen (N_2) mixed with 20 sccm of ammonia (NH_3); the process chamber was at 200 mTorr and 350 ^oC. Boron doping followed a similar process with a mixture of silane (SiH_4) and diborane gas (B_2H_6) at 300 mTorr replacing N_2 and NH_3 in the process chamber. **Fig 4.1B** shows X-ray photoelectron spectroscopy (XPS) data for NCNT and BCNT electrodes with peaks at the corresponding energy level of the dopant element (195 eV for boron and 400 eV for nitrogen). The doped CNT were kept in a vacuum storage until spectroscopy and/or thermocell testing. Upon thermocell testing, the samples were washed with water and tested again. Feng et al. [84] showed that nitrogen doping of carbon nanotubes by PECVD maintain the same stability as platinum/carbon electrodes towards the reduction of oxygen in microbial fuel cells. Feng et al. showed that, over 25 cycles and 50 days, nitrogen-doped CNT improved the power density and stability when compared was to platinum supported on carbon electrodes. Platinum (Pt) electrodes were fabricated for comparison with MWCNT electrodes by sputtering a 50/150 nm bilayer of Ti/Pt on a stainless steel substrate. The geometric surface area of all electrodes was held constant at 0.178 cm^2. In this chapter, MWCNT are also referred to as CNT.

4.2.2 Characterization methods

Cyclic voltammetry (CV) and impedance spectroscopy (EIS) measurements were carried out using a CH660D potentiostat. Ohmic resistance compensation was applied to all CV runs. EIS data was taken at the equilibrium potential dc signal (with respect to

Ag/AgCl reference electrode) and 5 mV amplitude ac signal. The electrolyte solution was potassium ferrocyanide and potassium ferricyanide (Sigma-Aldrich) dissolved in distilled water ($K_3Fe(CN)_6/K_4Fe(CN)_6$). Both measurements, EIS and CV, were performed several times after immersion of the electrodes in the electrolyte solution, and the final measurements reported do not change significantly with time. EIS and CV runs were performed at 20 °C.

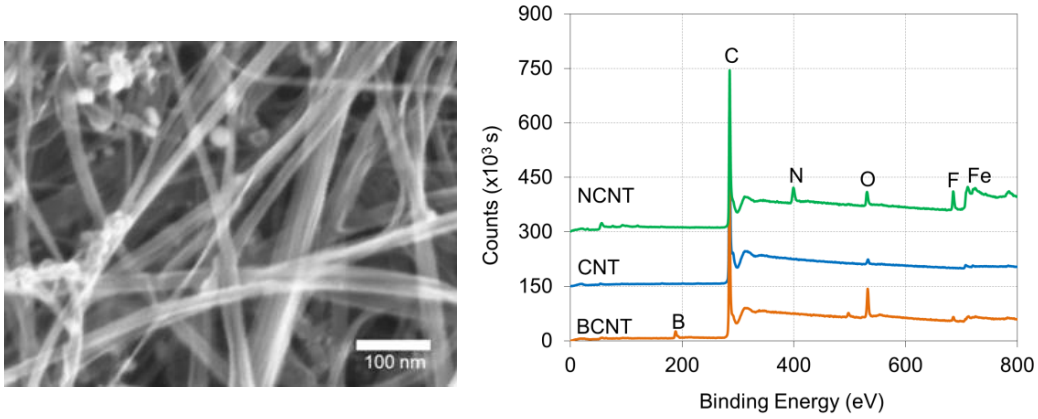

Fig. 4.1 A) Scanning electron microscope (SEM) micrograph of MWNT buckypaper purchased from Nanocomp Inc. B) X-ray photospectroscopy (XPS) of buckypaper before and after nitrogen and boron doping.

4.3 Results: electrochemical characterization

In EIS, the diameter of the semicircle in the frequency range of kinetic control determines the charge transfer resistance according to the Randles model [85]. The charge transfer resistances of Pt and CNT electrodes were estimated to be 23 Ω and 92 Ω, respectively, based on their EIS responses in 0.01 M of ferri/ferrocyanide solution (**Fig. 4.2**). The diffusion and kinetic controlled EIS responses superpose for doped CNT electrodes because of their large capacitances; therefore, it is difficult to estimate charge

transfer resistance using EIS. The ohmic resistances due to the electrodes, solution, and interfaces were determined by extrapolating measurements at high frequencies (left side of curve) using the Randles model. As expected, injection of electrons (NCNT) and holes (BCNT) increase and decrease the electronic conductivity of MWCNT electrodes, respectively.

Electrodes of NCNTs, pristine CNTs, and Pt produce a separation of about 60 mV between peak potentials in 0.01M of potassium ferri/ferrocyanide at a CV scan rate of 10 mV/s and 20 °C (**Fig. 4.3**); this corresponds to a reversible electrochemical reaction. In contrast, BCNT electrodes produce a peak separation of 250 mV, which indicates sluggish charge transfer (i.e., quasi-reversible kinetics).

In reversible electron transfer kinetics, the reduction and oxidation at the surface is fast enough to maintain dynamic equilibrium of the anodic and cathodic current at any voltage. The maximum or peak current occurs when the current increases until one of the ions is depleted, and diffusion subsequently limits the electrolyte concentration at the surface. The peak current at the electrode is independent of the exchange current density constant (i.e., the dynamic equilibrium current at zero voltage) as well as the potential where the peak current occurs. The faradaic peak current (I_f^p) varies proportionally to the diffusion coefficient (D), initial concentration (C^o), scan rate (v), and electroactive surface area (A) as described in [58]

$$I_f^p \propto D^{0.5} v^{0.5} C^o A \qquad \text{eq. 35}$$

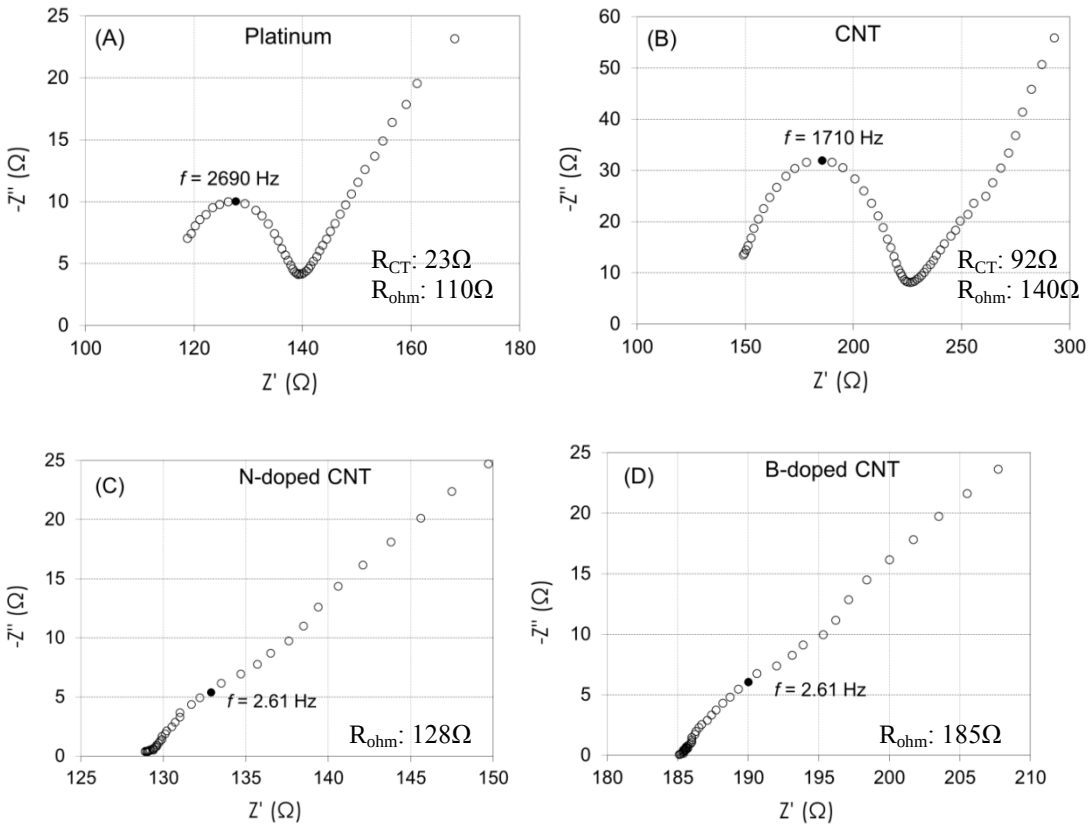

Fig. 4.2 Electrochemical impedance spectroscopy (EIS) at 190 mV dc signal, 5 mV ac signal, and 0.01M equimolar solution of $K_3Fe(CN)_6/K_4Fe(CN)_6$. R_{CT}: charge transfer resistance. R_{ohm}: ohmic resistance.

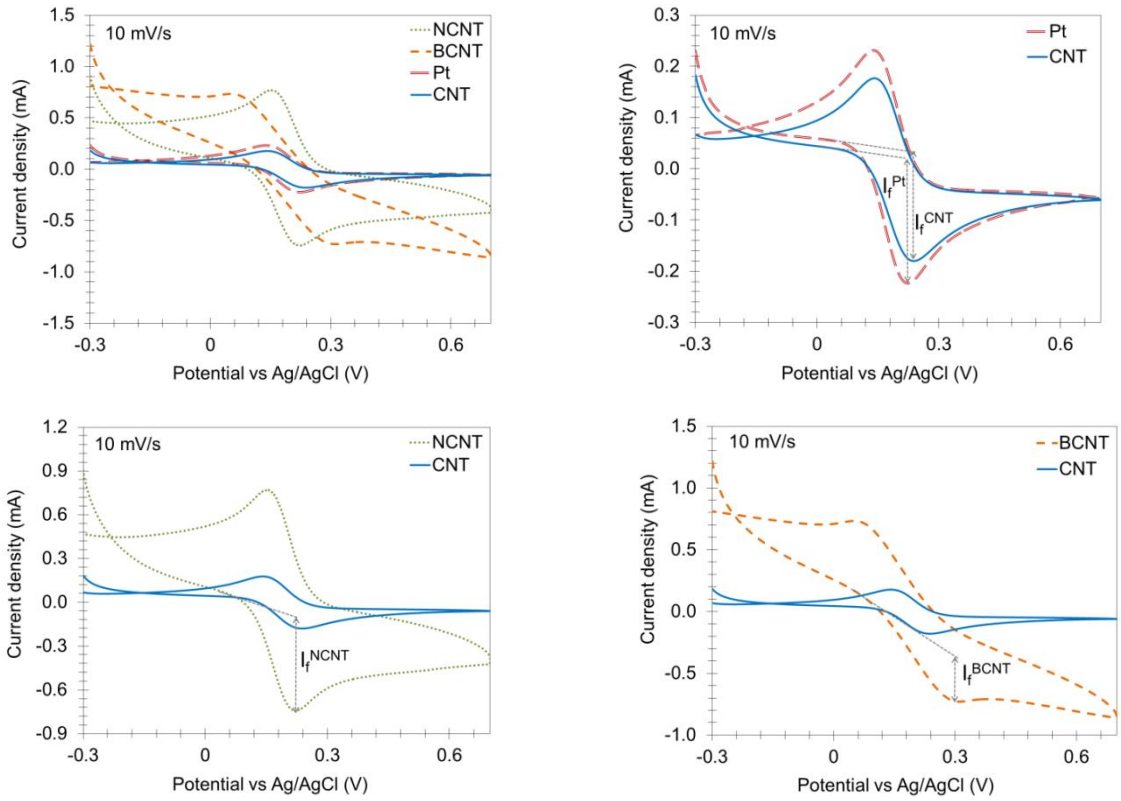

Fig. 4.3 Cyclic voltammetry of 0.01M equimolar solution of $K_3Fe(CN)_6/K_4Fe(CN)_6$ at 10 mV/s and 20 °C. Voltage scan starts at -0.3 V (with respect to a Ag/AgCl reference electrode). IR compensation was applied before every run. Geometric surface area is 0.178 cm^2.

Cyclic voltammetry experiments on all of the electrodes indicate purely capacitive current from -0.3 (V_i) to 0 V (V_f). The average capacitance (γ) can be estimated by integrating the current within this voltage window as described in

$$\gamma = \frac{1}{\nu(V_f - V_i)} \int_{V_i}^{V_f} I(V)\,dV \qquad \text{eq. 36}$$

The specific capacitances of NCNT and BCNT electrodes (with respect to the geometric surface area) are 180 mF/cm^2 and 316 mF/cm^2, respectively (**Fig. 4.3**); the capacitance of pristine CNT electrodes is 42 mF/cm^2 at the same concentration and scan

rate. Because NCNT and CNT electrodes both have reversible kinetics, the increase in the peak faradaic current for NCNT (0.71 mA compared to 0.23 mA for CNT) can only result from a change in the effective electroactive surface area (according to **eq. 35**). This hypothesis is supported by the similar 3- to 4-fold increase in capacitance and faradaic current of NCNT with respect to pristine CNT electrodes. The peak faradaic current of BCNT electrodes (0.36 mA) is greater than that of CNT electrodes because of the increase in surface area; however it is diminished due to increased irreversibility in the charge transfer kinetics. We attribute the increase in surface area of doped electrodes to structural changes that result from the breaking of C-C bonds and dopant substitution during the PECVD doping process.

The voltage sweep rate in the CV test is faster than the reaction of ions at the surface in case where scan rate is 100 mV/s and the solution is 0.01M ferri/ferrocyanide (**Fig. 4.4A** and **Fig. 4.4B**). The anodic and cathodic currents are not in equilibrium under these conditions. Consequently, the peak current and separation of peak potentials depends on the electrochemical kinetics (i.e., quasi-reversible kinetics). The kinetics can be analyzed qualitatively using the separation of the potential peaks, where slow kinetics will need more voltage or more time to reach the peak current, or to reach the current at which depletion of ions at the surface commences. **Fig. 4.4B** shows that the separation between peak potentials is 40 mV smaller for NCNT electrodes than it is for CNT electrodes. This shows that nitrogen doping improves the kinetics of CNT electrodes. Boron doped CNT electrodes show much slower kinetics than both NCNT and CNT electrodes, which is consistent with results from scans at 10 mV/s. A possible explanation of the changes in electrode kinetics with doping is associated with electrostatic effects at

the electrode-electrolyte interface, which alter the electrochemical double layer as well as interacting with the counterions. Although still unclear, the effect of non-covalent interactions between ions and the electrode has been shown to be important in the kinetics [86]. According to the Gouy-Chapman-Stern model [87], electrostatic forces near the electrode cause an exponential distribution of the ion concentration as described by

$$c_i^s = c_i^o \exp\left(-\frac{z_i \phi F}{RT}\right) \qquad \text{eq. 37}$$

The charge of the ion and its concentration at the surface and in the bulk are represented by z_i, c_i^s and c_i^o, respectively. φ is the potential at the surface of the electrode with respect to the potential at the bulk. According to **eq. 37**, a negatively charged doped electrode (NCNT) strengthens the electrostatic interaction with potassium (K+) counter ions and increases the electrolyte concentration at the surface of the electrode; the net current increases as a result. Similarly, a positively charged doped electrode will repulse the K+ (lower φ) and reduce the net current.

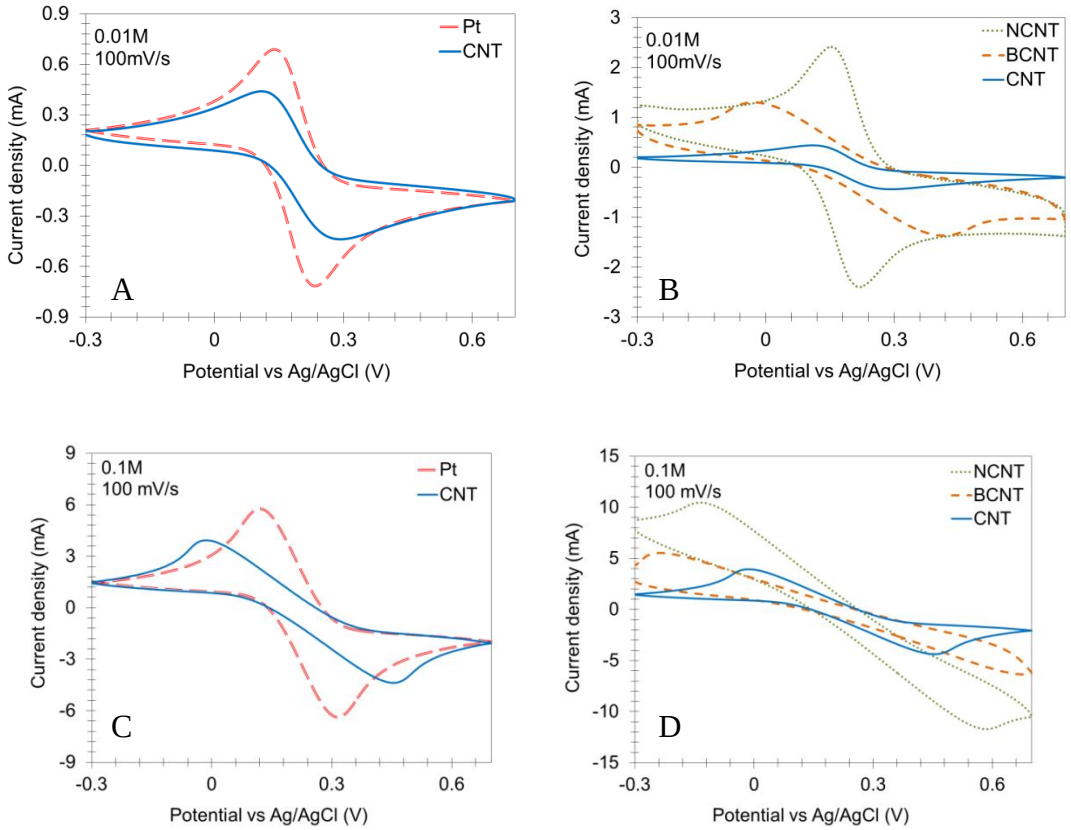

Fig. 4.4 Cyclic voltammetry of 0.01M (A and B) and 0.1M (C and D) equimolar solution of $K_3Fe(CN)_6/K_4Fe(CN)_6$ at 100 mV/s and 20^oC. Voltage scan starts at -0.3 V (with respect to a Ag/AgCl reference electrode). IR compensation was applied before every run. Geometric surface area is 0.178 cm^2.

Because anodic and cathodic peak currents are a function of the exchange current density constant in quasi-reversible reactions [88], they are also a function of the charge transfer coefficient. The transfer coefficient can be understood as the ratio of the effective potential of the electric double layer used to raise the chemical potential of the reactants and lower the activation energy. Therefore, the transfer coefficients towards oxidation and reduction may be different, but they are complementary (the sum of the coefficients is equal to 1). The doping seems to alter the Fermi energy of the electrodes – and

therefore it alters the energy gap with respect to the electrolyte, as indicated by the change in electrode resistance with doping shown in **Fig. 4.2**. However, **Fig. 4.4** shows that the cathodic and anodic currents are symmetric for all electrodes in this study, which suggests that the charge transfer coefficient is close to 0.5 with NCNT and BCNT electrodes in potassium ferri/ferrocyanide electrolyte.

A symmetric transfer coefficient of one half means an equal interaction of the oxidized and reduced metal ions with the electrode. Since the electronic coupling changes of reactants and electrodes due to doping of the electrodes did not alter the transfer coefficients, the reaction can be considered as adiabatic Therefore any change in the rate constant should be a consequence of nuclei collision frequency factor changes, and activation energies associated with them only.

Cyclic voltammetry scans at 100 mV/s were also performed at a higher electrolyte concentration of 0.1M potassium ferri/ferrocyanide (**Fig. 4.4C** and **Fig. 4.4D**) because such high concentrations are required for practical TECs. The separation of potential peaks for Pt, CNT and BCNT electrodes shows slower kinetics for BCNTs than for CNTs, and slower kinetics for CNTs than for Pt. These trends are similar to the trends observed at lower concentrations. However, in contrast to results at low electrolyte concentration, NCNT electrodes show slower kinetics than CNT and Pt electrodes at the higher concentration. In this case, high bulk concentrations decrease the thickness of the electrochemical double layer [87] on the order of $[10^7|z_i|(c_i^o)^{0.5}]^{-1}$; this adds to the compression of the double layer that already exists due to the negatively charged doped electrode (NCNT). The high density of electrolyte at the surface increases the nuclei

reorganization energy of the electron transfer process by blocking the path of the atoms towards the oxidized or reduced state, thus slowing down the kinetics.

4.4 Thermo-electrochemical performance

The energy conversion efficiency of a TEC is approximated to

$$\eta = \frac{V_{oc} I_{sc}}{4A\kappa\Delta T/d} \qquad \text{eq. 38}$$

where V_{oc} is the open circuit voltage, I_{sc} the short circuit current, A the geometric surface area, κ the thermal conductivity of the electrolyte, ΔT the temperature difference and d the electrodes' distance. Here, I measured V_{oc} and I_{sc} for Pt, CNT, and doped CNT electrodes in the same U-cell configuration; the results are presented in **Fig. 4.5**. The open circuit potential is driven by a thermal gradient (as described in **eq. 7**), and the ratio $V_{oc}/\Delta T$ is approximately 1.5 mV/K for all electrodes (see **Fig. 4.5A**). The short-circuit currents, I_{sc}, at steady state correlate with trends in the charge transfer kinetics shown in the CV scans of **Fig. 4.4** (these scans were performed in the same electrolyte concentration used for TEC tests). Ohmic compensation was applied to the measurement of I_{sc}. As shown in equation 22,

$$V_T = V_{oc} - \xi_a - \xi_c - \Delta\phi^s \qquad \text{eq. 22}$$

the total cell voltage, V_T, depends on the open circuit voltage, V_{oc}, minus the overpotentials, ξ, and ohmic drop, $\Delta\phi^s$, in the electrolyte. By applying an ohmic compensation in a short circuit measurement, all of the open circuit voltage created by the thermal gradients is consumed by the overpotentials at the electrodes only. The ohmic compensation allows studying the effect of the doped electrodes in the kinetics and power

of TECs. In the results in **Fig. 4.5B**, the ohmic resistance of the electrolyte represented 50 to 60 % of the total cell resistance, J_{sc}/V_{oc}.

The lower I_{sc} for NCNT and BCNT electrodes, compared to that of CNT and Pt electrodes, (**Fig. 4.5B**) reflects their relatively sluggish charge transfer kinetics as discussed above. The performance of asymmetric doped electrode configurations is also shown in **Fig. 4.5**, i.e., NCNT as the cold electrode and BCNT as the hot electrode, and vice versa. While both asymmetric arrangements produce higher initial currents than symmetric doped electrode configurations, the current in the asymmetric arrangements eventually decreases as the magnitude of the thermal gradient is increased. The combination of BCNT and NCNT electrodes at small thermal gradients drives large concentration gradients at the surface of the BCNT electrode, due to its slow kinetics, while establishing low surface concentrations at the NCNT electrode, which avoids the blocking state discussed in the previous section. At larger thermal gradients, the ion concentration at the surface of the NCNT electrodes increases to the point where the high rate of collision of atoms slows the kinetics and leads to reduced currents. The transition to slower kinetics occurs at smaller thermal gradients when the NCNT electrode is the cold electrode, as opposed to the hot electrode, because higher ion concentrations exist at the cold electrode due to the slow kinetics at low temperatures. The NCNT symmetric configuration shows lower currents than any of the asymmetric cases, because the blocking state is reached at the hot and cold electrodes due to their similar rate constant.

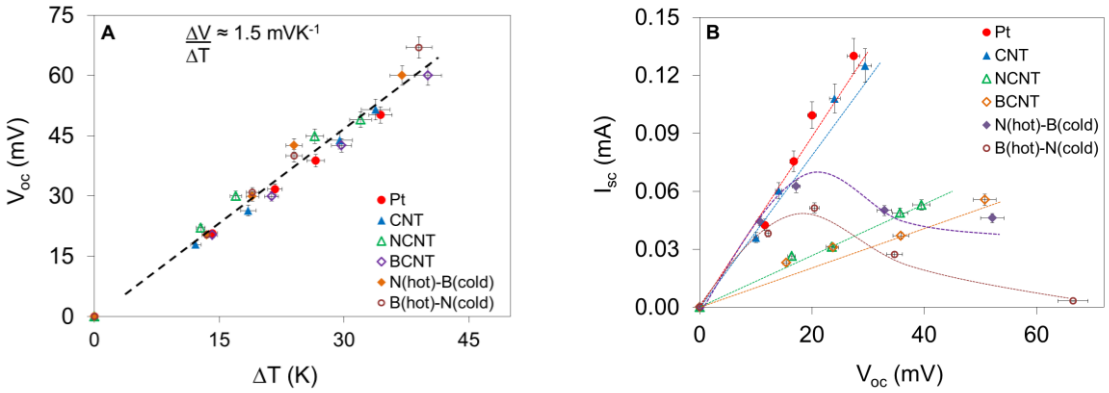

Fig. 4.5 TEC response in 0.1M of $K_3Fe(CN)_6/K_4Fe(CN)_6$. A: Open-circuit potential (V_{oc}) and B: short-circuit current (I_{sc}). Temperature at the cold electrode was maintained at 20 °C. Geometric surface area is 0.178 cm^2. Ohmic resistance compensation was applied to the short circuit current reported. The same electrode type was used as the anode and cathode unless otherwise stated in the legend.

In summary, CV measurements revealed a reversible (i.e., diffusion controlled) electrochemical reaction at NCNT electrodes at low electrolyte concentrations and a more irreversible reaction at high concentrations, suggesting slower kinetics at higher electrolyte concentrations. In contrast, slow kinetics was observed for BCNT electrodes at both low and high electrolyte concentrations. CV results for both NCNT and BCNT electrodes suggest that plasma exposure during the doping process increased the electrochemically active surface area. Electrostatic interactions with potassium ions, and electron density changes at the CNT surface altered the charge transfer kinetics; yet, the symmetry of the charge transfer remained approximately equal to that of pristine CNTs. In TEC tests, accumulation of potassium ions at doped CNT electrodes was found to reduce the short-circuit current.

CHAPTER 5. STUDY OF NOVEL ELECTROLYTES: IONIC LIQUIDS INTEGRATED WITH CARBON NANOTUBES

5.1 Introduction

Compared to aqueous solutions, ionic liquids (ILs) solvent can extend the temperature range of operation of TECs, because of their high boiling temperatures (> 150 °C) [24,26]. In addition, ILs have higher ohmic conductivities than conventional non-aqueous electrolytes. Recent reports have shown that the addition of CNTs to IL electrolytes can improve the efficiency of DSC, although the transport mechanisms and their molecular interactions have not yet fully explained [89,35]. In this chapter, I use nuclear magnetic resonance (NMR) spectroscopy to reveal the molecular interactions between the MWCNTs and ILs, which provides evidence to support the high dispersibility of CNTs in ILs. These mixtures are also studied with electrochemical impedance spectroscopy (EIS) to quantify the ionic and electronic contributions in the total electrical conductivity of 1-methyl-3-propylimidazolium iodide ([PMIM][I]), 1-butyl-3-methylimidazolium hexafluorophosphate ([BMIM][PF_6]), and 1-butyl-3-methylimidazolium hydrogen sulfate ([BMIM][HSO_4]) mixed with MWCNTs or nitrogen-doped MWCNTs (N-MWCNTs) below and above the wt% required for percolation. These results are compared to mixtures of MWCNTs in the organic solvents DMF and dimethyl sulfoxide (DMSO). EIS and NMR results show that CNT-ILs have enhanced conductivity, which provides an alternative explanation for the recent reports of enhanced energy conversion efficiency in devices that use CNT-IL electrolytes [32-35].

5.2 Methods

[BMIM][PF_6], [BMIM][HSO_4], and [PMIM][I] (purity >99%) were purchased from IOLITEC; DMF and DMSO from Sigma Aldrich; and MWCNTs and N-MWCNTs from US-nano (US4315 and US4882, respectively). According to product specifications, the MWCNTs had a length of 10-20 μm, outside diameter of 50-80 nm, and density of 2.1g/cm^3. The N-MWCNTs had an approximate length of 35 μm and outside diameter of 20-50 nm and about 3 wt% of nitrogen content. The solvents, ILs, and CNTs were used as received.

I stirred each mixture of MWCNT-IL on a hot plate for 30 minutes, then ultrasonicated the mixture for 30 minutes, followed by another stirring step for 15 minutes, with all steps occurring at a temperature of 65 °C. The samples were allowed to cool at room temperature for at least 1 hour, followed by 5 minutes of stirring before taking measurements. Typical sample volumes were approximately 6 mL. To increase the wt% of MWCNTs in the ILs, I added MWCNTs to the mixture subsequent to the previous test at lower wt%, and repeated the stirring and sonication steps described above. Coulometric Karl Fischer titration (Titroline KF, Schott instruments) indicates water content less than 0.05 wt%, before and after the mixing in the ionic liquids (**Table 5.1**). Previous studies on the effect of water impurity showed a change of less than 4% in the electrical conductivity of imidazolium-based ionic liquids when the water content is below 0.1 wt% [90,91]. The electrochemical setup consisted of a 2-electrode configuration with platinum electrodes. The conversion of the measured impedance to conductivity was calibrated using standard solutions of potassium chloride at 0.01 M and 0.1 M, following **eq. 28 and 29** in **Section 2.3**. EIS was performed with a CH

instruments Model 660E potensiostat. The ac voltage amplitude was 20 mV and the dc signal was 0 mV. The spectra ranged from 1 MHz to 0.02 Hz for all the solvents and ILs, except for [PMIM][I]. We extended the lowest frequency in [PMIM][I] to 0.002 Hz, in order to reach the region where diffusion is dominant. The spectra were fit to impedance circuit models using the automated software provided by CH instruments.

Table 5.1 Water content (wt%) in [BMIM][PF_6], [BMIM][HSO_4] and [PMIM][I], before and after the mixing procedure.

	Before	After
[BMIM][PF_6]	0.033	0.011
[BMIM][HSO_4]	0.021	0.017
[PMIM][I]	0.01	0.017

I performed ^{1}H-1D and ^{1}H-PSGE diffusion NMR spectroscopy of neat MWCNT-ILs in NMR tubes 5 mm in diameter at 23 °C, and in a Bruker AV3-400 NMR spectrometer (magnetic field strength of 9.4 T). The instrument was equipped with a Bruker Diff50 diffusion probe and gradient amplifiers allowing pulsed field gradient (PFG) experiments with magnetic field gradients larger than 2000 G/cm. The chemical shift scale was calibrated using an external standard of 0.1% DSS (3-Trimethylsilylpropane sulfonic acid and chemical shift calibrated to 0 ppm) in D_2O containing 20% H_2O. The diffusion coefficients were measured using the PFG stimulated echo sequence (PFG-STE). Spectra were measured as a function of the gradient strength.

Integrals over individual peaks were fitted using the Bruker Topsin software according to the Stejskal-Tanner equation [77-79]:

$$\ln\left(\frac{I}{I_o}\right) = -(\gamma\delta)^2 G^2 \left(\Delta - \frac{\delta}{3}\right) D \qquad \text{eq. 39}$$

where I/I_o is the ratio of the intensities with and without the gradient pulses, γ is the gyromagnetic ratio, G is the gradient strength, Δ is the diffusion time, i.e. the delay between the midpoints of the gradients (50 ms), δ is the gradient duration (2 ms), and D is the diffusion coefficient. The gradient pulses, providing G up to 2000 G/cm, were used for each measurement. Experimental uncertainty is approximately ±4% for the NMR measurements and ±9% for the EIS measurements, based on repeating each experiment three times.

5.3 Results and discussion

5.3.1 Electrochemical impedance spectroscopy

The impedance spectra for pure solvents or ILs, with the exception of [PMIM][I], resemble that of a dielectric material (**Fig. 5.1**). As MWCNTs are added, the conductivity of the MWCNT-IL mixtures increases, and the spectra in **Fig. 5.1** shift upward. When enough MWCNTs are added to the ILs or solvents to produce a percolated state, the conductivity at low frequencies increases by several orders of magnitude, and the spectrum resembles that of a resistor (frequency independent).

We fit the spectra in **Fig. 5.1** to the Debye model [71,92] (**Fig. 5.2a**) when the MWCNT-IL mixtures are below their percolation threshold – except for the [PMIM][I] spectra, which requires a different model. In the Debye model, a dielectric material is represented by two sets of parallel resistors and capacitors connected in series (**Fig. 5.2a**).

The dielectric capacitance between the metal electrodes (C_b) is proportional to the permittivity of the solvent or electrolyte. When an electric field is applied, the ions migrate toward the electrodes, and ion pairs polarize and orient in the direction of the applied field. The mobility of the ions and dipoles, and the concentration of charges determines the bulk resistance, R_b. The accumulation of charges at the electrode interface with the electrolyte or solvent is represented by the constant-phase element, Q_{dl}; this is a non-ideal capacitor with a phase between 0 and 90° that accounts for the surface roughness of the electrode and other inhomogeneous properties at the double layer [93,94]. The contact resistance at this interface is R_c.

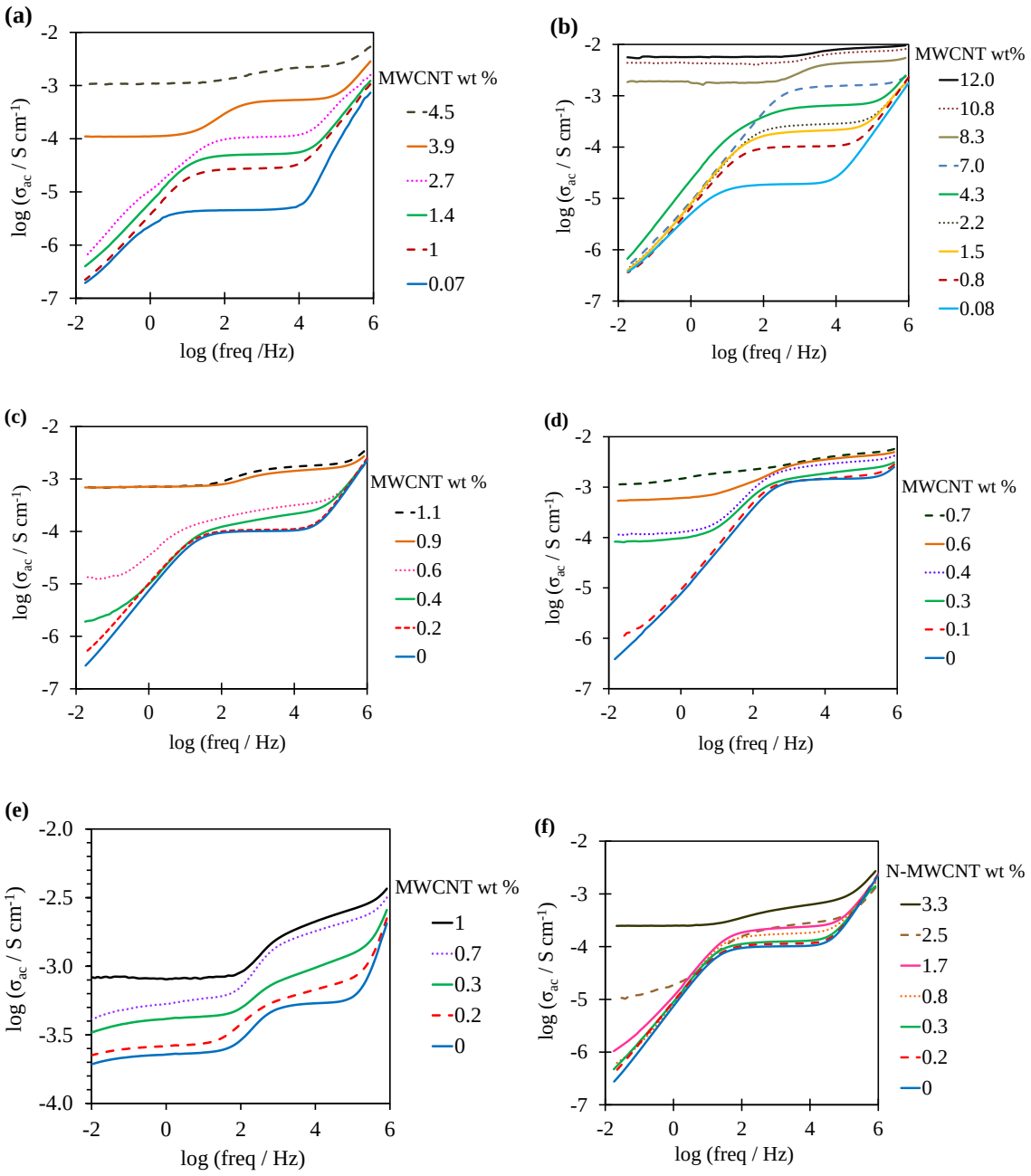

Fig. 5.1 Frequency dependence of ac conductivity, σ_{ac}, for MWCNT powders mixed in DMF (a), DMSO (b), [BMIM][HSO_4] (c), [BMIM][PF_6] (d), [PMIM][I] (e) and [BMIM][HSO_4] mixed with N-MWCNTs (f). The measured impedance spectra are converted to conductivity using **eq. 28 and 29** in **Section 2.3**.

The two parallel RC brackets connected in series in the model of **Fig. 5.2a** have different time constants. C_b in parallel with R_b determines the impedance (Z_{HF}) in the high frequency region (>10^4 Hz) as

$$Z_{\mathrm{HF}} = \frac{R_{\mathrm{b}}}{1+j\omega C_{\mathrm{b}} R_{\mathrm{b}}} \qquad \text{eq. 40}$$

where ω is the frequency. Whereas, R_c in parallel with Q_{dl} determines the impedance (Z_{LF}) in the low frequency region (<100 Hz) as

$$Z_{\mathrm{LF}} = \frac{R_{\mathrm{c}}}{1+(j\omega)^{\alpha} Q_{\mathrm{dl}} R_c} \qquad \text{eq. 41}$$

where α is the constant-phase element coefficient (between 0 and 1) due to the inhomogeneity of the electrode. The bulk resistance (R_b) determines the frequency independent conductivity in the mid-frequency region of the spectra (between 10^2 and 10^4 Hz).

When the MWCNT-IL mixtures are near and above their percolation threshold, the spectra were fit to the model in **Fig. 5.2b** to account for the grain boundaries between the MWCNTs and IL [95,96]. The resistance and capacitance at these grain boundaries are represented by R_{gb} and Q_{gb}, respectively. The spectra for the redox IL [PMIM][I] were fit to the model in **Fig. 5.2c** [71]. The charge transfer resistance, R_{ct}, is due to the activation polarizations of the electrochemical reactions of iodide. The Warburg impedance, W, is the mass transfer impedance due to diffusion near the electrode.

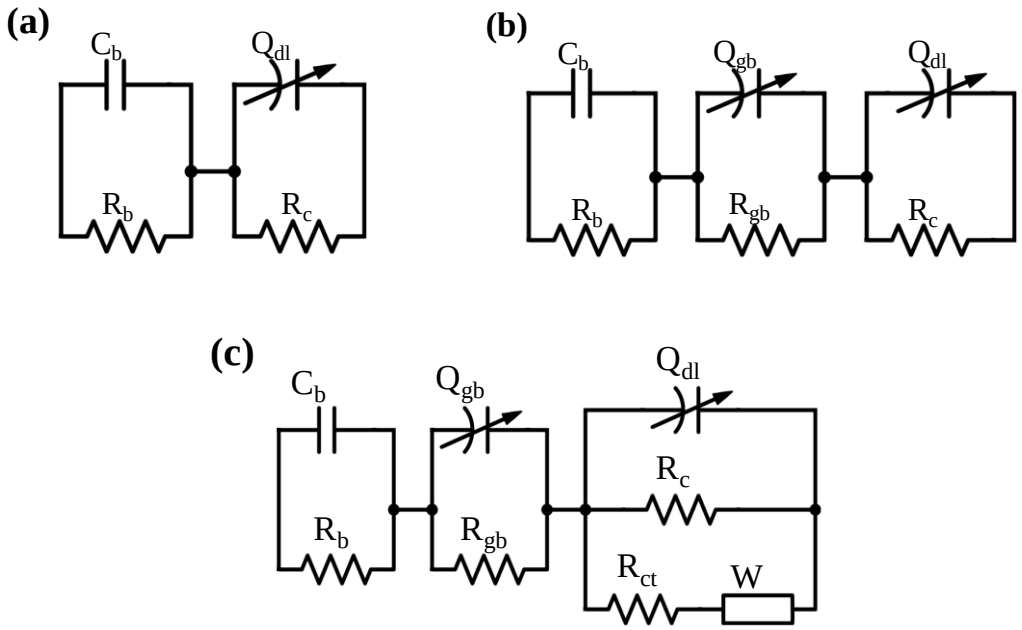

Fig. 5.2 Models used to fit the EIS of MWCNT-ILs. a) Model for a dielectric material. b) Model for a dielectric material with suspended particles forming grain boundaries. d) Model for a redox electrolyte with suspended particles. C_b is the bulk capacitance; R_b is the bulk resistance; Q_{dl} is the double layer capacitance; R_c is the contact resistance; Q_{gb} is the grain boundary capacitance; R_{gb} is the grain boundary resistance; R_{ct} is the charge transfer resistance; and W is the Warburg impedance.

Fig. 5.3 shows the changes in R_b and R_c as MWCNTs are added. The fitted parameters are presented in **Table 5.2** to **Table 5.7**. **Fig. 5.1** shows that the percolated state in DMF and DMSO is reached around 3 wt% and 8 wt% of MWCNTs, respectively. These percolation thresholds correlate with their dispersion limits of 2.3×10^{-3} wt% and 5.4×10^{-4} wt%, respectively [97]. A low dispersion limit means an aggregation of the MWCNTs at low wt%, decreasing the aspect ratio of the particles, resulting in a high

percolation threshold [98]. In the MWCNT-ILs mixtures (**Fig. 5.1c-e**), the percolation state is reached below 1 wt%, suggesting a high affinity of the ILs to disperse the MWCNTs. The theoretical critical volume fraction at the percolation threshold for randomly oriented cylinders can be estimated as $W/2L$, where W and L are the diameter and length of the cylinders, respectively [98]. Based on the aspect ratio of the MWCNTs used, the theoretical volume fraction is between 0.002 and 0.006. The critical volume fraction found from our measurements of MWCNTs in ILs falls between 0.006 and 0.009, suggesting a high affinity of the ILs to disperse the MWCNTs.

Fig. 5.3 shows that before reaching the percolated state, the bulk resistance (R_b) of the MWCNT-IL mixtures drops by 3 to 5 fold; while the contact resistance (R_c) drops approximately 3 orders of magnitude, but still remains 1 to 2 orders of magnitude higer than R_b. At the percolated state, R_b and R_c are of the same order of magnitude, approximately 10^3 Ω. Without MWCNTs, R_b and R_c of the ILs depend mainly on their ionic diffusion at the bulk and diffusive boundary layer, respectively. But when MWCNTs are added, interfacial polarization and percolation decrease R_b and R_c [98-100,92]. As shown in **Fig. 5.4**, when an electric field is applied to a conductive particle in a medium, the particle is polarized. Then, the charges in the medium redistribute around the particle in accordance with Coulomb's law (i.e., Maxwell-Wagner polarization or interfacial polarization), increasing the dielectric losses. As the dipoles near the particle orient in the direction of the electric field, they absorb energy that otherwise would be stored in the dielectric. Following the electrical RC circuit in **Fig. 5.2a**, the energy required is E_{ac}/R, where E_{ac} is the ac electric field. This energy required is described as dielectric losses. As the MWCNTs are added to the solution, the ions become trapped at

the surface of the particles and require more energy to align in the direction of the electric field. Thus, as the dielectric loss increases, the ohmic resistance drops [96,101,99].

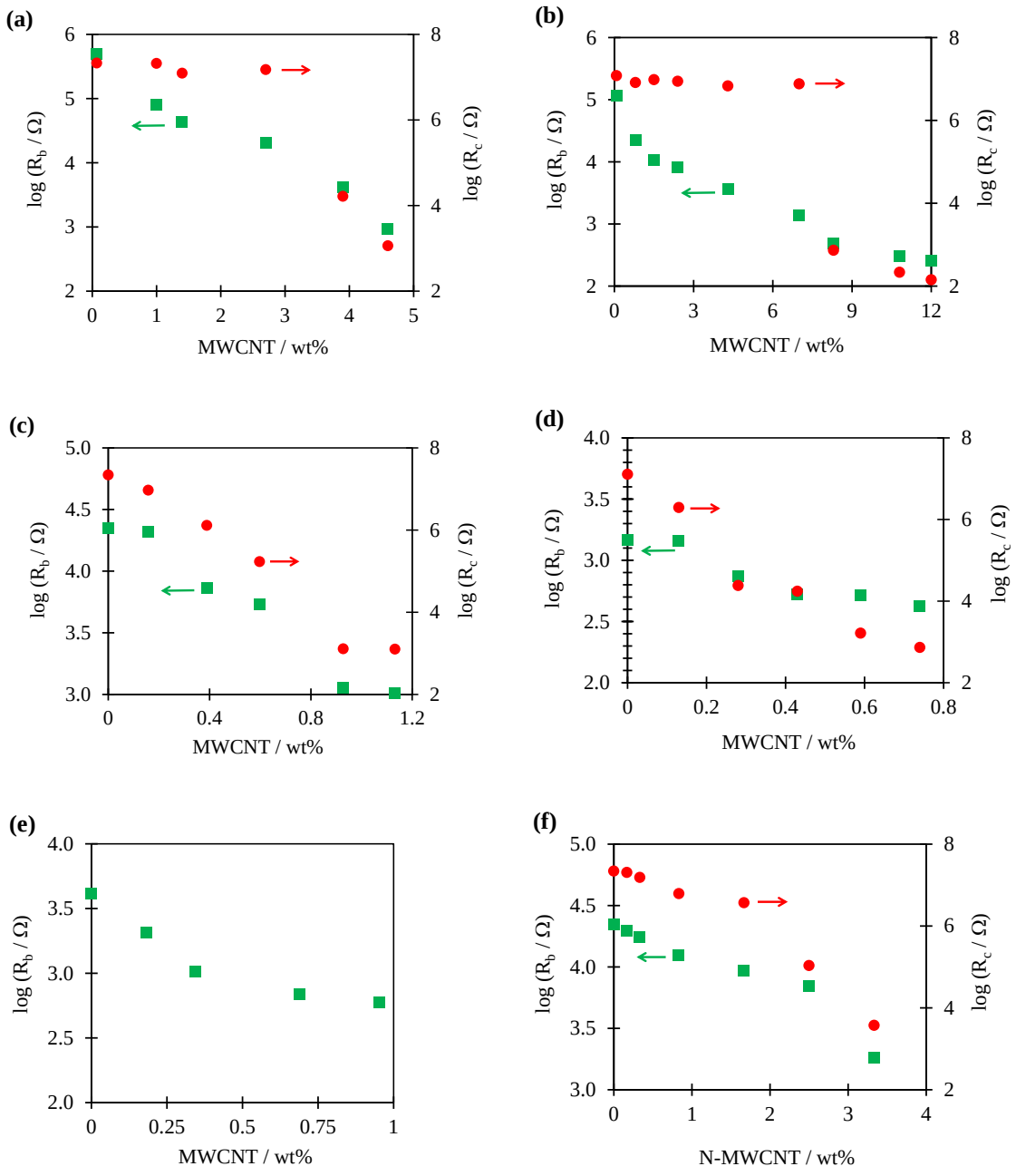

Fig. 5.3 Bulk, R_b (green squares), and contact , R_c (red circles), resistances, as MWCNTs are added in DMF (a), DMSO (b), [BMIM][HSO_4] (c), [BMIM][PF_6] (d), [PMIM][I] (e), and as N-MWCNTs are added to [BMIM][HSO_4] (f). The impedance spectra of **Fig. 5.1** were fit with the electrochemical models of **Fig. 5.2** to obtain the resistances.

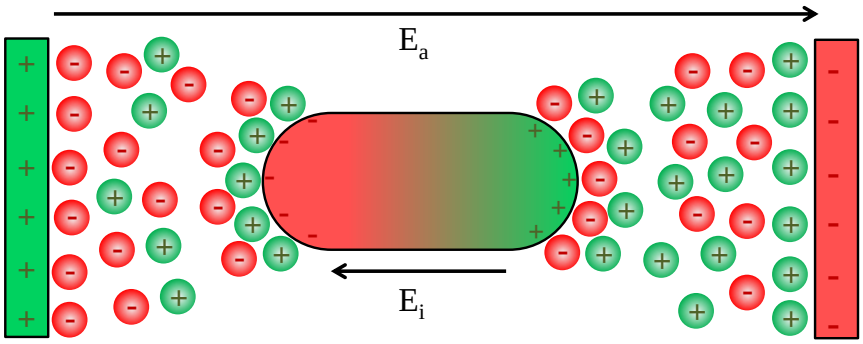

Fig. 5.4 Schematic representation of the interfacial polarization induced in a conductive particle (e.g., MWCNT) in an ionic medium. In addition to ionic diffusion of the positive (+) and negative (-) charges, the applied electric field (E_a) induces an internal electric field (E_i) from the electronic polarization in the particle and redistribution of the ions around the surface.

Table 5.2 Fitting parameters of the impedance spectra in MWCNT-DMF mixtures to the model in **Fig. 5.2a**. C_b is the bulk capacitance; R_b is the bulk resistance; Q_{dl} is the double layer capacitance; α_{dl} is the constant phase element coefficient for Q_{dl}; and R_c is the contact resistance.

MWCNT wt%	R_b (Ω)	R_c (Ω)	C_b ($\Omega^{-1}s$)	Q_{dl} ($\Omega^{-1}s^{\alpha dl}$)	α_{dl}
0.07	4.9×10^5	2.1×10^7	5.3×10^{-10}	3.6×10^{-7}	0.81
1	7.9×10^4	2.1×10^7	1.2×10^{-10}	4.2×10^{-7}	0.82
1.4	4.3×10^4	1.2×10^7	1.7×10^{-10}	5.4×10^{-7}	0.85
2.7	2.0×10^4	1.5×10^7	2.9×10^{-10}	1.5×10^{-6}	0.83
3.9	4.1×10^3	1.6×10^4	3.0×10^{-10}	9.5×10^{-7}	0.83
4.5	9.3×10^2	1.1×10^3	8.7×10^{-10}	1.2×10^{-5}	0.60

Table 5.3 Fitting parameters of the impedance spectra in MWCNT-DMSO mixtures to the model in **Fig. 5.2a**. C_b is the bulk capacitance; R_b is the bulk resistance; Q_{dl} is the double layer capacitance; α_{dl} is the constant phase element coefficient for Q_{dl}; and R_c is the contact resistance.

MWCNT wt%	R_b (Ω)	R_c (Ω)	C_b ($\Omega^{-1}s$)	Q_{dl} ($\Omega^{-1}s^{\alpha dl}$)	α_{dl}
0.08	1.2×10^5	1.2×10^7	1.3×10^{-10}	6.2×10^{-7}	0.77
0.8	2.2×10^4	8.2×10^6	1.9×10^{-10}	6.0×10^{-7}	0.88
1.5	1.1×10^4	9.6×10^6	2.1×10^{-10}	7.7×10^{-7}	0.86
2.4	8.0×10^3	8.8×10^6	2.1×10^{-10}	7.6×10^{-7}	0.85
4.3	3.6×10^3	6.8×10^6	2.7×10^{-10}	2.1×10^{-6}	0.85
7.0	1.4×10^3	7.6×10^6	2.2×10^{-10}	8.9×10^{-7}	0.86
8.3	4.9×10^2	7.3×10^2	7.4×10^{-10}	9.1×10^{-7}	0.88
10.8	3.1×10^2	2.2×10^2	1.4×10^{-9}	2.6×10^{-6}	0.80
12.0	2.5×10^2	1.4×10^2	1.1×10^{-9}	4.6×10^{-6}	0.80

Table 5.4 Fitting parameters of the impedance spectra in MWCNT-[BMIM][HSO_4] mixtures to the model in **Fig. 5.2b**, except at low concentrations of MWCNTs, at which grain boundaries effects were small. C_b is the bulk capacitance; R_b is the bulk resistance; Q_{dl} is the double layer capacitance; α_{dl} is the constant phase element coefficient for Q_{dl}; R_c is the contact resistance; Q_{gb} is the grain boundary capacitance; α_{gb} is constant phase element coefficient for Q_{gb}; and R_{gb} is the grain boundary resistance.

MWCNT wt%	R_b (Ω)	R_c (Ω)	C_b ($\Omega^{-1}s$)	Q_{dl} ($\Omega^{-1}s^{\alpha dl}$)	α_{dl}	R_{gb} (Ω)	Q_{gb} ($\Omega^{-1}s^{\alpha gb}$)	α_{gb}
0	2.2×10^4	2.2×10^7	2.0×10^{-10}	6.9×10^{-7}	0.86			
0.2	2.1×10^4	9.3×10^6	1.9×10^{-10}	1.0×10^{-6}	0.83			
0.4	7.2×10^3	1.3×10^6	2.9×10^{10}	1.1×10^{-6}	0.80	1.1×10^4	3.8×10^{-6}	0.37
0.6	5.3×10^3	1.7×10^5	2.2×10^{-10}	3.7×10^{-6}	0.86	1.5×10^4	8.2×10^{-6}	0.36
0.9	1.1×10^3	1.3×10^3	2.7×10^{-10}	1.6×10^{-6}	0.84	7.4×10^2	1.8×10^{-5}	0.37
1.1	1.0×10^3	1.3×10^3	2.7×10^{-10}	1.8×10^{-6}	0.84	8.0×10^2	6.4×10^{-5}	0.37

Table 5.5 Fitting parameters of the impedance spectra in MWCNT-[BMIM][PF_6] mixtures to the model in **Fig. 5.2b**, except at low concentrations of MWCNTs, at which grain boundaries effects were small. C_b is the bulk capacitance; R_b is the bulk resistance; Q_{dl} is the double layer capacitance; α_{dl} is the constant phase element coefficient for Q_{dl}; R_c is the contact resistance; Q_{gb} is the grain boundary capacitance; α_{gb} is constant phase element coefficient for Q_{gb}; and R_{gb} is the grain boundary resistance.

MWCNT wt%	R_b (Ω)	R_c (Ω)	C_b ($\Omega^{-1}s$)	Q_{dl} ($\Omega^{-1}s^{\alpha dl}$)	α_{dl}	R_{gb} (Ω)	Q_{gb} ($\Omega^{-1}s^{\alpha gb}$)	α_{gb}
0	1.5×10^3	1.3×10^7	2.1×10^{-10}	8.5×10^{-7}	0.83			
0.1	1.4×10^3	2.0×10^6	3.6×10^{-10}	8.5×10^{-7}	0.86			
0.3	7.4×10^2	2.4×10^4	3.4×10^{-10}	1.8×10^{-6}	0.86	7.9×10^2	2.0×10^{-5}	0.37
0.4	5.3×10^2	1.7×10^4	2.8×10^{-10}	1.6×10^{-6}	0.86	5.2×10^2	2.7×10^{-5}	0.37
0.6	5.2×10^2	1.6×10^3	7.3×10^{-10}	5.6×10^{-6}	0.80	2.2×10^3	1.3×10^{-4}	0.37
0.7	4.2×10^2	7.3×10^2	6.2×10^{-10}	4.2×10^{-4}	0.80	9.5×10^2	2.6×10^{-5}	0.45

Table 5.6 Fitting parameters of the impedance spectra in MWCNT-[PMIM][I] mixtures to the model in **Fig. 5.2c**. R_c was not found below percolation because the model was overdetermined. C_b is the bulk capacitance; R_b is the bulk resistance; Q_{dl} is the double layer capacitance; α_{dl} is the constant phase element coefficient for Q_{dl}; R_c is the contact resistance; Q_{gb} is the grain boundary capacitance; α_{gb} is the constant phase element coefficient for Q_{gb}; R_{gb} is the grain boundary resistance; R_{ct} is the charge transfer resistance; and W is the Warburg impedance.

MWCNT wt%	R_b (Ω)	R_{CT} (Ω)	C_b ($\Omega^{-1}s$)	Q_{dl} ($\Omega^{-1}s^{\alpha dl}$)	α_{dl}	R_{gb} (Ω)	Q_{gb} ($\Omega^{-1}s^{\alpha gb}$)	α_{gb}	W ($\Omega s^{-0.5}$)	R_c (Ω)
0	4.1×10^3	5.5×10^3	2.1×10^{-10}	5.4×10^{-7}	0.87				1.4×10^{-3}	
0.2	2.1×10^3	3.9×10^3	2.8×10^{-10}	1.2×10^{-6}	0.87	2.4×10^3	7.0×10^{-6}	0.37	1.7×10^{-3}	
0.3	1.0×10^3	2.2×10^3	3.6×10^{-10}	1.1×10^{-6}	0.89	2.1×10^3	5.9×10^{-6}	0.37	1.9×10^{-3}	
0.7	6.8×10^2	2.4×10^3	3.4×10^{-10}	1.2×10^{-6}	0.87	9.0×10^2	1.3×10^{-5}	0.36	2.2×10^{-3}	
1.0	5.9×10^2		4.6×10^{-10}	9.5×10^{-7}	0.89	1.1×10^3	2.0×10^{-5}	0.37	IND	1.6×10^3

Table 5.7 Fitting parameters of the impedance spectra in N-MWCNT-[BMIM][HSO_4] mixtures to the model in **Fig. 5.2b**, except at low concentrations of N-MWCNTs, at which grain boundaries effects were small. C_b is the bulk capacitance; R_b is the bulk resistance; Q_{dl} is the double layer capacitance; α_{dl} is the constant phase element coefficient for Q_{dl}; R_c is the contact resistance; Q_{gb} is the grain boundary capacitance; α_{gb} is constant phase element coefficient for Q_{gb}; and R_{gb} is the grain boundary resistance.

N-MWCNT wt%	R_b (Ω)	R_c (Ω)	C_b ($\Omega^{-1}s$)	Q_{dl} ($\Omega^{-1}s^{\alpha dl}$)	α_{dl}	R_{gb} (Ω)	Q_{gb} ($\Omega^{-1}s^{\alpha gb}$)	α_{gb}
0	2.2×10^4	2.2×10^7	2.0×10^{-10}	6.9×10^{-7}	0.86			
0.2	2.0×10^4	2.0×10^7	1.9×10^{-10}	9.4×10^{-7}	0.82			
0.3	1.7×10^4	1.5×10^7	1.9×10^{-10}	1.0×10^{-6}	0.82			
0.8	1.2×10^4	6.2×10^6	1.9×10^{-10}	9.5×10^{-7}	0.83			
1.7	9.3×10^3	3.7×10^6	2.1×10^{-10}	1.4×10^{-6}	0.77			
2.5	7.0×10^3	1.1×10^5	1.6×10^{-10}	1.3×10^{-6}	0.80	1.5×10^{10}	1.4×10^{-5}	0.40
3.3	1.8×10^3	3.7×10^3	4.7×10^{-10}	2.8×10^{-6}	0.80	3.6×10^3	5.5×10^{-6}	0.37

5.3.2 NMR spectroscopy

I chose [BMIM][HSO_4] for NMR studies because the imidazolium-cation and anion contain the same NMR-sensitive isotope (^1H) (**Fig. 5.5a**). In the neat [BMIM][HSO_4] spectrum (blue curve of **Fig. 5.5b**) the peak around 10.4 ppm belongs to the anion isotope, while the others correspond to the cation. The peak assignment has been validated according to other NMR studies in neat ILs [102-104]. As MWCNTs are added to [BMIM][HSO_4] (top 3 spectra on **Fig. 5.5b**) there is a broadening of all the peaks. The broadening is due to inhomogeneous local magnetic fields caused by the nanoparticles [105]. A close look at the peak positions **Fig. 5.5c-e**) shows a slight deshielding (shift to higher ppm) of all the cation peaks proportional to the concentration of MWCNTs. The shift of peaks 5-6 are similar to the shifts of peaks 7-9 (not shown in the inset figure). The anion peak, however, remains almost at the same shift.

The [BMIM][HSO_4] cation-peak shifts suggest weak van der Waals interactions between the cations and the MWCNTs [46,52]. The possibility of cation-π interaction or electrostatic interactions, as suggested by some authors,[51,44] would mean a stronger shift of the hydrogen isotopes in the imidazolium ring, as they concentrate most of the positive charge. Thus, according to the spectra in **Fig. 5.5c-e**, the cation-π interaction or electrostatic interactions between the MWCNTs and cations do not appear to occur.

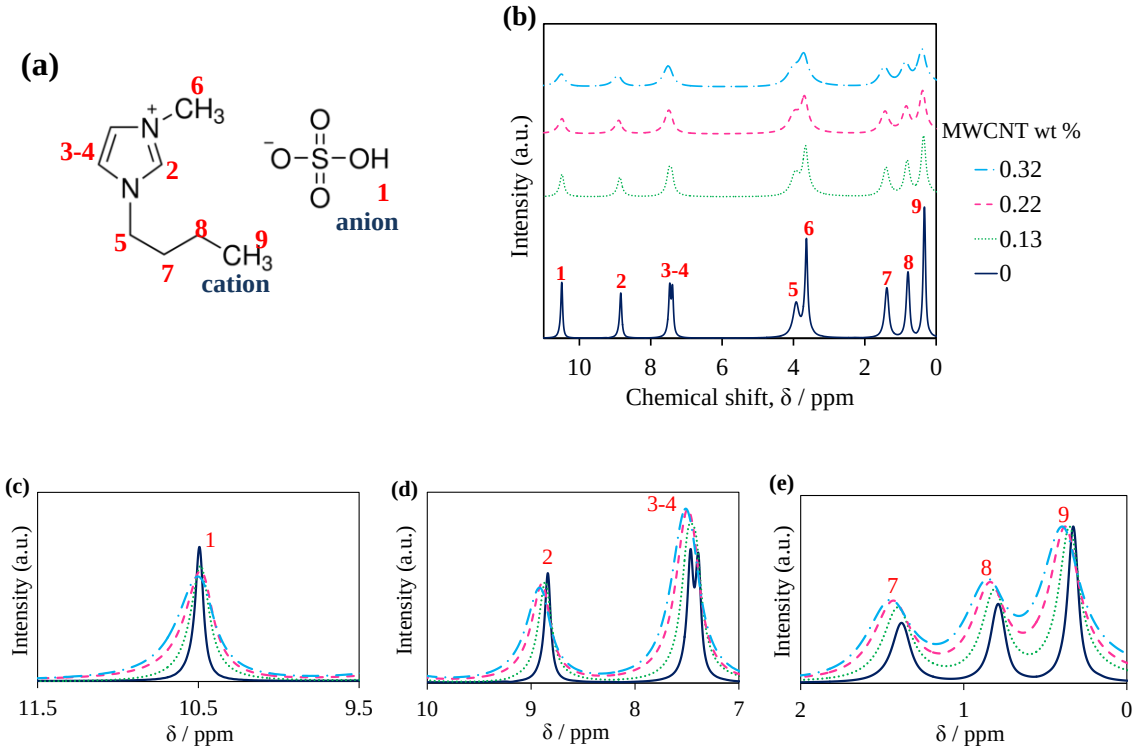

Fig. 5.5 a) Molecular structure of [BMIM][HSO_4] and hydrogen assignments. b) ^{1}H NMR spectroscopy of neat [BMIM][HSO_4] (dark blue), and MWCNT-[BMIM][HSO_4] mixtures with MWCNTs at 0.13 wt% (green), 0.22 wt% (purple) and 0.32 wt% (light blue). Close up plots of the ^{1}H spectra are shown in c, d, and e. The intensities were normalized with respect to the peak height at ~0.3 ppm (i.e., peak 9).

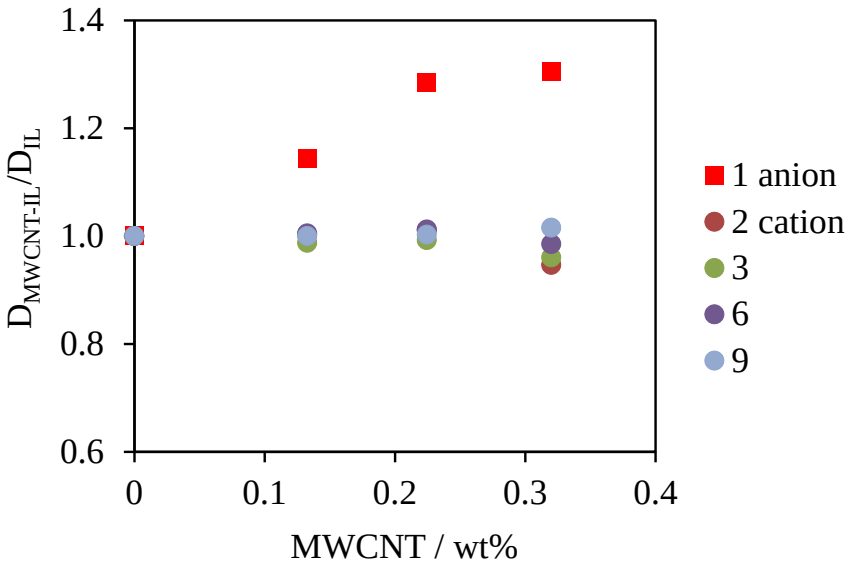

Fig. 5.6 Diffusion coefficients of [BMIM][HSO_4] mixed with MWCNTs from pulse gradient spin-echo NMR spectroscopy. $D_{MWCNT-IL}/D_{IL}$ is the ratio of the diffusion coefficient in the MWCNT-IL mixture and in the neat IL. Labels 1 through 9 correspond to the diffusion coefficients of the ^{1}H isotopes of the anion and cation shown in **Fig. 5.5a**.

The diffusion coefficients of the hydrogen isotopes are shown in **Fig. 5.6**. This plot shows that the diffusion coefficient of the anions increases as MWCNTs are added. The diffusion coefficients of the cations, however, decrease because the IL becomes more viscous with the addition of MWCNTs [106,107]. These trends provide additional evidence that weak van der Waals interactions occur between the cations of the IL and MWCNTs. A possible explanation for the increase in the diffusion coefficient of the anions is that, when the cations become attracted to the walls of the MWCNTs, some of the ion pairs are broken, which releases the anions and increases their diffusion coefficient.

To test the effect of increased negative charge in the MWCNTs on their ability to break ion pairs, we performed similar NMR studies with N-MWCNTs in [BMIM][HSO_4]. The diffusion coefficient of the anions also increases with the concentration of N-MWCNTs (**Fig. 5.7a**), but to a lesser degree than with pristine MWCNTs. In addition, **Fig. 5.7c-e** show a smaller shift of the cation peaks, compared to pristine MWCNTs, as N-MWCNTs are added to [BMIM][HSO_4]. This result suggests weaker van der Waals interaction between the N-MWCNT and the IL cations compared to the cation interaction with pristine MWCNTs. These results suggest less breaking of ion pairs because of weaker attraction of the cations to the N-MWCNTs. This weaker attraction is likely due to the smaller van der Waals radii of nitrogen compared to carbon [73]. For both MWCNTs and N-MWCNTs, there is not a significant shift of the peaks belonging to the imidazolium ring exclusively, as would be expected in cation-π interactions; thus, this makes the hypothesis of van der Waals interactions between the MWCNT walls and the IL cations more likely.

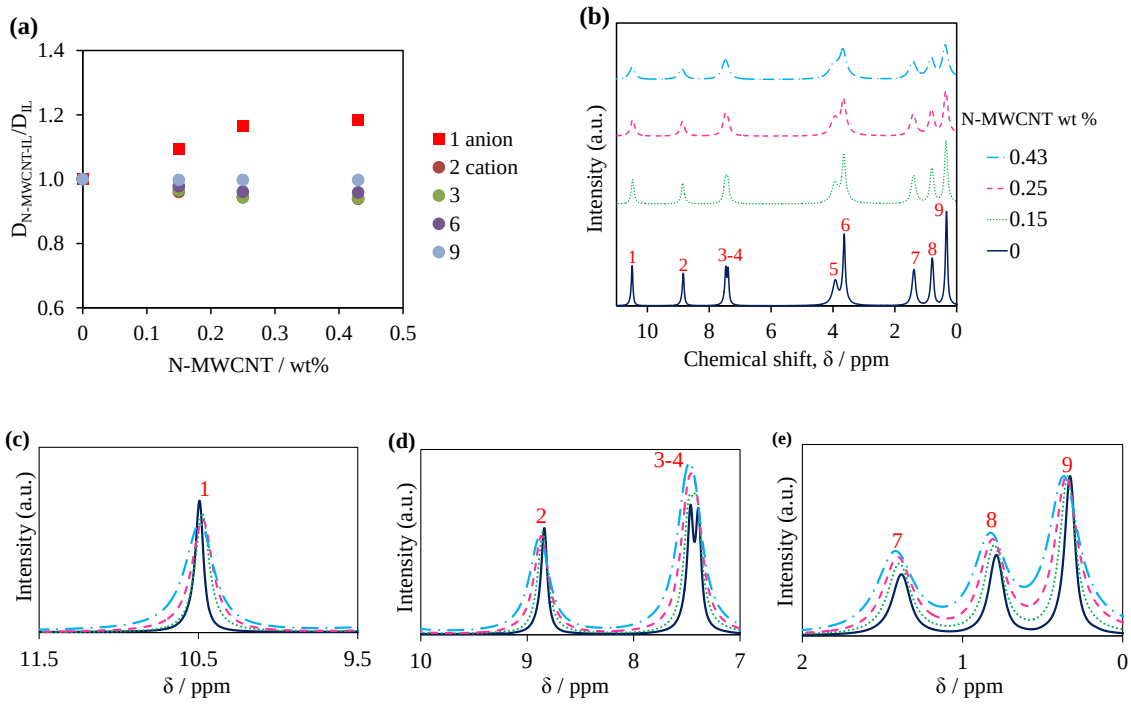

Fig. 5.7 a) Diffusion coefficients of [BMIM][HSO_4] mixed with N-MWCNTs from pulse gradient spin-echo NMR spectroscopy. $D_{N\text{-}MWCNT\text{-}IL}/D_{IL}$ is the ratio of the diffusion coefficient in the N-MWCNT-IL mixture and in the neat IL. Labels 1 through 9 correspond to the diffusion coefficients of the ^1H isotopes of the anion and cation shown in **Fig. 5.5a**. b) ^1H NMR spectroscopy of neat [BMIM][HSO_4] (dark blue), and N-MWCNT-[BMIM][HSO_4] mixtures with N-MWCNTs at 0.15 wt% (green), 0.25 wt% (purple) and 0.43 wt% (light blue). Close up plots of the ^1H spectra are shown in c, d, and e. The intensities were normalized with respect to the peak height at ~0.3 ppm (i.e., peak 9).

In summary, the results show a percolation threshold below 1 wt% of CNTs which, due to their high dispersibility in imidazolium-based ionic liquids, is 3- to 8-fold lower than the percolation threshold for CNTs in typical organic solvents. The addition of

CNTs appears to polarize their interface with imidazolium-based ionic liquids and increases the diffusion coefficient of the anions up to 35%, which is likely due to weak van der Waals interactions between the carbon nanotube walls and the cations. These effects produce a 3- to 5-fold increase in electrical conductivity of the electrolyte mixture, at CNT concentrations that are under the threshold for percolation.

CHAPTER 6. THERMO-ELECTROCHEMICAL CELLS USING CARBON NANOTUBES IN IONIC LIQUID REDOX ELECTROLYTES

6.1 Introduction

In **CHAPTER 5**, I showed that the addition of MWCNTs to IILs decreases the ohmic resistance of the solution. The conductivity changes are due to formation of percolated networks, interfacial polarization and ion-pair dissociation, as shown in **Fig. 6.1**. When an electric field is applied, the MWCNTs are polarized, and the ions are attracted to the charged surfaces (interfacial polatization), increasing the dielectric losses and ohmic conductivity [101,92]. In addition, the imidazolium cations are attracted to the MWCNT surface by weak van der Waals forces, leading to ion-pair dissociations that increase the diffusion coefficients of the anions [54,52]. In this chapter, I show that these effects can be combined to enhance the power of TECs at low wt% of MWCNTs, by balancing the increase in electrical conductivity with the reduction of open circuit voltage due to percolated networks.

Here I measure the electric power of TECs using 1-ethyl-3-methylimidazolium bis(trisfluoromethanesulfonyl) amide ([EMIM][NTf_2]) mixed with MWCNTs at different wt%. As redox couple, we use a 0.025 M equimolar tris(bipyridyl) cobalt (II) bis(trifluoromethane sulfonyl)-amide / tris(bipyridyl) cobalt (III) bis(trifluoromethane sulfonyl)-amide (Co^{II} $(bpy)_3$ $(NTf_2)_2$ / Co^{III} $(bpy)_3$ $(NTf_2)_3$). I also test [PMIM][I], as an electrolyte for TECs where the IIL act as both solvent and source of redox ions.

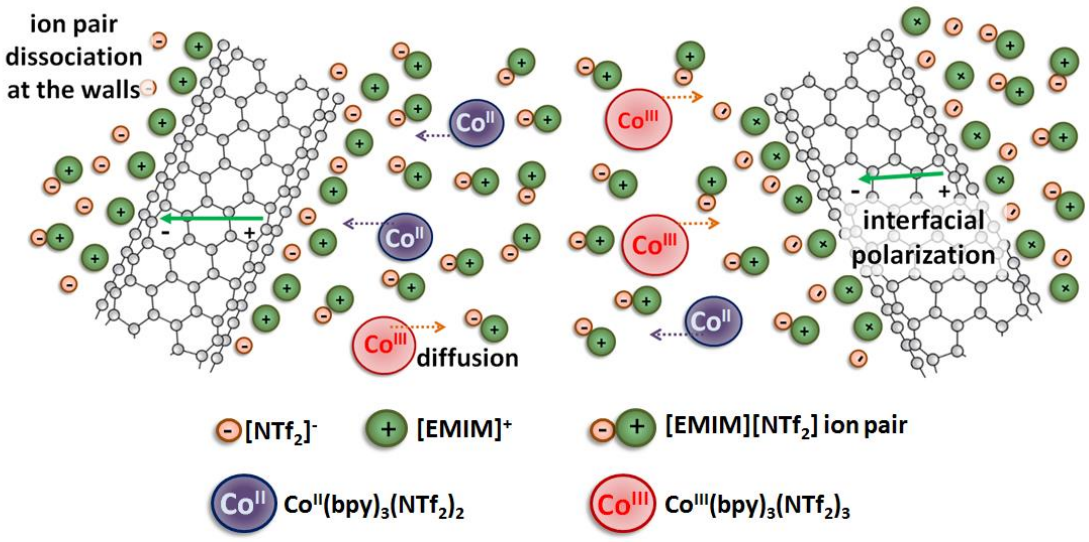

Fig. 6.1 Schematic representation of the molecular effects in MWCNT-[EMIM][NTf_2]-Co^{II}/Co^{III} electrolytes that contribute to enhanced power in TECs: ion pair dissociation and interfacial polarization at the MWCNT surface, and ionic diffusion.

6.2 Experimental details

6.2.1 Materials

[EMIM][NTf_2] and MWCNTs were purchased from IOLITEC and US-nano, respectively and used as received. According to product specifications, the MWCNTs had a length of 10-20 μm, outside diameter of 50-80 nm, and density of 2.1g/cm^3. Co^{II} $(bpy)_3$ $(NTf_2)_2$ and Co^{III} $(bpy)_3$ $(NTf_2)_3$ were synthesized by Prof. Pringle at Deakin University (Australia), following the procedure in her previous work [26]. **Fig. 6.2a** and **Fig. 6.2b** show a transmission electron micrograph (TEM) and Raman spectra of the MWCNTs used, respectively. The intensity ratio of D-band (1340 cm^{-1}) and G-band (1580 cm^{-1}) peaks is approximately 0.4, suggesting a high quality of MWCNTs. The IILs and MWCNTs were used as received.

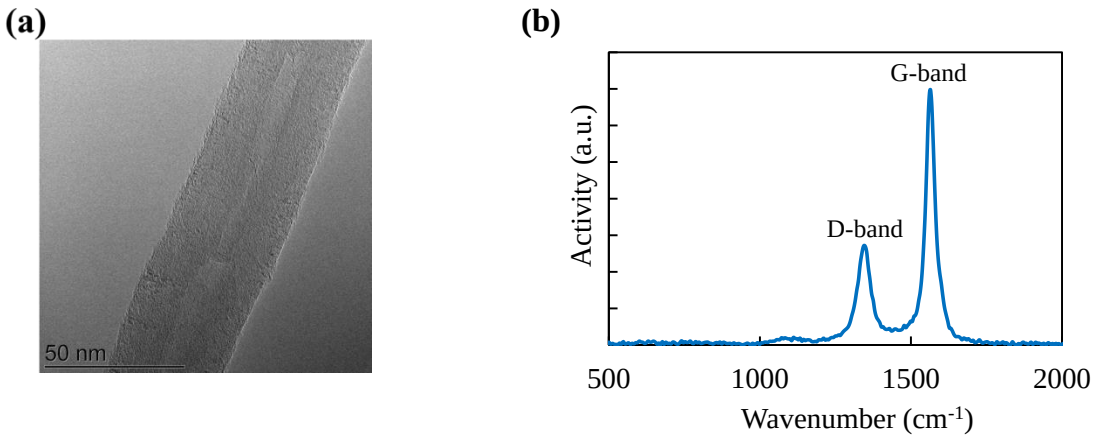

Fig. 6.2 a) TEM image of individual MWCNT. b) Raman spectrum of MWCNTs used excited by a 785-nm laser beam.

Each MWCNT-IIL mixture was prepared following the procedure described in **Section 5.2**. In the case of electrolytes with 0.025 M of $Co^{II}(bpy)_3(NTf_2)_2$ / $Co^{III}(bpy)_3(NTf_2)_3$, we added the redox couple before mixing with MWCNTs. Coulometric Karl Fischer titration (Titroline KF, Schott instruments) indicates water content less than 0.08 wt%, before and after the mixing with MWCNTs (**Table 6.1**).

Table 6.1 Water content (wt%) in [EMIM][NTf_2] at several concentrations of MWCNTs.

MWCNT (wt %)	0	0.1	0.2	0.4	0.6
Water content (wt%)	0.027	0.015	0.016	0.022	0.074

6.2.2 Viscosity measurements

The Stokes-Einstein equation relates ionic diffusion, D, and viscosity, η, as

$$D = \frac{k_b T}{6\pi\eta r} \qquad \text{eq. 42}$$

where k_b is the Planck constant and r is the radius of the redox ion. The addition of MWCNT might increase the viscosity of the mixture and block the diffusion of ions, resulting in lower TEC powers.

Viscosity measurements were performed with an MCR300 stress-controlled rheometer (Anton Paar) with standard couette geometry (CC10: 10 mm inner diameter, 10.845 mm outer diameter, and 15 mm long). The [EMIM][NTf_2]-MWCNT mixtures were prepared as described above. **Fig. 6.3** shows the viscosity, η, dependence on MWCNT wt% and temperature, *T*.

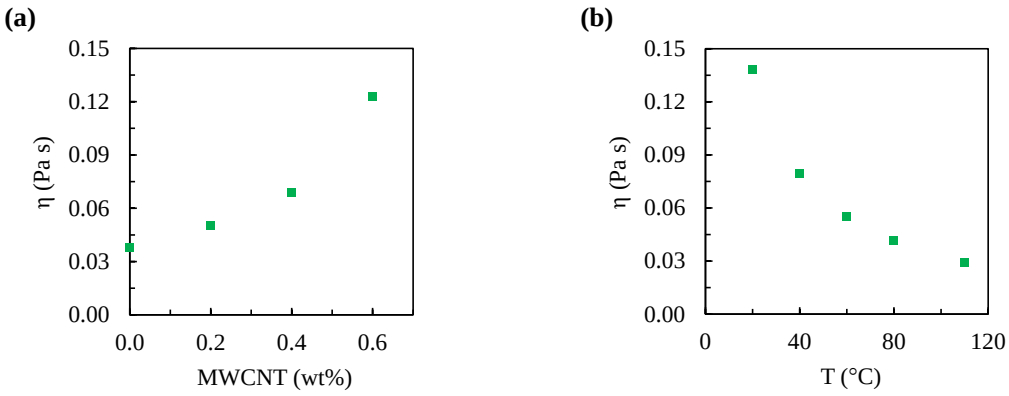

Fig. 6.3 Viscosity measurements in [EMIM][NTf_2]-MWCNT mixtures. a) Viscosity (η) at different wt% of MWCNTs. b) Temperature dependence on η of [EMIM][NTf_2] at 0.6 wt% of MWCNTs. Sampling shear rate was 100 s^{-1}.

6.2.3 Electrochemical set-up for power testing on stirring TEC

Fig. 2.8 shows a schematic representation and photograph of the stirring TEC experimental step-up. To recap the discussion in Chapter 2, the water jacket cell is connected to a chiller to control the overall temperature of the electrolyte to 22 °C. A

magnetic bar stirs the electrolyte at a rate controlled by the plate at the bottom. Two graphite electrodes (6.1 mm in diameter), separated by 25.6 mm, are immersed vertically in the electrolyte through a Polytetrafluoroethylene (PTFE) cap. Thin heater films, connected to a copper block, supply a constant power of 40 W to one electrode. Upon stirring, forced convection makes diffusive boundary layers thinner, and the system becomes ohmic limited. Even though forced convection reduces thermal gradients between the electrodes, a thermal gradient at the hot electrode/electrolyte boundary still exists. A thermoelectric effect is maintained because redox reactions happen at the electrode boundary layers.

6.2.4 Electrochemical set-up for power testing on coin-shape TEC

Fig. 2.7 shows a schematic representation and photograph of the coin-shape TEC experimental step-up. The cell consists of two platinum electrodes deposited by e-beam evaporation (100 nm) in stainless steel substrates (20 mm in diameter). The electrodes are separated (2 mm) with a polypropylene gasket and crimped at 250 psi for 30 seconds. The coin-shape TEC is sandwiched between two metal blocks. The one at the top is connected to a chiller, while the one at the bottom is connected to a thin heater film. Additional details on the coin cell step up are given in Chapter 2.

6.3 Results and Discussion

6.3.1 Electrochemical Impedance Spectroscopy

Impedance spectroscopy measurements were performed using the same electrochemical set-up as in **Section 5.2**. The ac voltage amplitude was 20 mV and the dc

signal was 0 mV. The spectra ranged from 1 MHz to 0.02 Hz. The spectra of [EMIM][NTF_2]-MWCNT mixtures, with and without 0.025 M of Co^{II} $(bpy)_3$ $(NTf_2)_2$ / Co^{III} $(bpy)_3$ $(NTf_2)_3$, were taken at three different temperatures: 22, 60 and 110 °C. The resistance was converted to conductivity using **eq. 28** and **eq. 29** in **Section 2.3**. The spectra in **Fig. 6.4** show an increase in conductivity as MWCNTs are added, as a result of the increase of interfacial polarizations. At low wt% of MWCNTs, there are also small changes at low frequencies of the dielectric spectra due to the formation of percolated networks. Above 0.3 wt% of MWCNTs, the spectra at low frequencies resemble that of a resistor, characteristic of a mixture above the percolation threshold. The addition of 0.025 M of Co^{II} $(bpy)_3$ $(NTf_2)_2$ / Co^{III} $(bpy)_3$ $(NTf_2)_3$ shows charge transfer resistances at mid-frequency ranges, but it shows similar changes in conductivity with the addition of MWCNTs.

For the case of dielectric mixtures (MWCNT-[EMIM][NTf_2]), the spectra were fit to the Debye model shown in **Fig. 5.2a**. For the case of electrolytes with redox couples, either cobalt or iodide ions, the spectra were fit to the model shown in **Fig. 5.2c**. **Fig. 6.5a, c and e** show the changes on R_b and R_c as MWCNTs are added in [EMIM][NTf_2]. The results show that R_b decreases approximately 35%, 15% and 7% at 22, 60 and 110 °C, respectively, with the addition of 0.3wt% of MWCNTs. The results also show that R_c reaches values of the same order of magnitude as R_b, and a saturation of MWCNTs, at 0.5 wt%. **Fig. 6.5b, d and e** shows changes on R_b when 0.025 M of Co^{II} $(bpy)_3$ $(NTf_2)_2$ / Co^{III} $(bpy)_3$ $(NTf_2)_3$ are added in [EMIM][NTf_2]-MWCNT mixtures. The resistance decreases as the temperature rises, due to faster diffusion of cobalt ions as well as ion pair dissociation of [EMIM][NTf_2]. All fitted values are shown in **Table 6.2** and **Table 6.3**.

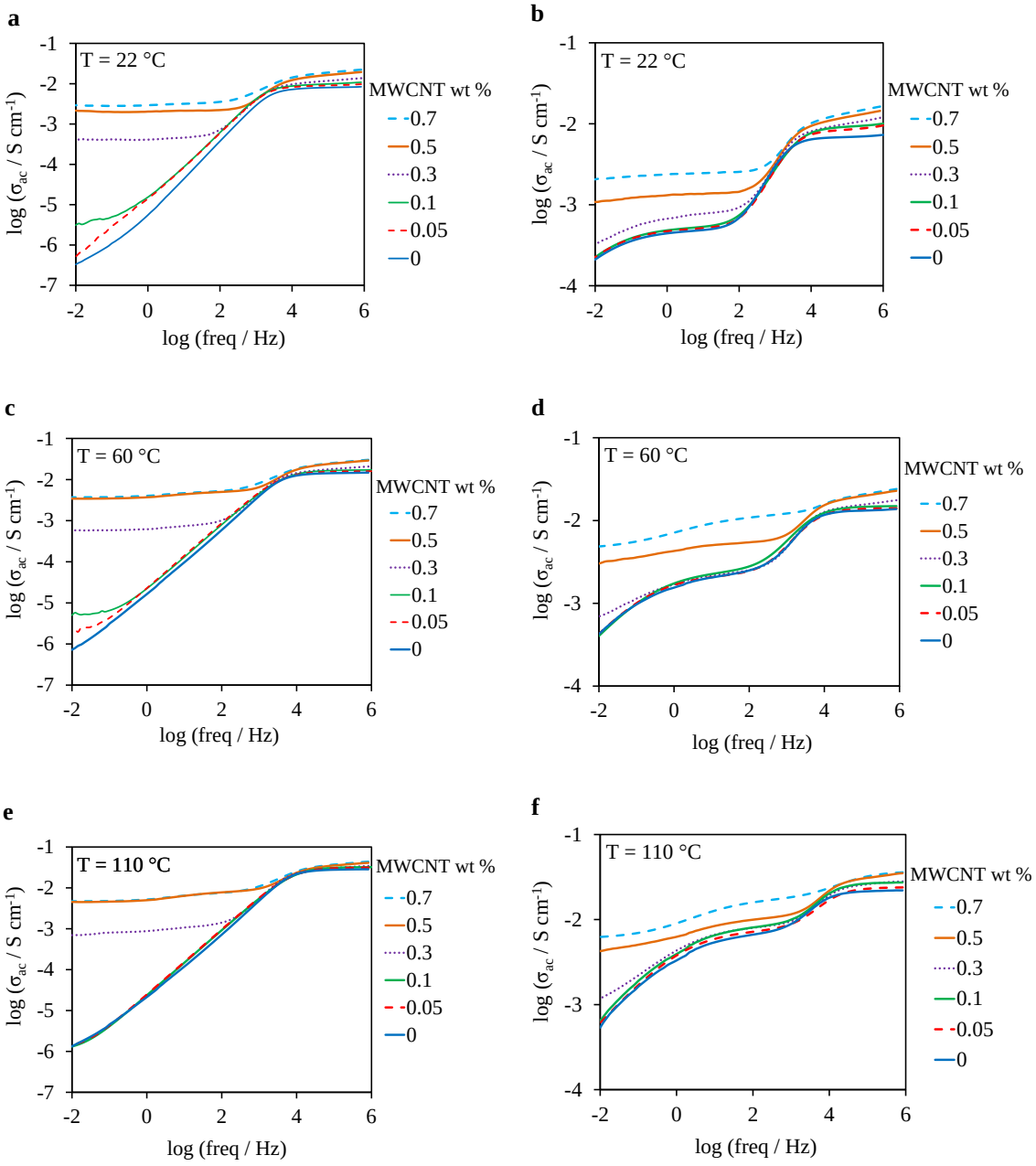

Fig. 6.4 Frequency dependence of ac conductivity, σ_{ac}, for MWCNT powders mixed in [EMIM][NTf_2] (a, c and e) and 0.025 M Co^{II} $(bpy)_3$ $(NTf_2)_2$ / Co^{III} $(bpy)_3$ $(NTf_2)_3$ - [EMIM][NTf_2] (b, d and f).

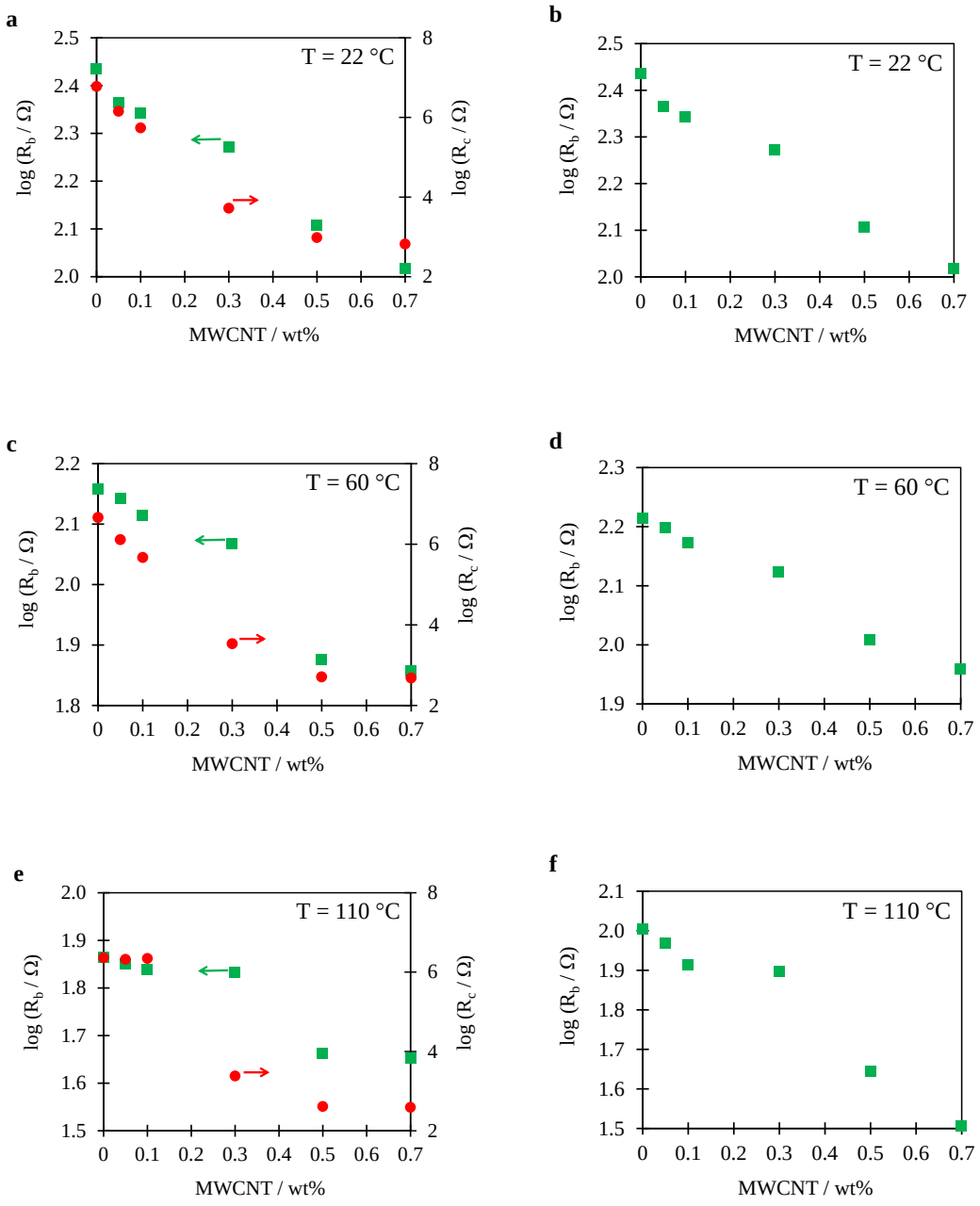

Fig. 6.5 Bulk and percolated resistance, R_b and R_c, respectively, as MWCNTs are added in [EMIM][NTf_2] at 22 °C (a), 60 °C (c) and 110 °C (e). [EMIM][NTf_2]. R_b as MWCNTs are added in 0.025 M $Co^{II}(bpy)_3(NTf_2)_2$ / $Co^{III}(bpy)_3(NTf_2)_3$ - [EMIM][NTf_2] at 22 °C (b), 60 °C (d) and 110 °C (f).

Table 6.2 Fitting parameters of the impedance spectra in MWCNT-[EMIM][NTf_2] mixtures to the model in **Fig. 5.2a**. C_b is the bulk capacitance; R_b is the bulk resistance; Q_{dl} is the double layer capacitance; α_{dl} is the constant phase element coefficient for Q_{dl}; and R_c is the contact resistance. IND: indeterminate because the model is overdetermined.

MWCNT wt%	R_b (Ω)			R_c (Ω)			Q_{dl} ($\Omega^{-1}s^{ndl}$)			α_{dl}			C_b ($\Omega^{-1}s$)		
	22 °C	60 °C	110 °C	22 °C	60 °C	110 °C	22 °C	60 °C	110 °C	22 °C	60 °C	110 °C	22 °C	60 °C	110 °C
0	2.7E+2	1.4E+2	7.3E+1	6.0E+6	4.6E+6	2.3E+6	5.6E-7	1.8E-6	2.4E-6	9.0E-1	8.0E-1	8.0E-1	5.9E-11	4.6E-11	IND
0.05	2.3E+2	1.4E+2	7.1E+1	1.4E+6	1.3E+6	2.1E+6	1.7E-6	2.3E-6	2.5E-6	8.0E-1	8.0E-1	8.0E-1	1.3E-10	6.0E-11	IND
0.1	2.2E+2	1.3E+2	6.9E+1	5.5E+5	4.7E+5	2.2E+6	1.3E-6	2.1E-6	2.4E-6	8.0E-1	8.0E-1	8.0E-1	1.6E-10	1.0E-10	IND
0.3	1.9E+2	1.2E+2	6.8E+1	5.2E+3	3.4E+3	2.4E+3	9.0E-7	1.5E-6	1.8E-6	9.0E-1	8.0E-1	8.0E-1	2.6E-10	1.9E-10	IND
0.5	1.3E+2	7.5E+1	4.6E+1	9.6E+2	5.1E+2	4.1E+2	1.2E-6	1.1E-5	7.6E-5	8.0E-1	6.0E-1	5.0E-1	2.8E-10	IND	IND
0.7	1.0E+2	7.2E+1	4.5E+1	6.6E+2	4.8E+2	3.9E+2	8.4E-6	2.3E-5	5.3E-5	7.0E-1	6.0E-1	5.0E-1	1.4E-10	IND	IND

Table 6.3 Fitting parameters of the impedance spectra in MWCNT-[EMIM][NTf_2] mixtures at 0.025 M of $Co^{II}(bpy)_3(NTf_2)_2$ / $Co^{III}(bpy)_3(NTf_2)_3$ to the model in **Fig. 5.2c**. C_b and R_c were not found because the model was overdetermined. R_b is the bulk resistance; Q_{dl} is the double layer capacitance; α_{dl} is the constant phase element coefficient for Q_{dl}; R_c is the contact resistance; R_{ct} is the charge transfer resistance; and W is the Warburg impedance. IND: indeterminate because the model is overdetermined.

MWCNT wt%	R_b (Ω)			Q_{dl} ($\Omega^{-1}s^{\alpha dl}$)			α_{dl}			W ($\Omega s^{-0.5}$)			R_{ct} (Ω)		
	22 °C	60 °C	110 °C	22 °C	60 °C	110 °C	22 °C	60 °C	110 °C	22 °C	60 °C	110 °C	22 °C	60 °C	110 °C
0	3.2E+2	1.6E+2	1.0E+2	6.4E-7	2.1E-6	2.0E-6	9.0E-1	8.1E-1	8.0E-1	1.2E+3	8.1E+2	6.1E+2	4.2E+3	8.5E+2	2.4E+2
0.05	2.6E+2	1.6E+2	9.3E+1	7.1E-7	2.2E-6	2.3E-6	8.6E-1	8.0E-1	8.0E-1	1.1E+3	7.9E+2	6.1E+2	4.1E+3	8.4E+2	2.0E+2
0.1	2.3E+2	1.5E+2	8.2E+1	9.7E-7	3.3E-6	3.1E-6	8.3E-1	8.0E-1	8.3E-1	1.1E+3	8.6E+2	5.6E+2	4.0E+3	7.6E+2	1.9E+2
0.3	2.1E+2	1.3E+2	7.9E+1	8.7E-7	2.2E-6	1.3E-6	8.5E-1	8.0E-1	8.6E-1	1.5E+3	1.1E+3	6.2E+2	3.2E+3	1.0E+3	1.9E+2
0.5	1.7E+2	1.0E+2	4.4E+1	1.1E-6	3.3E-6	1.7E-6	8.3E-1	7.5E-1	8.5E-1	IND	6.5E+2	7.8E+2	1.5E+3	6.1E+2	2.0E+2
0.7	1.5E+2	9.1E+1	3.2E+1	1.8E-6	2.6E-6	1.3E-5	7.7E-1	8.0E-1	6.4E-1	IND	6.2E+2	6.3E+2	7.9E+2	1.1E+2	8.7E+1

6.3.2 Power testing on stirring TEC

In order to reduce diffusive boundary layers and test the performance on an ohmic limited scenario, I used a stirring TEC and measured the power of [EMIM][NTf_2]-MWCNT mixtures at 0.025 M of Co^{II} $(bpy)_3$ $(NTf_2)_2$ / Co^{III} $(bpy)_3$ $(NTf_2)_3$.

Fig. 6.8 shows a reduction of the open circuit voltage, V_{oc}, as MWCNTs are added, as a result of electronic leakage by the percolated networks. As the stirring rate increases, forced convection cools down the surface temperature of the hot electrode, and the open circuit voltage decreases. Forced convection seems to partially break the conductive networks and weaken the electronic leakage when compared to V_{oc} changes at 0 rpm. **Fig. 6.7** shows an increase in the cell conductance (short circuit current, J_{sc}, over V_{oc}) as MWCNTs are added, due to the above mentioned effects: interfacial polarization, percolated networks and ion-pair dissociation. J_{sc}/V_{oc} seems to follow a power-law trend characteristic of mixtures with conductive particles below and near the percolation threshold [108,92]. When the electrolyte is stirred, reduced diffusive mass transfer resistances increase the cell conductance approximately 4-fold. The total maximum power, P_{max}, estimated as $V_{oc}J_{sc}/4$, increases as MWCNTs are added, and it is more significant at 400 rpm (**Fig. 6.8**). Although the cell conductance is lower at this rate, the higher temperature at the electrode (thus higher V_{oc}) yields a higher power than is obtained at higher stirring rates. The optimum amount of MWCNTs is reached between 0.3 and 0.5 wt%, when percolation becomes dominant. Without forced convection, the addition of MWCNTs decreases P_{max} as a result of more percolated networks; but also slower ionic diffusion in a more viscous solution, as explained in **Section 6.2.2** (**Fig. 6.3**).

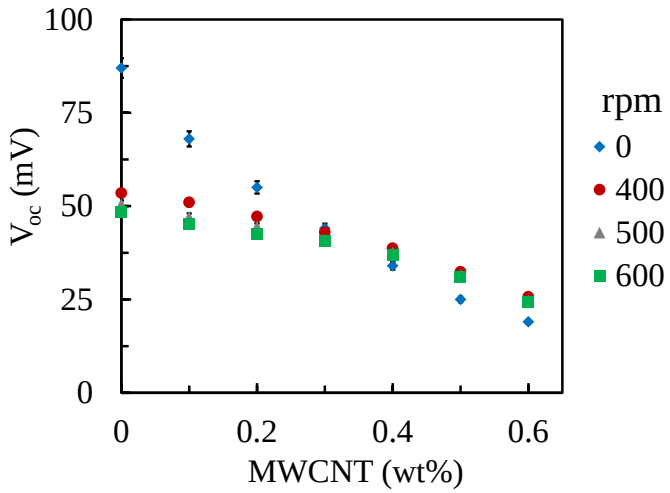

Fig. 6.6 Open circuit voltage, V_{oc}, in stirring TEC using 0.025 M of $Co^{II}(bpy)_3(NTf_2)_2$ / $Co^{III}(bpy)_3(NTf_2)_3$ in [EMIM][NTf_2] and different wt% of MWCNTs at 0 (blue squares), 400 (red circles), 500 (gray triangles) and 600 (green squares) rpm. The heat power (1.6 W cm^{-2}) and chiller temperature (22 °C) were kept constant in all measurements.

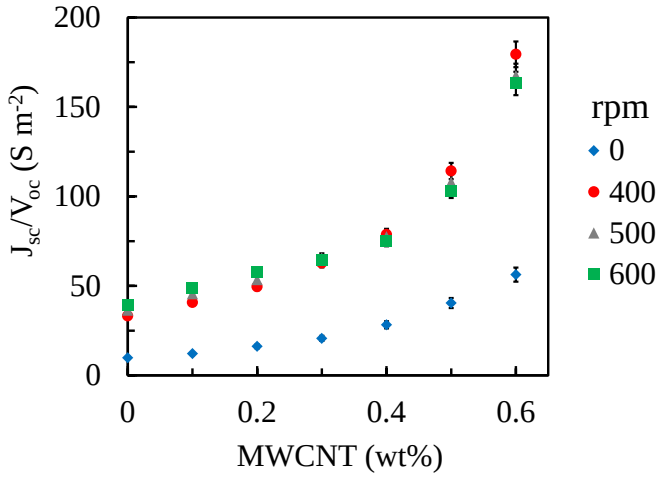

Fig. 6.7 Cell conductance, J_{sc}/V_{oc}, in stirring TEC using 0.025 M of $Co^{II}(bpy)_3(NTf_2)_2$ / $Co^{III}(bpy)_3(NTf_2)_3$ in [EMIM][NTf_2] and different wt% of MWCNTs at 0 (blue squares), 400 (red circles), 500 (gray triangles) and 600 (green squares) rpm. The heat power (1.6 W cm^{-2}) and chiller temperature (22 °C) were kept constant in all measurements.

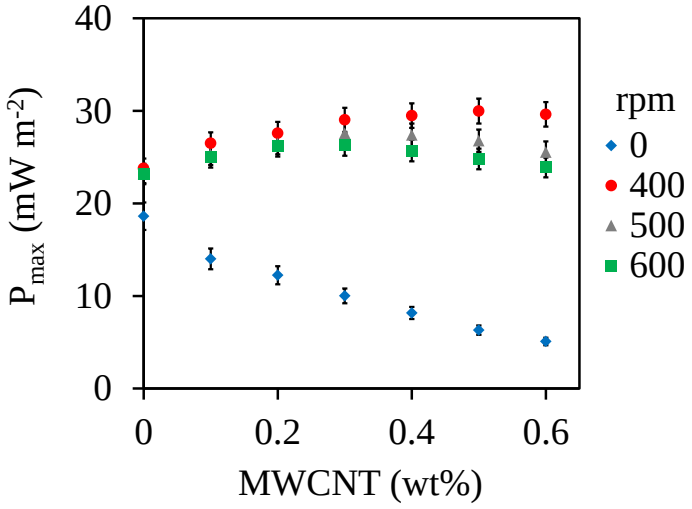

Fig. 6.8 Maximum electrical power, P_{max}, in stirring TEC using 0.025 M of $Co^{II}(bpy)_3(NTf_2)_2$ / $Co^{III}(bpy)_3(NTf_2)_3$ in [EMIM][NTf_2] and different wt% of MWCNTs at 0 (blue squares), 400 (red circles), 500 (gray triangles) and 600 (green squares) rpm. The heat power (1.6 W cm^{-2}) and chiller temperature (22 °C) were kept constant in all measurements.

6.3.3 Power testing on stagnant coin-shape TEC

I tested the performance of coin-shaped TEC with 0.025 M of $Co^{II}(bpy)_3(NTf_2)_2$ / $Co^{III}(bpy)_3(NTf_2)_3$ in [EMIM][NTf_2] at different wt% of MWCNTs. **Fig. 6.9** shows a significant reduction in the thermal-to-voltage conversion, $V_{oc}/\Delta T$, as we add MWCNTs. These changes due to percolated networks correlate with the impedance spectra results at low frequencies in **Fig. 6.4**. At higher temperatures, thermal energy partially breaks the conductive percolated networks [100], and the reduction of electronic leakage seems to vanish at higher temperature differences, as also suggested in **Fig. 6.4**. For example, at 0.1wt%, $V_{oc}/\Delta T$ increases from 1 mV/K at 17 K ΔT to 1.4 mV/K at 72 K ΔT. In these

coin-shaped TECs (2 mm electrode-electrode distance), diffusion plays a significant role in power [53]. The addition of MWCNTs increases the electrolyte viscosity, thus limiting ionic diffusion and power. **Fig. 6.3a** shows a 20% increase on the viscosity, η, of [EMIM][NTf_2], when 0.2 wt% of MWCNTs are added. This change results in lower cell conductances (J_{sc}/V_{oc}), shadowing the positive effects of interfacial polarization on ohmic conductivity, at 0.06 and 0.1wt% (**Fig. 6.10**). At 0.3 wt%, percolation is dominant, resulting in higher cell conductance than at 0 wt%. As the average cell temperature increases, the viscosity of [EMIM][NTf_2]-MWCNT mixtures decrease (**Fig. 6.10**) and the cell conductance increases. Both, percolation and slower diffusion reduces the total TEC power as MWCNTs are added (**Fig. 6.11**).

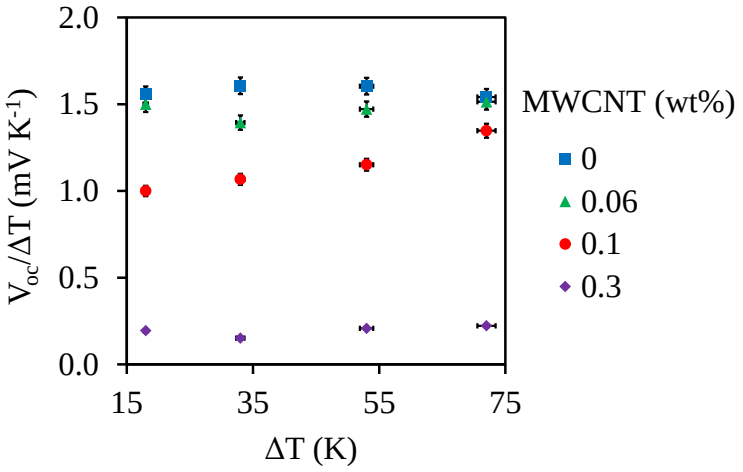

Fig. 6.9 Open circuit voltage, V_{oc}, in coin TEC using 0.025 M of Co^{II} $(bpy)_3$ $(NTf_2)_2$ / Co^{III} $(bpy)_3$ $(NTf_2)_3$ in [EMIM][NTf_2] and 0 (blue squares), 0.06 (green triangles), 0.1 (red circles) and 0.3 (purple diamonds) wt% of MWCNTs. ΔT is the temperature difference between the electrodes. The temperature at the cold electrode was set at 296 K in all the measurements.

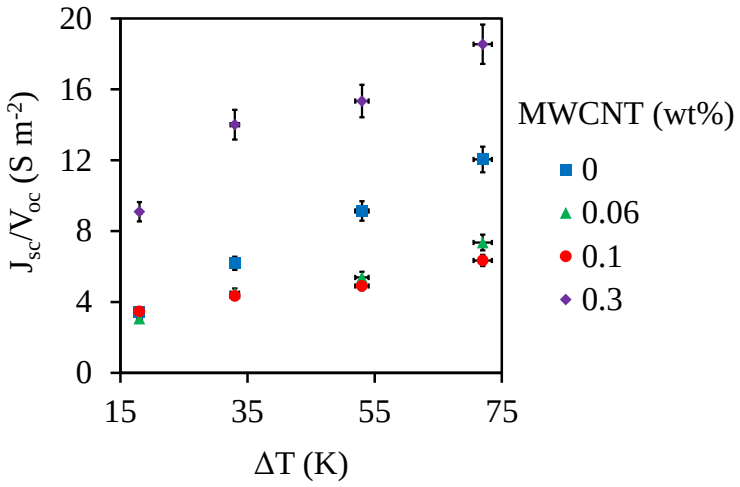

Fig. 6.10 Cell conductance, J_{sc}/V_{oc}, in coin TEC using 0.025 M of Co^{II} $(bpy)_3$ $(NTf_2)_2$ / Co^{III} $(bpy)_3$ $(NTf_2)_3$ in [EMIM][NTf_2] and 0 (blue squares), 0.06 (green triangles), 0.1 (red circles) and 0.3 (purple diamonds) wt% of MWCNTs. ΔT is the temperature difference between the electrodes. The temperature at the cold electrode was set at 296 K in all the measurements.

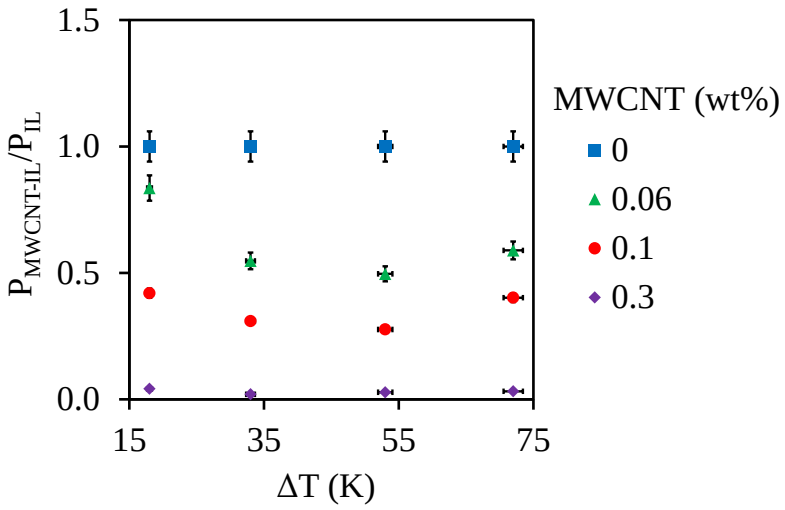

Fig. 6.11 Relative power, $P_{MWCNT-IL}/P_{IL}$, in coin TEC using 0.025 M of Co^{II} $(bpy)_3$ $(NTf_2)_2$ / Co^{III} $(bpy)_3$ $(NTf_2)_3$ in [EMIM][NTf_2] and 0 (blue squares), 0.06 (green triangles), 0.1 (red circles) and 0.3 (purple diamonds) wt% of MWCNTs. $P_{MWCNT-IL}/P_{IL}$ is the ratio of maximum power using MWCNTs and without them. ΔT is the temperature difference between the electrodes. The temperature at the cold electrode was set at 296 K in all measurements.

In **CHAPTER 5**, I showed that the addition of MWCNTs to IILs dissociates the ion pairs and releases and increases the average diffusion coefficient of the anions. To test the effect of ion pair dissociation on TEC power, I chose a solvent-free redox electrolyte [PMIM][I]. The coin-shape cells were tested under two different temperature differences, 25 and 48 K. **Fig. 6.12** shows a thermal-to-voltage conversion, $V_{oc}/\Delta T$ of 0.12 mV/K without MWCNTs, lower than in the 1.6 mV/K in cobalt electrolytes (**Fig. 6.9**). The thermoelectric effect at 0.1 wt% remains similar to 0 wt%, decreasing significantly at 0.2 wt% of MWCNTs due to percolated networks. The cell conductance, J_{sc}/V_{oc}, increases with the addition of MWCNTs (**Fig. 6.13**). At 0.05 and 0.1 wt%, the

changes are due to ion-pair dissociation and interfacial polarization, since percolation starts to be dominant at 0.2 wt%. These effects result in up to a 30% increase in power density (**Fig. 6.14**). Even though the cell is diffusion limited, the likely dissociation of $[PMIM]^+$ and $[I]^-$ ions increases the average diffusion coefficient of $[I]^-$ ions, significantly improving the cell power density.

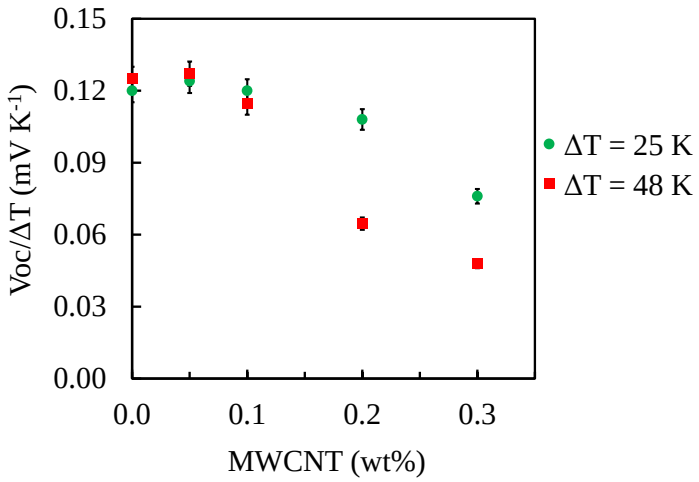

Fig. 6.12 Open circuit voltage, V_{oc}, in coin TEC using [PMIM][I]-MWCNT mixtures at ΔT = 25 K (green circles) and ΔT = 48 K (red squares). The temperature at the cold electrode was set at 288 K in all the measurements.

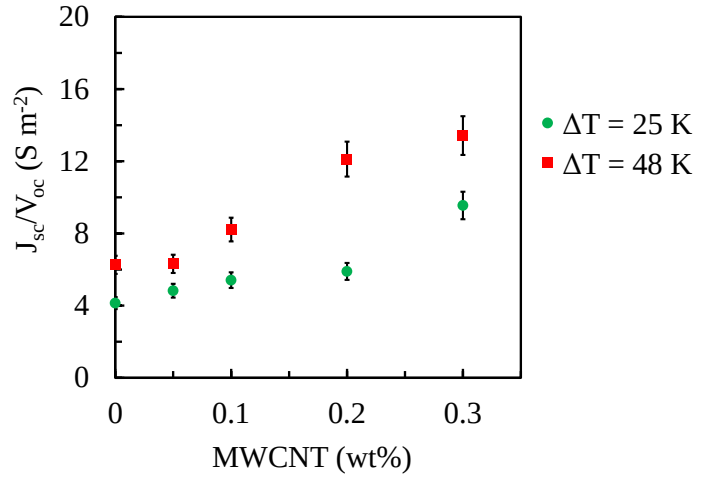

Fig. 6.13 Cell conductance, J_{sc}/V_{oc}, in coin TEC using [PMIM][I]-MWCNT mixtures at ΔT = 25 K (green circles) and ΔT = 48 K (red squares). The temperature at the cold electrode was set at 288 K in all the measurements.

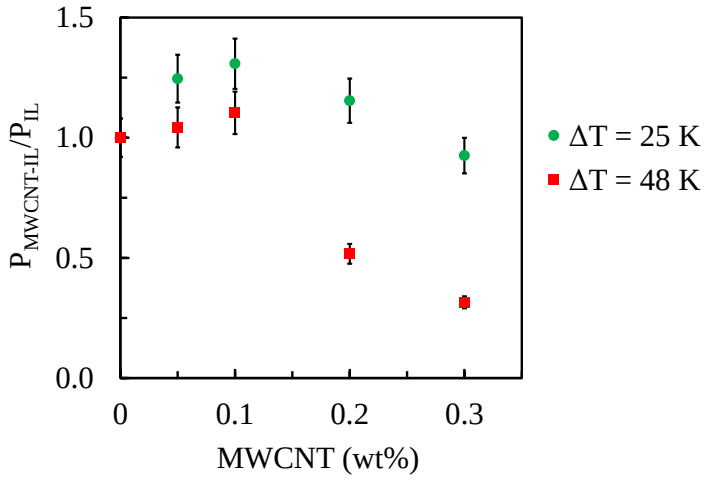

Fig. 6.14 Relative power, $P_{MWCNT-IL}/P_{IL}$, in coin TEC using [PMIM][I]-MWCNT mixtures at ΔT = 25 K (green circles) and ΔT = 48 K (red squares). $P_{MWCNT-IL}/P_{IL}$ is the ratio of maximum power using MWCNTs and without them. The temperature at the cold electrode was set at 288 K in all measurements.

Table 6.4 shows the thermal to voltage conversion, $V_{oc}/\Delta T$, and relative short circuit current, $J_{sc}/\Delta T$, of two coin-like cells tested immediately after crimping of the cell (day 1) and after 30 days of resting at open circuit (day 30). The samples were left at ambient conditions after initial testing (day 1) for 30 days. The same samples were then rested at the same temperature differences. The results suggest a good stability of the mixture and platinum electrodes. The results fall within the 3% uncertainty on the open circuit voltage and 8% uncertainty on the short circuit current.

Table 6.4 Stability test of CoII/III-[EMIM][NTf_2]-MWCNT and [PMIM][I]-MWCNT electrolytes in coin-like cells.

	$Co^{II/III}$ (day 1/ day 30)		[PMIM][I] (day 1/day 30)	
MWCNT (wt %)	0	0.06	0	0.05
$V_{oc}/\Delta T$ (mV/K)	1.61/1.59	1.40/1.42	0.120/0.122	0.125/0.123
$J_{sc}/\Delta T$ (mA/m^2K)	9.9/9.8	6.8/7.0	0.50/0.46	0.60/0.52

In summary, the results show that the addition of MWCNTs to redox ILs enhances the electrical conductivity, and, at low concentration of MWCNTs (less than 0.5 wt%), increases the electric power generation of thermocells by as much as 1.3 times the original power. This increase in power results from reduced mass transfer resistances through interfacial polarization and ion pair dissociation, and by optimizing the concentration of MWCNTs to minimize electronic leakage.

CHAPTER 7. CONCLUSIONS AND RECOMMENDATIONS

7.1 Conclusions

Thermo-electrochemical cells (TECs) are devices that convert waste heat to electricity inexpensively. Current TECs, however, operate at low conversion efficiencies.

CHAPTER 3 reveals key features that must be considered in the design of TECs, and highlights points of performance optimization and limitation. The diffusive boundary layer at the electrodes was shown to limit the current densities of TECs. Natural convection in conventional TECs was shown to compress the boundary layers and increase mass and heat transfer depending on their ion diffusivity and thermal diffusivity coefficients, respectively. In conventional TECs with 1 mm thickness and a temperature difference of 60 °C, natural convection increases mass transfer of the electrolyte by a factor of 8; however, heat flux across the electrodes increases by only a factor of 1.5 due to natural convection. The net effect of natural convection is thus an enhancement of the energy conversion efficiency of TECs, compared to TECs with stagnant electrolyte. Although larger cell dimensions could strengthen natural convection, the high ionic resistivity would then limit the output power and efficiency. Numerical results show that series stacking of TECs increases the overall conversion efficiency by optimizing the impact of natural convection on mass and heat transfer in the individual cells. In a flow cell TEC design, forced convection lowers the concentration overpotentials; however the power is limited by the low ionic conductivity of the electrolyte. The ohmic potential drop consumes about 70% of the open circuit voltage generated in a flow cell TEC.

The results in **CHAPTER 4** suggest that the process of doping CNT electrodes can change the electroactive surface area by as much as 3- to 4-fold. In addition, electrostatic interactions between counterions and the electrodes should be considered in the search for electrodes with improved electron transfer kinetics. Doped CNT electrodes did not exhibit an apparent change in the kinetic transfer coefficient with the ferri/ferrocyanide redox couple, which indicates that the reaction is adiabatic.

In **CHAPTER 5**, EIS showed lower percolation thresholds of MWCNTs in [BMIM][PF_6], [BMIM][HSO_4] and [PMIM][I], than in organic solvents (DMF and DMSO), which provides clear evidence for their high dispersibility in imidazolium-based ILs. This high dispersibility is probably due to weak van der Waals interactions between the MWCNT walls and imidazolium cations, as indicated by NMR data. In addition, diffusion NMR showed an increase in the diffusion coefficient of the anions only as MWCNTs are added to the ILs. EIS also showed a 3 to 5-fold decrease of the bulk resistance of the IL-MWCNT mixtures, before reaching the percolated state. The optimum amount of MWCNTs to be added will depend on maximizing the effect of interfacial polarization and reducing the bulk ohmic resistance, while minimizing the formation of percolated networks.

CHAPTER 6 shows that the addition of MWCNTs improves the power of IL-based TECs, in spite of electronic leakage that reduces the open circuit voltage. The optimum amount of MWCNTs to be added depends on maximizing the effect of interfacial polarization and reducing the bulk ohmic resistance, while minimizing the formation of percolated networks. In [PMIM][I], the MWCNTs dissociates the ion pairs, increasing the mobility of redox [I] ions. This results in a 30% power increase in stagnant

TECs with the addition of 0.1 wt% of MWCNTs. However, in [EMIM][NTf_2] with cobalt redox couples, the addition of MWCNT limits the diffusion of cobalt ions, resulting in lower power for stagnant TECs. In stirring TECs, forced convection reduces the diffusive boundary layers, and the system becomes ohmic limited. The addition of MWCNTs to [EMIM][NTf_2]-cobalt electrolytes increases their ohmic conductivity due to interfacial polarization. This positive effect overcomes the open circuit reduction, and results in a 25% power increase with the addition of 0.4 wt% of MWCNTs at 400 rpm. The importance of these results is not limited to TECs, but can be extended to other IL-based electrochemical devices, such as redox flow batteries, dye solar cells or fuel cells.

The novel contributions of this work to the current research on TECs are:

- The estimation of the effect of natural and forced convection, as well as cell geometry, on the conversion efficiency of TECs.
- The enhancement of conversion efficiency (predicted) of TECs, when stacked in series.
- The enhancement of the internal surface area of MWCNT electrodes by PECVD doping.
- The electrokinetic changes on doped MWCNT electrodes.
- The ohmic resistance reduction of ILs with the addition of MWCNTs, as a result of interfacial polarizations.
- The enhancement of ionic diffusion coefficients of IILs with the addition of MWCNTs, as a result of ion pair dissociation.
- The effect of percolated MWCNT networks and electronic leakage on the open circuit voltage of TECs.

- The power enhancement of IL-based TECs with the addition of MWCNTs, as a result of interfacial polarizations and ion pair dissociation.

7.2 Recommendations

7.2.1 Maximizing interfacial polarization

The TEC power using CNT-IL mixtures could be further increased by maximizing interfacial polarizations. NMR results suggest that imidazolium cations are attracted to nanotube walls by weak van der Waals interactions. As the cations are trapped at the walls, the dipoles at the interface require more energy in order to align in the direction of the electric field, thus increasing dielectric losses and decreasing the solution ohmic resistance.

CNTs with more imperfections at the surface could trap more cations at the walls and increase dielectric losses. Plasma or chemical treatments are two conventional methods to create surface imperfections. Alternatively, instead of particles with high aspect ratio such as CNTs, spherical conductive particles would allow higher wt% of particles, thus increasing the effect of interfacial polarizations.

7.2.2 Novel ILs and redox couples

Following the work of Abraham et al. [26], further improvement of TECs requires the synthesis of novel redox couples or ionic liquids. Some guidelines or constraints to follow are:

- Redox couples with fast kinetics and high solubility. Generally, redox couples based on metal complexes have fast electrode-kinetics due to their high electron density

near their Fermi level. In addition, their ligands and counterions could also play an important role, not only in the kinetics, but also in the redox couple solubility in ILs. A highly soluble redox couple allows high concentrations at the electrode surface, thus high electric currents following **eq. 9 and 10**. In an ideal case, the synthesis of an IL having a redox metal in the anion will allow the maximum solubility and kinetics possible. The maximum TEC power is reached using an equimolar concentration of reduced and oxidized redox couples [9]. Thus, the synthesis procedure has to be applicable to both reagent types.

- Redox couples with high reaction entropies. There is not yet a full understanding of the physical chemistry behind redox reaction entropies. Hupp *et al*. proposed correlations of reaction entropies with the molecular radius, valence and solvent [4]. However, the discovery of novel redox couples/ionic liquids mixtures requires an intensive computational screening at the molecular level. The inclusion of solvent or nanoparticles molecules in ab-initio simulations can be time expensive, but the simulations can be combined with molecular dynamics to speed up the screening.
- Ionic liquids mixed with carbon nanotubes. Longer cations could increase their total van der Waals attraction to the nanotube walls, thus trapping more dipoles at the interface. In addition, longer cations will have weaker ionic interactions with the anions, reducing the IL viscosity and increasing the diffusion coefficient of the redox couple. Although all the ionic liquids tested in this thesis have a imidazolium ring in the cation, other IL with similar rings such as pyrazolium or pyridinium could lead to strong interactions with CNT walls. Alternatively, quinolium cations which have 2 rings could optimize the interfacial polarizations. Effective medium theory

approaches could be used to estimate the diffusion, thermal conductivity and electrical conductivity changes in IL-MWCNT mixtures or other mixtures with conductive particles [109-111]. These models can be used as a first approximation of electrical and thermal conductivity at low concentration of conductive particles. However, these models does not consider the electrical double layer interactions or the effect of ionic concentration in the mixture, or fail to predict the changes near the percolation threshold.

7.2.3 Optimizing the electrode surface area

Fig. 4.3 showed the similar electrokinetics of platinum and MWCNT electrodes. However, the expected higher internal surface area of MWCNT electrodes did not increase the peak currents in cyclic voltammetry with potassium ferri/ferrocyanide electrolytes. Plasma treatment of MWCNT electrodes seems to break the carbon-carbon bonds, enlarge the pore size and allow diffusion of ferri and ferrocyanide ions in the electrode. As a result, cyclic voltammetry of nitrogen and boron-doped MWCNTs showed higher current peaks than pristine MWCNTs. This plasma, or chemical treatment, could be optimized to further enhance the internal surface area. Alternative electrodes, less expensive and with similar electrokinetics, could be explored as well. This electrode search is particular to the electrolyte used. As shown in **section 4.4**, electrostatic interactions at the electrode/electrolyte interface plays a significant role in the electrokinetics and TEC power. The pore diameter and porosity of the electrode could be optimized by extending the model developed in CHAPTER 3. The model can then be used to find the optimum porosity that would maximize the TEC power but, that will also maintain the high thermal conductivity of the electrode and avoid thermal drops at the

interface. The model could also be extended to a three dimensional model and, non-dimensional parameters could be used to identify the optimum conversion efficiency at different cell geometries.

7.2.4 Thermal conductivity vs ionic diffusion

In redox electrolytes, heat transfer rate is mainly dependent on the thermal conductivity of solvent molecules. Ionic diffusion also has a contribution in the heat transfer rate due to the Dufour effect, but it is typically small (equation 2). The thermal conductivity of the electrolyte then depends on the heat transported through molecular collisions of solvent molecules. On the other hand, ionic diffusion is inverse proportional to the viscosity of the solvent and ionic radius (equation 42). In order to maximize the conversion efficiency of TECs, it is important to find a solvent with low thermal conductivity, but also low viscosity that will result in fast ionic diffusion.

APPENDICES

A. Thermo-electrochemical cell Comsol model

A snapshot of the Comsol model used for the simulations in **CHAPTER 3** is shown below. **Fig. A.1** shows all the physics implemented in the model, which are, fluid dynamics, mass transfer, electrokinetics and heat transfer. **Fig. A.2** shows a snapshot of the grid layout for a 1mm square TEC model.

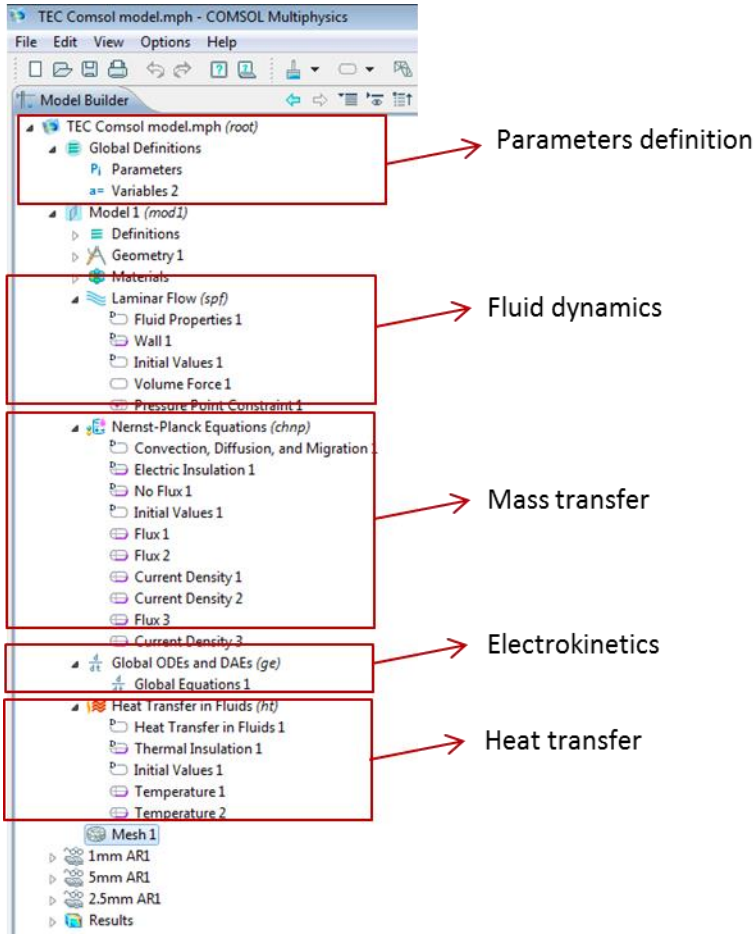

Fig. A.1 Snapshot of the TEC Comsol model showing the different studies implemented.

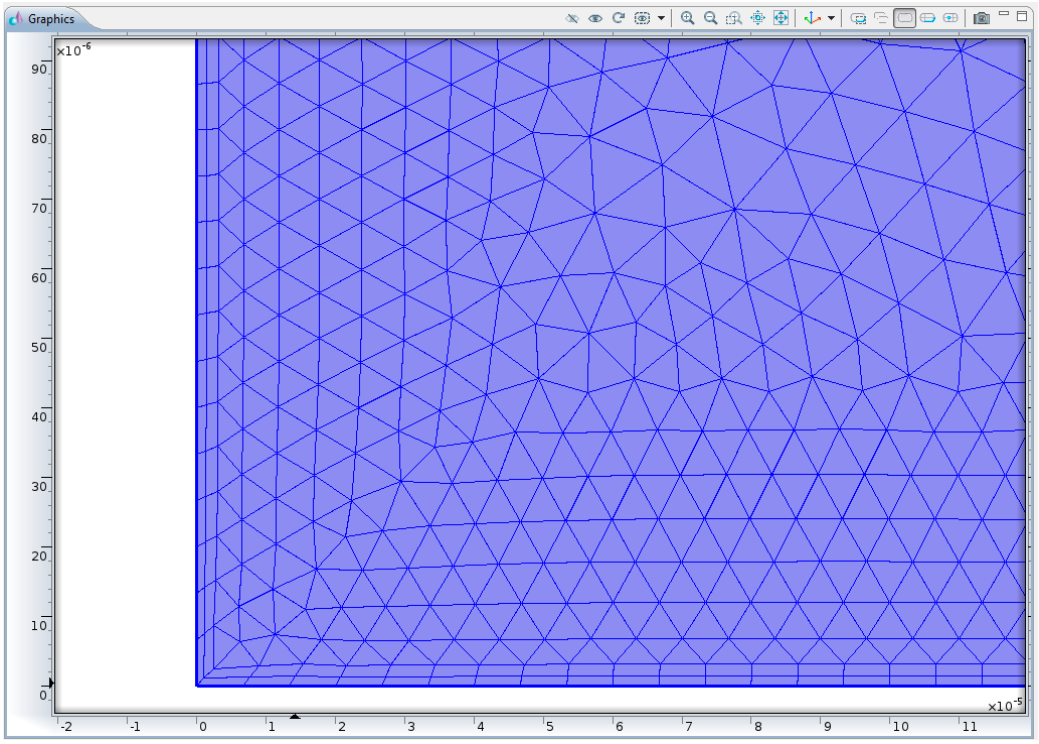

Fig. A.2 Snapshot of the grid used for a 1 mm square TEC model. The units are in meter.

B. Thermal conductivity of MWCNT-IL mixtures

Fig. B.1 shows the thermal conductivity changes, k, of IILs with the addition of MWCNTs. The results show a 5 to 10% increase of thermal conductivity with the addition of 0.5 wt% of MWCNTs. Compared to the changes on electrical conductivity, **section 5.3** showed that the addition of approximately 0.5 wt% to these ILs reduces their ohmic resistance 5 to 10-fold. The results then suggest that the addition of MWCNT to IL electrolytes will have a negligible change in the electrode temperature difference of TECs.

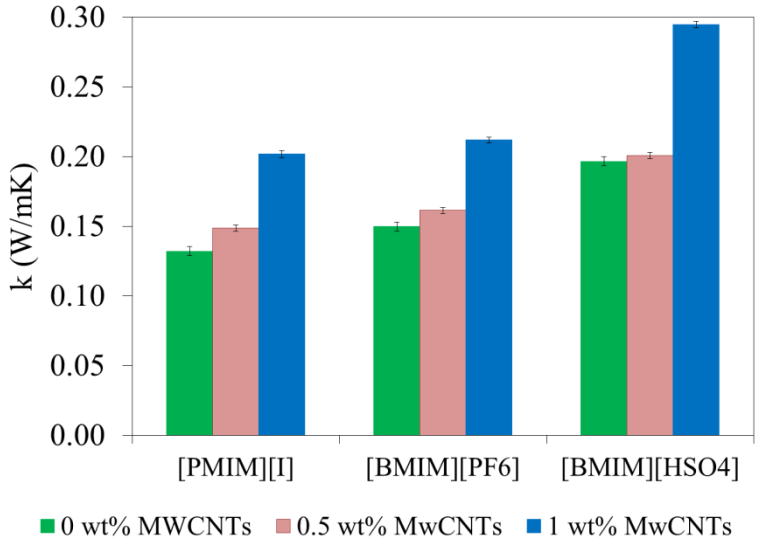

Fig. B.1 Thermal conductivity, k, of [PMIM], [BMIM][PF_6] and [BMIM][HSO_4] at 0 (green bars), 0.5 (pink bars) and 1 wt% (blue bars) of MWCNTs.

C. Ab-initio modeling of redox couples

Ab-initio simulations can be used to prescreen potential novel redox couples for TECs. Fig. C.1 shows the electronic distribution and molecular orbitals of potassium ferri/ferrocyanide in water. The LUMO (lowest unoccupied molecular orbital) of potassium ferricyanide is at approximately at -3 eV, clearly separated from the next unoccupied molecular orbitals. This suggests a high tendency, and probably fast kinetics, to be reduced. Similarly, the HOMO (highest unoccupied molecular orbital) of potassium ferrocyanide is clearly separated from the next occupied molecular orbital, suggesting a tendency to be reduced.

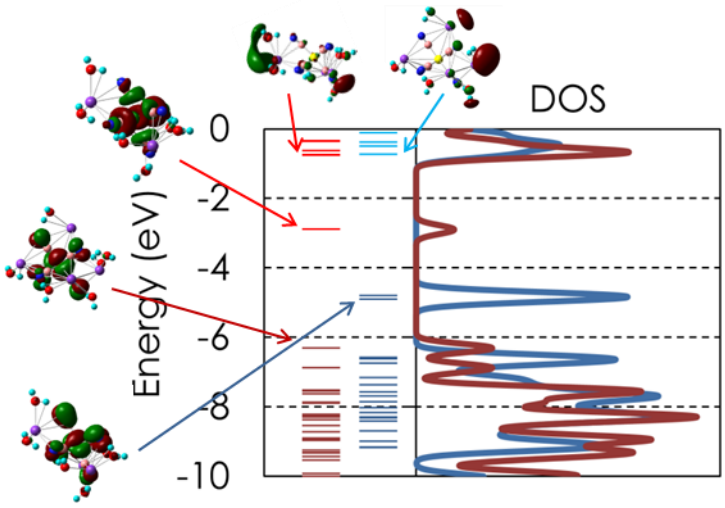

Fig. C.1 Density of States (DOS) Electronic distribution of potassium ferri/ferrocyanide in water. Blue for the reduced reagent and red for the oxidized reagent. Molecular orbitals of the energy states near the Fermi level. Light colors for unoccupied states and dark colors for occupied states.

D. Platinum dispersed particles on carbon nanotubes

Novel redox couples require fast kinetics, high solubility, high reaction entropies and chemical stability. These conditions may not always be accomplished. Some redox couples will require platinum electrodes to maintain a fast kinetics. In this scenario, the dispersion of platinum particles on CNT electrodes will reduce materials costs while maintaining a fast kinetics and providing a high internal surface area.

Dai et al. proposed a substrate-enhanced electroless procedure for the deposition of platinum particles on SWCNTs [112]. For depositing platinum on MWCNTs, I followed a similar procedure. First, I ultrasonicated for 30 minutes a mixture of 20 mg of MWCNT powder and 20 mL of DI water. Then I added 8 to 10 Zn pellets of 3 mm in diameter along with a magnetic stirrer. While stirring for 30 seconds, I added 3 mL of

0.02 M Na_2PtCl_4, and then stopped the stirring for 30 seconds. This on/off stirring cycle was repeated 8 times in order reach a uniform distribution of platinum particles. The MWCNTs were then filtrated and dried at 100 °C for 2 hours. SEM and XPS analysis (**Fig. D.1** and **Fig. D.2**, respectively) show a 1.5 wt% deposition of 20 to 30 nm-radius platinum particles at the nanotube walls.

The next step in the electrode preparation will be the binding of the modified MWCNTs using a conventional powder adhesive, such as polyvinylidine fluoride (PVDF). The kinetics and internal surface area with a particular redox couple can be analyzed using cyclic voltammetry.

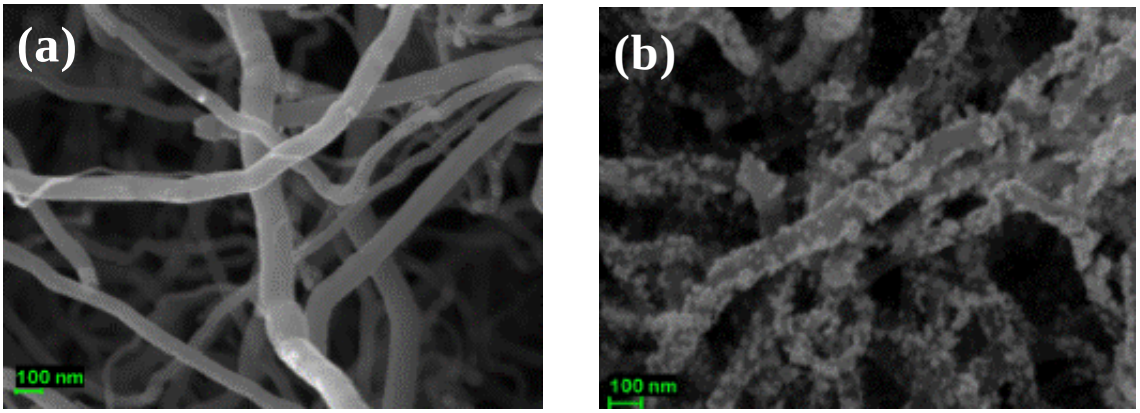

Fig. D.1 SEM screenshots of MWCNTs (10-20 um long and 50 nm in diameter) before (a) and after (b) platinum deposition. Picture b shows a deposition of platinum particles with an estimated diameter of 20 to 30 nm.

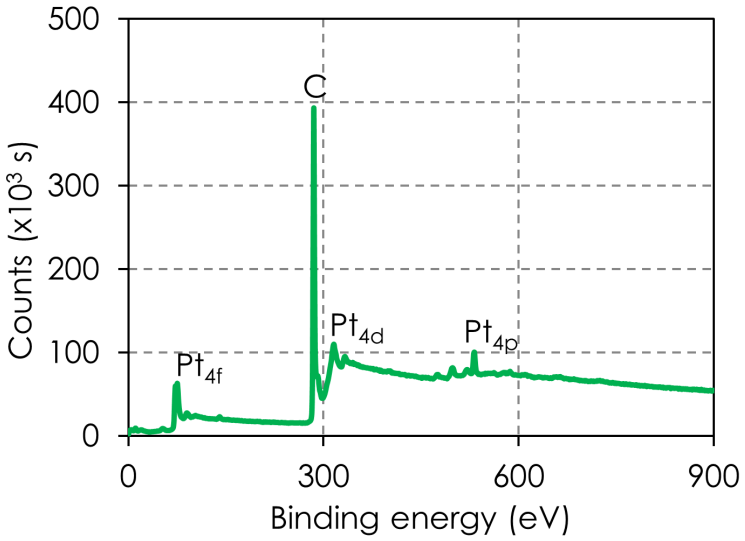

Fig. D.2 XPS analysis of MWCNT powders after platinum deposition. The spectra show several valence peaks corresponding to platinum, and an estimated deposition of 1.5 wt%.

REFERENCES

1. DOE (2008) Waste Heat Recovery: Technology and Opprotunities in U.S. Industry. Waste Heat Recovery: Technology and Opprotunities in U.S. Industry.

2. Quoilin S, Broek MVD, Declaye S, Dewallef P, Lemort V (2013) Techno-economic Survey of Organic Rankine Cycle (ORC) systems. Renewable and Sustainable Energy Reviews 22 (0):168-186. doi:http://dx.doi.org/10.1016/j.rser.2013.01.028

3. DOE (2006) Engineering Scoping Study of Thermoelectric Generator Systems for Industrial Waste Heat Recovery. Engineering Scoping Study of Thermoelectric Generator Systems for Industrial Waste Heat Recovery.

4. Hupp JT, Weaver MJ (1984) Solvent, ligand, and ionic charge effects on reaction entropies for simple transition-metal redox couples. Inorganic Chemistry 23 (22):3639-3644. doi:10.1021/ic00190a042

5. Daum PH, Enke CG (1969) Electrochemical kinetics of the ferri-ferrocyanide couple on platinum. Analytical Chemistry 41 (4):653-656. doi:10.1021/ac60273a007

6. Nugent JM, Santhanam KSV, Rubio A, Ajayan PM (2001) Fast Electron Transfer Kinetics on Multiwalled Carbon Nanotube Microbundle Electrodes. Nano Letters 1 (2):87-91. doi:10.1021/nl005521z

7. Sokirko AV (1994) Theoretical study of thermogalvanic cells in steady state. Electrochimica Acta 39 (4):597-609. doi:Doi: 10.1016/0013-4686(94)80106-1

8. Ikeshoji T, de Nahui FNB, Kimura S, Yoneya M (1991) Computer analysis on natural convection in thin-layer thermocells with a soluble redox couple: Part 2. E-I relation, electric power, heat flux and electrochemical heat pump. Journal of Electroanalytical Chemistry 312 (1-2):43-56. doi:Doi: 10.1016/0022-0728(91)85143-d

9. Ikeshoji T, Kimura S, de Nahui FNB, Yoneya M (1991) Computer analysis of natural convection in thin-layer thermocells with a soluble redox couple: Part 1. Method and the

unsteady problem. Journal of Electroanalytical Chemistry 307 (1-2):29-45. doi:Doi: 10.1016/0022-0728(91)85537-y

10. Ikeshoji T (1987) Thermoelectric Conversion by Thin-Layer Thermogalvanic Cells with Soluble Redox Couples. Bulletin of the Chemical Society of Japan 60 (4):1505-1514. doi:doi:10.1246/bcsj.60.1505

11. Chum HL, Osteryoung RA (1981) Review of thermally regenerative electrochemcial systems. vol 2. Solar Energy Research Institute,

12. Quickenden TI, Vernon CF (1986) Thermogalvanic conversion of heat to electricity. Solar Energy 36 (1):63-72. doi:Doi: 10.1016/0038-092x(86)90061-7

13. Quickenden TI, Mua Y (1995) A Review of Power Generation in Aqueous Thermogalvanic Cells. Journal of The Electrochemical Society 142 (11):3985-3994

14. Hu R, Cola BA, Haram N, Barisci JN, Lee S, Stoughton S, Wallace G, Too C, Thomas M, Gestos A, Cruz MEd, Ferraris JP, Zakhidov AA, Baughman RH (2010) Harvesting Waste Thermal Energy Using a Carbon-Nanotube-Based Thermo-Electrochemical Cell. Nano Letters 10 (3):838-846. doi:10.1021/nl903267n

15. Gong K, Yan Y, Zhang M, Su L, Xiong S, Mao L (2005) Electrochemistry and Electroanalytical Applications of Carbon Nanotubes: A Review. Analytical Sciences 21 (12):1383-1393

16. Landi BJ, Ganter MJ, Cress CD, DiLeo RA, Raffaelle RP (2009) Carbon nanotubes for lithium ion batteries. Energy & Environmental Science 2 (6):638-654

17. McCreery RL (2008) Advanced Carbon Electrode Materials for Molecular Electrochemistry. Chemical Reviews 108 (7):2646-2687. doi:10.1021/cr068076m

18. Merkoçi A, Pumera M, Llopis X, Pérez B, del Valle M, Alegret S (2005) New materials for electrochemical sensing VI: Carbon nanotubes. TrAC Trends in Analytical Chemistry 24 (9):826-838. doi:10.1016/j.trac.2005.03.019

19. Wang C, Waje M, Wang X, Tang JM, Haddon RC, Yan (2003) Proton Exchange Membrane Fuel Cells with Carbon Nanotube Based Electrodes. Nano Letters 4 (2):345-348. doi:10.1021/nl034952p

20. Panchakarla LS, Govindaraj A, Rao CNR (2007) Nitrogen- and Boron-Doped Double-Walled Carbon Nanotubes. ACS Nano 1 (5):494-500. doi:10.1021/nn700230n

21. Gong K, Du F, Xia Z, Durstock M, Dai L (2009) Nitrogen-Doped Carbon Nanotube Arrays with High Electrocatalytic Activity for Oxygen Reduction. Science 323 (5915):760-764. doi:10.1126/science.1168049

22. Kuzminskii YV, Zasukha VA, Kuzminskaya GY (1994) Thermoelectric effects in electrochemical systems. Nonconventional thermogalvanic cells. Journal of Power Sources 52 (2):231-242. doi:Doi: 10.1016/0378-7753(94)02015-9

23. Galiński M, Lewandowski A, Stępniak I (2006) Ionic liquids as electrolytes. Electrochimica Acta 51 (26):5567-5580. doi:http://dx.doi.org/10.1016/j.electacta.2006.03.016

24. Abraham TJ, MacFarlane DR, Baughman RH, Jin L, Li N, Pringle JM (2013) Towards ionic liquid-based thermoelectrochemical cells for the harvesting of thermal energy. Electrochimica Acta 113 (0):87-93. doi:http://dx.doi.org/10.1016/j.electacta.2013.08.087

25. Abraham TJ, MacFarlane DR, Baughman RH, Li N, Chen Y, Pringle JM (2013) Protic ionic liquid-based thermoelectrochemical cells for the harvesting of waste heat. MRS Online Proceedings Library 1575. doi:doi:10.1557/opl.2013.647

26. Abraham TJ, MacFarlane DR, Pringle JM (2013) High Seebeck coefficient redox ionic liquid electrolytes for thermal energy harvesting. Energy & Environmental Science 6 (9):2639-2645. doi:10.1039/c3ee41608a

27. Abraham TJ, Tachikawa N, MacFarlane DR, Pringle JM (2014) Investigation of the kinetic and mass transport limitations in thermoelectrochemical cells with different electrode materials. Physical Chemistry Chemical Physics 16 (6):2527-2532. doi:10.1039/c3cp54577f

28. Salazar PF, Kumar S, Cola BA (2012) Nitrogen- and Boron-Doped Carbon Nanotube Electrodes in a Thermo-Electrochemical Cell. Journal of The Electrochemical Society 159 (5):B483-B488. doi:10.1149/2.043205jes

29. Bonetti M, Nakamae S, Roger M, Guenoun P (2011) Huge Seebeck coefficients in nonaqueous electrolytes. The Journal of Chemical Physics 134 (11):114513

30. Rooney D, Jacquemin J, Gardas R (2010) Thermophysical Properties of Ionic Liquids. 290:185-212. doi:10.1007/128_2008_32

31. Fröba A, Rausch M, Krzeminski K, Assenbaum D, Wasserscheid P, Leipertz A (2010) Thermal Conductivity of Ionic Liquids: Measurement and Prediction. International Journal of Thermophysics 31 (11):2059-2077. doi:10.1007/s10765-010-0889-3

32. Benedetti JE, Corrêa AA, Carmello M, Almeida LCP, Gonçalves AS, Nogueira AF (2012) Cross-linked gel polymer electrolyte containing multi-wall carbon nanotubes for application in dye-sensitized solar cells. Journal of Power Sources 208 (0):263-270. doi:http://dx.doi.org/10.1016/j.jpowsour.2012.01.147

33. Chang Y-H, Lin P-Y, Huang S-R, Liu K-Y, Lin K-F (2012) Enhancing photovoltaic performance of all-solid-state dye-sensitized solar cells by incorporating ionic liquid-physisorbed MWCNT. Journal of Materials Chemistry 22 (31):15592-15598. doi:10.1039/c2jm31658g

34. Karim MR, Islam A, Singh SP, Han L (2011) Quasi Solid-State Dye-Sensitized Solar Cell Incorporating Highly Conducting Polythiophene-Coated Carbon Nanotube Composites in Ionic Liquid. Advances in OptoElectronics 2011:7. doi:10.1155/2011/357974

35. Lee C-P, Lin L-Y, Chen P-Y, Vittal R, Ho K-C (2010) All-solid-state dye-sensitized solar cells incorporating SWCNTs and crystal growth inhibitor. Journal of Materials Chemistry 20 (18):3619-3625. doi:10.1039/b925221e

36. Zhang Y, Shen Y, Han D, Wang Z, Song J, Li F, Niu L (2007) Carbon nanotubes and glucose oxidase bionanocomposite bridged by ionic liquid-like unit: Preparation and electrochemical properties. Biosensors and Bioelectronics 23 (3):438-443. doi:http://dx.doi.org/10.1016/j.bios.2007.06.010

37. Fukushima T, Asaka K, Kosaka A, Aida T (2005) Fully Plastic Actuator through Layer-by-Layer Casting with Ionic-Liquid-Based Bucky Gel. Angewandte Chemie 117 (16):2462-2465. doi:10.1002/ange.200462318

38. Fukushima T, Aida T (2007) Ionic Liquids for Soft Functional Materials with Carbon Nanotubes. Chemistry – A European Journal 13 (18):5048-5058. doi:10.1002/chem.200700554

39. Tunckol M, Durand J, Serp P (2012) Carbon nanomaterial–ionic liquid hybrids. Carbon 50 (12):4303-4334. doi:http://dx.doi.org/10.1016/j.carbon.2012.05.017

40. Yang Y-K, Xie X-L, Cui W (2012) Functionalization of Carbon Nanotubes with Ionic Liquids. In: Mohammad A, Inamuddin D (eds) Green Solvents II. Springer Netherlands, pp 399-434. doi:10.1007/978-94-007-2891-2_15

41. Vahlman H, Halme J, Korhonen J, Aitola K, Patakangas J (2013) On the Mass Transport in Apparently Iodine-Free Ionic Liquid Polyaniline-Coated Carbon Black Composite Electrolytes in Dye-Sensitized Solar Cells. The Journal of Physical Chemistry C 117 (23):11920-11929. doi:10.1021/jp401401t

42. Thess A, Lee R, Nikolaev P, Dai H (1996) Crystalline ropes of metallic carbon nanotubes. Science 273 (5274):483

43. Polo-Luque ML, Simonet BM, Valcárcel M (2013) Functionalization and dispersion of carbon nanotubes in ionic liquids. TrAC Trends in Analytical Chemistry 47 (0):99-110. doi:http://dx.doi.org/10.1016/j.trac.2013.03.007

44. Fukushima T, Kosaka A, Ishimura Y, Yamamoto T, Takigawa T, Ishii N, Aida T (2003) Molecular Ordering of Organic Molten Salts Triggered by Single-Walled Carbon Nanotubes. Science 300 (5628):2072-2074. doi:10.1126/science.1082289

45. Ducros JB, Buchtova N, Magrez A, Chauvet O, Le Bideau J (2011) Ionic and electronic conductivities in carbon nanotubes - ionogel solid device. Journal of Materials Chemistry 21 (8):2508-2511. doi:10.1039/c0jm02016h

46. Jameson CJ (1980) Effects on intermolecular interactions and intramolecular dynamics on nucler resonance. Bulletin of Magnetic Resonance 3 (1):3-29

47. Fredlake CP, Crosthwaite JM, Hert DG, Aki SNVK, Brennecke JF (2004) Thermophysical Properties of Imidazolium-Based Ionic Liquids. Journal of Chemical & Engineering Data 49 (4):954-964. doi:10.1021/je034261a

48. Martínez-Palou R (2010) Microwave-assisted synthesis using ionic liquids. Mol Divers 14 (1):3-25. doi:10.1007/s11030-009-9159-3

49. Ausman KD, Piner R, Lourie O, Ruoff RS, Korobov M (2000) Organic Solvent Dispersions of Single-Walled Carbon Nanotubes: Toward Solutions of Pristine

Nanotubes. The Journal of Physical Chemistry B 104 (38):8911-8915. doi:10.1021/jp002555m

50. Chen G, Sun G, Liu Z (2010) Dispersion of pristine multi-walled carbon nanotubes in common organic solvents. Nano 05 (02):103-109. doi:doi:10.1142/S1793292010001986

51. Bellayer S, Gilman JW, Eidelman N, Bourbigot S, Flambard X, Fox DM, De Long HC, Trulove PC (2005) Preparation of Homogeneously Dispersed Multiwalled Carbon Nanotube/Polystyrene Nanocomposites via Melt Extrusion Using Trialkyl Imidazolium Compatibilizer. Advanced Functional Materials 15 (6):910-916. doi:10.1002/adfm.200400441

52. Wang J, Chu H, Li Y (2008) Why Single-Walled Carbon Nanotubes Can Be Dispersed in Imidazolium-Based Ionic Liquids. ACS Nano 2 (12):2540-2546. doi:10.1021/nn800510g

53. Salazar P, Kumar S, Cola B (2014) Design and optimization of thermo-electrochemical cells. Journal of Applied Electrochemistry 44 (2):325-336. doi:10.1007/s10800-013-0638-y

54. Salazar PF, Chan KJ, Stephens ST, Cola BA (2014) Enhanced Electrical Conductivity of Imidazolium-Based Ionic Liquids Mixed with Carbon Nanotubes: A Spectroscopic Study. Journal of The Electrochemical Society 161 (9):H481-H486. doi:10.1149/2.0401409jes

55. Agar JN (1963) Thermogalvanic cells. In: Delay P, Tobias CW (eds) Advances in Electrochemistry and Electrochem. Eng., vol 3. Interscience, New York, pp 31-121

56. Tyrrell HJ (1961) Diffusion and Heat Flow in Liquids. Butterworths, London

57. Newman J (1995) Thermoelectric effects in electrochemical systems. Industrial & Engineering Chemistry Research 34 (10):3208-3216. doi:10.1021/ie00037a005

58. Bard AJ (2001) Electrochemical Methods: Fundamentals and Applications. 2 edn. John Wiley & Sons, Inc.,

59. Bockris JOM (1973) Modern electrochemistry: an introduction to an interdisciplinary area vol 2. Plenum Press, New York

60. Newman JS (1991) Electrochemical systems. 2 edn. Prentice-Hall, Englewood Cliffs, NJ

61. Saraç H, Patrick MA, Wragg AA (1993) Physical properties of the ternary electrolyte potassium ferri-ferrocyanide in aqueous sodium hydroxide solution in the range 10–90°C. Journal of Applied Electrochemistry 23 (1):51-55. doi:10.1007/bf00241575

62. Ching S, Dudek R, Tabet E (1994) Cyclic Voltammetry with Ultramicroelectrodes. Journal of Chemical Education 71 (7):602. doi:10.1021/ed071p602

63. Bard AJ, Faulkner LR (2000) Electrochemical Methods: Fundamentals and Applications. Wiley,

64. Inzelt G (2013) Pseudo-reference Electrodes. In: Inzelt G, Lewenstam A, Scholz F (eds) Handbook of Reference Electrodes. Springer Berlin Heidelberg, pp 331-332. doi:10.1007/978-3-642-36188-3_14

65. Izutsu K (2013) Reference Electrodes for Use in Nonaqueous Solutions. In: Inzelt G, Lewenstam A, Scholz F (eds) Handbook of Reference Electrodes. Springer Berlin Heidelberg, pp 145-187. doi:10.1007/978-3-642-36188-3_6

66. Kissinger PT, Heineman WR (1983) Cyclic voltammetry. Journal of Chemical Education 60 (9):702. doi:10.1021/ed060p702

67. Schmitz JEJ, Montree AH (1985) Determination of the reaction entropy of a quasi-reversible redox reaction with cyclic voltammetry. Analytical Chemistry 57 (1):371-372. doi:10.1021/ac00279a086

68. Spitzer P, Wunderli S, Maksymiuk K, Michalska A, Kisiel A, Galus Z, Tauber G (2013) Reference Electrodes for Aqueous Solutions. In: Inzelt G, Lewenstam A, Scholz F (eds) Handbook of Reference Electrodes. Springer Berlin Heidelberg, pp 77-143. doi:10.1007/978-3-642-36188-3_5

69. Tanimoto S, Ichimura A (2013) Discrimination of Inner- and Outer-Sphere Electrode Reactions by Cyclic Voltammetry Experiments. Journal of Chemical Education 90 (6):778-781. doi:10.1021/ed200604m

70. Van Benschoten JJ, Lewis JY, Heineman WR, Roston DA, Kissinger PT (1983) Cyclic voltammetry experiment. Journal of Chemical Education 60 (9):772. doi:10.1021/ed060p772

71. Lvovich VF (2012) Distributed Impedance Models. In: Impedance Spectroscopy - Applications to Electrochemical and Dielectric Phenomena. John Wiley & Sons, pp 97-111

72. Orazem ME, Tribollet B (2008) Experimental Design. In: Electrochemical Impedance Spectroscopy. John Wiley & Sons, Inc., pp 129-152. doi:10.1002/9780470381588.ch8

73. Haynes WM (2012) CRC Handbook of Chemistry and Physics, 93rd Edition. Taylor & Francis,

74. Macdonald JR, Johnson WB (2005) Fundamentals of Impedance Spectroscopy. In: Impedance Spectroscopy. John Wiley & Sons, Inc., pp 1-26. doi:10.1002/0471716243.ch1

75. Pour Shahid Saeed Abadi P, Hutchens SB, Greer JR, Cola BA, Graham S (2012) Effects of morphology on the micro-compression response of carbon nanotube forests. Nanoscale 4 (11):3373-3380. doi:10.1039/c2nr30474k

76. Jacobsen NE (2007) Interpretation of Proton (1H) NMR Spectra. In: NMR Spectroscopy Explained. John Wiley & Sons, Inc., pp 39-73. doi:10.1002/9780470173350.ch2

77. Price WS (1997) Pulsed-field gradient nuclear magnetic resonance as a tool for studying translational diffusion: Part 1. Basic theory. Concepts in Magnetic Resonance 9 (5):299-336. doi:10.1002/(sici)1099-0534(1997)9:5<299::aid-cmr2>3.0.co;2-u

78. Price WS (1998) Pulsed-field gradient nuclear magnetic resonance as a tool for studying translational diffusion: Part II. Experimental aspects. Concepts in Magnetic Resonance 10 (4):197-237. doi:10.1002/(sici)1099-0534(1998)10:4<197::aid-cmr1>3.0.co;2-s

79. Susan MABH, Noda A, Watanabe M (2005) Diffusion in Ionic Liquids and Correlation with Ionic Transport Behavior. In: Electrochemical Aspects of Ionic Liquids. John Wiley & Sons, Inc., pp 55-74. doi:10.1002/0471762512.ch5

80. Spiro M (1964) Standard exchange current densities of redox systems at platinum electrodes. Electrochimica Acta 9 (11):1531-1537. doi:http://dx.doi.org/10.1016/0013-4686(64)85032-5

81. Wendt H, Kreysa G (1999) Mass Transfer by Fluid Flow, Convective Diffusion and Ionic Electricity Transport in Electrolytes and Cells. In: Electrochemical Engineering Springer, pp 81-127

82. Breck WG, Lin J (1965) Thermal diffusion studies with redox electrodes. Part 2.-Ferro-ferricyanide couple. Transactions of the Faraday Society 61:1511-1515

83. Mua Y, Quickenden TI (1996) Power Conversion Efficiency, Electrode Separation, and Overpotential in the Ferricyanide/Ferrocyanide Thermogalvanic Cell. Journal of The Electrochemical Society 143 (8):2558-2564. doi:10.1149/1.1837047

84. Feng L, Yan Y, Chen Y, Wang L (2011) Nitrogen-doped carbon nanotubes as efficient and durable metal-free cathodic catalysts for oxygen reduction in microbial fuel cells. Energy & Environmental Science 4 (5):1892-1899. doi:10.1039/c1ee01153g

85. Randles JEB (1947) Kinetics of rapid electrode reactions. Discussions of the Faraday Society 1:11-19

86. Strmcnik D, Kodama K, van der Vliet D, Greeley J, Stamenkovic VR, Marković NM (2009) The role of non-covalent interactions in electrocatalytic fuel-cell reactions on platinum. Nat Chem 1 (6):466-472. doi:http://www.nature.com/nchem/journal/v1/n6/suppinfo/nchem.330_S1.html

87. Delahay P (1965) Double layer and electrode kinetics. John Wiley and Sons, Inc,

88. Bard AJ (2001) Electrochemical methods : fundamentals and applications 2edn. John Wiley and Sons, Inc,

89. Lee C-P, Chen P-Y, Vittal R, Ho K-C (2010) Iodine-free high efficient quasi solid-state dye-sensitized solar cell containing ionic liquid and polyaniline-loaded carbon black. Journal of Materials Chemistry 20 (12):2356-2361

90. Widegren JA, Magee JW (2007) Density, Viscosity, Speed of Sound, and Electrolytic Conductivity for the Ionic Liquid 1-Hexyl-3-methylimidazolium

Bis(trifluoromethylsulfonyl)imide and Its Mixtures with Water. Journal of Chemical & Engineering Data 52 (6):2331-2338. doi:10.1021/je700329a

91. Widegren JA, Saurer EM, Marsh KN, Magee JW (2005) Electrolytic conductivity of four imidazolium-based room-temperature ionic liquids and the effect of a water impurity. The Journal of Chemical Thermodynamics 37 (6):569-575. doi:http://dx.doi.org/10.1016/j.jct.2005.04.009

92. Zhang J, Mine M, Zhu D, Matsuo M (2009) Electrical and dielectric behaviors and their origins in the three-dimensional polyvinyl alcohol/MWCNT composites with low percolation threshold. Carbon 47 (5):1311-1320. doi:http://dx.doi.org/10.1016/j.carbon.2009.01.014

93. Jorcin J-B, Orazem ME, Pébère N, Tribollet B (2006) CPE analysis by local electrochemical impedance spectroscopy. Electrochimica Acta 51 (8–9):1473-1479. doi:http://dx.doi.org/10.1016/j.electacta.2005.02.128

94. Lvovich VF (2012) Impedance Spectroscopy - Applications to Electrochemical and Dielectric Phenomena. John Wiley & Sons

95. Jankovic J, Wilkinson DP, Hui R (2011) Electrochemical Impedance Spectroscopy of Ba2In2O5: Effect of Porosity, Grain Size, Dopant, Atmosphere and Temperature. Journal of The Electrochemical Society 159 (2):B109-B120. doi:10.1149/2.022202jes

96. Lvovich VF (2012) Impedance Analysis of Complex Systems. In: Impedance Spectroscopy - Applications to Electrochemical and Dielectric Phenomena. John Wiley & Sons, pp 113-144

97. Cheng Q, Debnath S, O'Neill L, Hedderman TG, Gregan E, Byrne HJ (2010) Systematic Study of the Dispersion of SWNTs in Organic Solvents. The Journal of Physical Chemistry C 114 (11):4857-4863. doi:10.1021/jp911202d

98. Bauhofer W, Kovacs JZ (2009) A review and analysis of electrical percolation in carbon nanotube polymer composites. Composites Science and Technology 69 (10):1486-1498. doi:http://dx.doi.org/10.1016/j.compscitech.2008.06.018

99. Tsangaris GM, Kouloumbi N, Kyvelidis S (1996) Interfacial relaxation phenomena in particulate composites of epoxy resin with copper or iron particles. Materials Chemistry and Physics 44 (3):245-250. doi:http://dx.doi.org/10.1016/0254-0584(96)80063-0

100. Xi Y, Bin Y, Chiang CK, Matsuo M (2007) Dielectric effects on positive temperature coefficient composites of polyethylene and short carbon fibers. Carbon 45 (6):1302-1309. doi:http://dx.doi.org/10.1016/j.carbon.2007.01.019

101. Smyth CP (1955) Dielectric behavior and structure: dielectric constant and loss, dipole moment and molecular structure. McGraw-Hill

102. Cesare Marincola F, Piras C, Russina O, Gontrani L, Saba G, Lai A (2012) NMR Investigation of Imidazolium-Based Ionic Liquids and Their Aqueous Mixtures. ChemPhysChem 13 (5):1339-1346. doi:10.1002/cphc.201100810

103. Jeon Y, Sung J, Seo C, Lim H, Cheong H, Kang M, Moon B, Ouchi Y, Kim D (2008) Structures of Ionic Liquids with Different Anions Studied by Infrared Vibration Spectroscopy. The Journal of Physical Chemistry B 112 (15):4735-4740. doi:10.1021/jp7120752

104. Zheng Y-Z, Wang N-N, Luo J-J, Zhou Y, Yu Z-W (2013) Hydrogen-bonding interactions between [BMIM][BF4] and acetonitrile. Physical Chemistry Chemical Physics 15 (41):18055-18064. doi:10.1039/c3cp53356e

105. Claridge TDW (2009) High-resolution NMR techniques in organic chemistry. 2nd ed. edn. Elsevier, Amsterdam

106. Chen H, Ding Y, He Y, Tan C (2007) Rheological behaviour of ethylene glycol based titania nanofluids. Chemical Physics Letters 444 (4–6):333-337. doi:http://dx.doi.org/10.1016/j.cplett.2007.07.046

107. Lee J-H, Hwang KS, Jang SP, Lee BH, Kim JH, Choi SUS, Choi CJ (2008) Effective viscosities and thermal conductivities of aqueous nanofluids containing low volume concentrations of Al2O3 nanoparticles. International Journal of Heat and Mass Transfer 51 (11–12):2651-2656. doi:http://dx.doi.org/10.1016/j.ijheatmasstransfer.2007.10.026

108. Webman I, Jortner J, Cohen MH (1977) Critical exponents for percolation conductivity in resistor networks. Physical Review B 16 (6):2593-2596

109. Gao L, Zhou XF (2006) Differential effective medium theory for thermal conductivity in nanofluids. Physics Letters A 348 (3–6):355-360. doi:http://dx.doi.org/10.1016/j.physleta.2005.08.069

110. Maxwell JC (1904) A treatise on electricity and magnetism, vol 1. 3 edn., Clarendon, Oxford

111. Tinga WR, Voss WAG, Blossey DF (1973) Generalized approach to multiphase dielectric mixture theory. Journal of Applied Physics 44 (9):3897-3902. doi:doi:http://dx.doi.org/10.1063/1.1662868

112. Qu L, Dai L (2005) Substrate-Enhanced Electroless Deposition of Metal Nanoparticles on Carbon Nanotubes. Journal of the American Chemical Society 127 (31):10806-10807. doi:10.1021/ja053479+